

ASSESSING STRUCTURAL AND MATERIAL PROPERTIES OF BONE FOLLOWING
RADIATION THERAPY AND HEMARTHROSIS

Lindsay Katherine Sullivan

A dissertation submitted to the faculty at the University of North Carolina at Chapel Hill in
partial fulfillment of the requirements for the degree of Doctor of Philosophy in the Department
of Biomedical Engineering in the School of Medicine.

Chapel Hill
2020

Approved by:

Ted A. Bateman

Jacqueline H. Cole

Jeffrey S. Willey

Brian O. Diekman

Anthony G. Lau

© 2020
Lindsay Katherine Sullivan
ALL RIGHTS RESERVED

To my Mom and Dad, I am forever grateful for your love and support.

ABSTRACT

Lindsay Katherine Sullivan: Assessing Structural and Material Properties of Bone Following Radiation Therapy and Hemarthrosis
(Under the direction of Ted Bateman)

Radiation therapy is a common clinical technique used to reduce tumor proliferation. A 2005 study by Baxter et al. showed that women who received pelvic radiation therapy were more likely to experience a pelvic fracture and 90% of these fractures were hip fractures [3]. There is also clinical evidence that premenopausal women with gynecological tumors may experience a premature and permanent menopause as a result of damage to the ovaries caused by radiation therapy [11]. The effects of this early onset estrogen deficiency on bone health may be more severe since these patients likely have not reached peak bone mass.

Both structural and material properties play an important role in the assessment of bone strength and fracture risk. Structural parameters, such as bone volume and trabecular thickness, are often studied more frequently due to the relative ease of access to imaging modalities and the ability to image in vivo. Changes in bone composition and material properties resulting from disease states or treatment methods are just as important in predicting bone function, but are more difficult to assess. In the first aim, a mouse model for structural changes resulting from fractionated radiation therapy and estrogen deficiency will be characterized at multiple skeletal sites. In the second aim, the efficacy of zoledronate to mitigate bone loss from radiation therapy will be evaluated by examining structural and material properties at three time points in a mouse

model. For the final aim, the techniques developed in aim two will be applied to evaluate joint changes following hemarthrosis in a mouse model.

ACKNOWLEDGEMENTS

I would like to thank Dr. Ted A. Bateman for all of his guidance and support throughout graduate school. His advice and endless encouragement have not only contributed to the outcome of this research, but also my confidence and growth as an engineer. I would like to thank Dr. Jacqueline H. Cole for her mentorship and generosity over the past few years. As my committee chair, she went above and beyond to help me find resources and provide advice for my project. I would like to thank Dr. Anthony Lau for being an incredible mentor since the first day I joined the lab as an undergraduate student. He is the reason I had the opportunities to present at conferences, travel to Cambridge for a fellowship and was able to gain confidence as a researcher. I would also like to thank Dr. Jeffrey S. Willey and Dr. Brian O. Diekmann for their support and advice during my degree.

I am extremely grateful to Eric Livingston, my lab sidekick, for helping me with anything and everything on a daily basis. Most of all, thank you for keeping lab morale high with Med Deli Mondays (and Thursdays) and hitting the high notes in every song. Thank you to the rest of the Bateman Lab members for all of your help. I am also grateful for Dr. Michelle L. Oyen and Dr. Virginia L. Ferguson for their incredible advice, support and the opportunity to spend time working in their labs. I learned so much in the time spent in both of their labs.

Finally, thank you to my family and friends for their endless love and support. Mom, Dad, Laura and Meredith, I could not have gotten to this point without you cannot thank you

enough. I would also like to thank Dr. Ned Hardison and my roommates, Dr. Terra Swanson and Ranger Ruffins for always being there for me and making me laugh.

TABLE OF CONTENTS

LIST OF FIGURES	xiv
LIST OF TABLES	xx
LIST OF ABBREVIATIONS	xxiii
CHAPTER 1: GENERAL BACKGROUND	1
Introduction	1
Bone Cells	1
Hierarchical Structure of Human Bone	2
Bone Remodeling	4
Bone Strength and Methods for Assessment of Relevant Bone Properties	6
Clinical Assessment of Bone Strength:	6
Bone Structure Assessment in Mouse Model:	7
Bone Material Properties Assessment in a Mouse Model:	9
Postmenopausal Osteoporosis	13
Bisphosphonates	14
Radiation Therapy and Bone	14
Hemophilia A and Bone	16
Research Objectives	18

CHAPTER 2: A MOUSE MODEL FOR SKELETAL STRUCTURE AND FUNCTION CHANGES CAUSED BY RADIATION THERAPY AND ESTROGEN DEFICIENCY	20
Introduction	20
Materials and Methods	23
X-ray Dose Validation.....	23
Proximal Tibia MicroCT for Dose Validation	24
OVX and Radiation Study	24
Animals and Study Design	24
Tissue Collection	25
Dual-energy X-ray absorptiometry (DEXA).....	25
Microcomputed Tomography (MicroCT)	26
Finite Element Analysis	26
Proximal Tibia	28
Proximal Femur	28
Statistics.....	29
Results	29
X-ray Dose Validation Study	29
Proximal Tibia MicroCT	29
OVX and Radiation Study.....	29
Body Mass	29
DEXA	30
Whole body aBMD.....	30
Right Hindlimb aBMD	31
MicroCT Proximal Tibia	31

Proximal Tibia Trabecular Morphometry (Figure 2.3a-2.3d)	33
Proximal Tibia Cortical Morphometry (Figure 2.3e-2.3h).....	34
Proximal Tibia Finite Element Analysis	37
Proximal Tibia Trabecular Bone Stiffness	37
Proximal Tibia Cortical Bone Stiffness.....	37
Proximal Tibia Whole Bone Stiffness (Trabecular and Cortical Combined)	37
MicroCT Midshaft Femur	38
Midshaft Femur Cortical Morphometry	38
Proximal Femur Finite Element Analysis	39
Proximal Femur Stiffness	39
MicroCT L1 Vertebra.....	40
L1 Vertebra Trabecular Morphometry	40
L1 Vertebra Finite Element Analysis.....	41
L1 Vertebra Stiffness.....	41
Discussion	41
 CHAPTER 3: EFFECTS OF RADIATION AND HIGH-DOSE ZOLEDRONATE TREATMENT ON THE STRUCTURAL AND MATERIAL PROPERTIES OF BONE IN A MOUSE MODEL	 48
Introduction	48
Methods.....	51
Animals and Study Design	51
Microcomputed Tomography	51
Finite Element Analysis	52
Statistical Analysis	52
Nanoindentation	53

Fourier Transform Infrared Spectroscopy Imaging.....	55
Raman Spectroscopy	56
Results	58
Body Mass (Table 3.1)	58
Proximal Tibia MicroCT	59
3 Day Time Point.....	59
14 Day Time Point.....	60
6 Month Time Point.....	60
Proximal Tibia Finite Element Analysis	63
Nanoindentation	64
Two-way ANOVA	64
Mixed Effects Model.....	64
6 Month Analysis	64
14 Day Analysis	66
Fourier Transform Infrared Spectroscopy	67
Raman Spectroscopy	68
Two-Way ANOVA	68
Mixed Model Statistical Analysis	69
6 month analysis	69
14 day analysis	73
Discussion	76
 CHAPTER 4: CHARACTERIZATION OF STRUCTURAL AND MATERIAL CHANGES IN BONE FOLLOWING KNEE JOINT BLEEDING IN MALE AND FEMALE FACTOR VIII DEFICIENT MICE	 82
Introduction	82

Methods	84
Animals and Study Design	84
Microcomputed Tomography	85
Finite Element Analysis	86
Sample Preparation and Keyence Profilometry	86
Nanoindentation	87
Raman Spectroscopy	88
Results	89
MicroCT	89
Finite Element Analysis	97
Keyence Profilometry.....	98
Nanoindentation	99
Raman Spectroscopy	99
Discussion	101
CHAPTER 5: CONCLUSION AND FUTURE WORK	104
Summary of Findings	104
Limitations	108
Future Work	109
Clinical dose bisphosphonate treatment	109
Include OVX model into material characterization for drug efficacy	109
Validation of heterotopic ossification in hemarthrosis model.....	109
Improve finite element model to include modulus estimates as well.....	110
APPENDIX.....	111

Chapter 2	111
Chapter 3	118
Chapter 4	124
REFERENCES	131

LIST OF FIGURES

Figure 1.1: Hierarchical structure of bone. Reproduced from Liu et al. 2016 [1]	3
Figure 1.2: Bone remodeling cycle. Reproduced from Siddiqui and Partridge 2016 [9]	5
Figure 1.3: Bone strength determinants and methods to assess properties that influence bone strength. Reproduced from Fonseca et al. 2014 [4]	7
Figure 1.4: Example FTIR spectrum of bone. Reproduced from Kobrina et al. 2010 [2]	9
Figure 1.5: Example Raman spectrum of bone. Reproduced from Morris and Mandair 2011 [10]	10
Figure 1.6: Example load vs. displacement plot with parameters used for Oliver-Pharr method calculation of Young's Modulus. Reproduced from Oliver and Pharr 1992 [7]	11
Figure 1.7: Factors that contribute to bone strength and fracture risk. Reproduced from Torres-del-Pliego et al. 2013 [8]	13
Figure 1.8: Overview of coagulation pathways. Reproduced from Goswami et al. 2014 [5]	17
Figure 1.9: Comparison of hemophilic arthropathy to a normal joint. Reproduced from Pulles et al. 2017 [6]	18
Figure 2.1: Example finite element analysis meshes for whole proximal tibia segment (a), loaded whole tibia (b), cortical proximal tibia segment (c), loaded cortical tibia (d), proximal femur mesh with nodes selected in red to be displaced (e), loaded femoral neck (f), L1 Vertebra (g) and loaded L1 Vertebra (h)	27
Figure 2.2: Example MicroCT scans of proximal tibia segment showing trabecular bone in pink and cortical bone in gray for Sham-NR mouse (a), Sham-IRR mouse (b), OVX-NR mouse (c) and OVX-IRR mouse (d)	33
Figure 2.3: Graphs for MicroCT morphometry data for the proximal tibia segment including trabecular BV/TV (a), trabecular connectivity density (b), trabecular thickness (c), trabecular number (d), cortical porosity (e), cortical vBMD (f), cortical tissue mineral density (g)	

and cortical thickness (h). Error bars indicate standard error of the mean. *=significant effect of irradiation within Sham or OVX groups; #=significant effect of OVX within NR or IRR groups (p<0.05).....	36
Figure 2.4: Graphs for proximal tibia finite element analysis data including proximal tibia cortical stiffness (a), proximal tibia trabecular stiffness (b) and whole proximal tibia segment stiffness (c). Error bars indicate standard error of the mean. *= significant effect of irradiation within Sham or OVX groups; #=significant effect of OVX within NR or IRR groups (p<0.05).....	38
Figure 2.5: Graphs for MicroCT cortical morphometry data for the midshaft femur segment including cortical area (a), marrow area (b), BA/TA (c), cortical porosity (d) and cortical thickness (e). Error bars indicate standard error of the mean. *=significant effect of irradiation within Sham or OVX groups; #=significant effect of OVX within NR or IRR groups (p<0.05).....	39
Figure 2.6: Graph for femoral neck stiffness determined using finite element compression simulation. Error bars indicate standard error of the mean. #=significant effect of OVX within NR or IRR groups (p<0.05).....	39
Figure 2.7: Graphs for MicroCT trabecular morphometry data for the L1 vertebra including BV/TV (a), vBMD (b), trabecular thickness (c) and stiffness determined through finite element compression simulation (d). Error bars indicate standard error of the mean. *= significant effect of irradiation within Sham or OVX groups; #=significant effect of OVX within NR or IRR groups (p<0.05).....	40
Figure 3.1: Optical microscope proximal tibia image with region for nanoindentation array in a red rectangle. Six rows of four indents per row were performed starting close to the endosteal surface and ending close to the periosteal surface	53
Figure 3.2: Example image of proximal tibia set up for FTIR imaging. The blue rectangle represents the area for FTIR assessment.	55
Figure 3.3: (a) Proximal tibia cross section with area for Raman array in a red rectangle. Three indents per row were spaced 15 microns apart from periosteal to endosteal surface. (b) Example setup of array to gather spectral data across the cortical thickness.....	57
Figure 3.4: MicroCT example images of NR-ZOL bone at 6 month time point. The trabecular compartment (show in pink) is almost entirely filled in with bone.	61

Figure 3.5: Proximal tibia trabecular bone volume fraction at 3 day, 14 day and 6 month time points. *=significant effect of irradiation with PLAC or ZOL groups, #=significant effect of ZOL within NR or IRR groups ($p<0.05$).....	61
Figure 3.6: FEA proximal tibia stiffness comparison for treatment groups at 3 day, 14 day and 6 month time points. *=significant effect of irradiation with PLAC or ZOL groups, #=significant effect of ZOL within NR or IRR groups ($p<0.05$).....	64
Figure 3.7: Mean and standard deviation bar graphs of nanoindentation data for 14 days and 6 month time points by using average modulus for each bone as single data point ($n=3$).	64
Figure 3.8: Reduced modulus least square means for 6 month time point along cortical thickness from endosteal to periosteal surface from the mixed model analysis. Left graph compares irradiated mice (red) to non-irradiated mice (blue) and right graph compared zoledronate treated mice (blue) with placebo treated mice (red).....	65
Figure 3.9: Reduced modulus least square means for 14 day time point along cortical thickness from endosteal to periosteal surface using the mixed model analysis. Left graph compares irradiated mice (red) to non-irradiated mice (blue) and right graph compared zoledronate treated mice (blue) with placebo treated mice (red).....	66
Figure 3.10: FTIR graphs for relevant bone material ratios at the cortical tibia. (a) 14 day mineral to matrix ratio (b) 6 month mineral to matrix ratio (c) 14 day carbonate to phosphate ratio (d) 6 month carbonate to phosphate ratio (e) 14 day crystallinity (f) 6 month crystallinity	67
Figure 3.11: Raman spectroscopy graphs for relevant bone material ratios at the cortical tibia using a single average value per bone sample within a treatment group. (a) 14 day mineral to matrix ratio (b) 6 month mineral to matrix ratio (c) 14 day carbonate to phosphate ratio (d) 6 month carbonate to phosphate ratio (e) 14 day crystallinity (f) 6 month crystallinity	68
Figure 3.12: Heat maps for Raman Mineral to Matrix Ratio from each bone (white/yellow=high mineral to matrix ratio, red/black=low mineral to matrix ratio). (a) 14 day time point heat maps (b) 6 month time point heat maps.....	69
Figure 3.13: Mineral to matrix ratio least square means for 6 month time point along cortical thickness of the proximal tibia from endosteal to periosteal surface using the mixed model analysis. Left graph compares irradiated mice (red) to non-irradiated mice	

(blue) and right graph compared zoledronate treated mice (blue) with placebo treated mice (red).....	70
Figure 3.14: Carbonate to phosphate ratio least square means for 6 month time point along cortical thickness of the proximal tibia from endosteal to periosteal surface using the mixed model analysis. Left graph compares irradiated mice (red) to non-irradiated mice (blue) and right graph compared zoledronate treated mice (blue) with placebo treated mice (red).....	71
Figure 3.15: Crystallinity least square means for 6 month time point along cortical thickness of the proximal tibia from endosteal to periosteal surface using the mixed model analysis. Left graph compares irradiated mice (red) to non-irradiated mice (blue) and right graph compared zoledronate treated mice (blue) with placebo treated mice (red).	72
Figure 3.16: Mineral to matrix ratio least square means for 14 day time point along cortical thickness of the proximal tibia from endosteal to periosteal surface using the mixed model analysis. Left graph compares irradiated mice (red) to non-irradiated mice (blue) and right graph compared zoledronate treated mice (blue) with placebo treated mice (red).	73
Figure 3.17: Carbonate to phosphate ratio least square means for 14 day time point along cortical thickness of the proximal tibia from endosteal to periosteal surface using the mixed model analysis. Left graph compares irradiated mice (red) to non-irradiated mice (blue) and right graph compared zoledronate treated mice (blue) with placebo treated mice (red).....	74
Figure 3.18: Crystallinity least square means for 14 day time point along cortical thickness of the proximal tibia from endosteal to periosteal surface using the mixed model analysis. Left graph compares irradiated mice (red) to non-irradiated mice (blue) and right graph compared zoledronate treated mice (blue) with placebo treated mice (red).	75
Figure 4.1: Study design schematic including timeline for assessment and methods for bone characterization	84
Figure 4.2: Fluorescent image of cross-section of 28 day distal femurs for (a) non-injured limb and (b) injured limb with red rectangles marking the area for nanoindentation. Fluorescent green (calcein label) represents bone formation following injury.....	88
Figure 4.3: Selected microCT data comparing injured limb to contralateral limb in male mice. (a) Proximal tibia BV/TV	

(b) Distal femur BV/TV (c) Midshaft femur cortical area (d) Midshaft femur cortical porosity (e) Proximal tibia smoothness ratio (f) Distal femur smoothness ratio	92
Figure 4.4: Selected microCT data comparing injured limb to contralateral limb in female mice. (a) Proximal tibia BV/TV (b) Distal femur BV/TV (c) Midshaft femur cortical area (d) Midshaft femur cortical porosity (e) Proximal tibia smoothness ratio (f) Distal femur smoothness ratio.....	93
Figure 4.5: MicroCT images of injured knee joint at (a) 7 days (b) 14 days and (c) 28 days following injury.....	97
Figure 4.6: Fluorescent imaging of calcein label of injured distal femur at 28 days following injury. (a) Female injured limb (b) Male injured limb	97
Figure 4.7: Male distal femur finite element analysis for (a) cortical bone only (b) trabecular bone only and (c) trabecular and cortical bone combined stiffness.....	98
Figure 4.8: Example Keyence profilometry assessment (a) selected region for quantified surface roughness and (b) heat map image of bone section for surface roughness with maximum difference under 5 microns.....	98
Figure 4.9: Box and whisker plot comparison of reduced modulus for uninjured and injured male distal femurs at 28 days	99
Figure 4.10: Box and whisker plot comparison of mineral to matrix ratio for uninjured and injured male distal femurs at 28 days.....	100
Figure 4.11: Box and whisker plots for comparison of (a) carbonate to phosphate ratio and (b) crystallinity for uninjured and injured male distal femurs at 28 days.....	100
Figure 5.1: Right hindlimb DEXA data for OVX+Radiation study with four treatment group mean aBMD values plotted over time	111
Figure 5.2: Whole body DEXA data for OVX+Radiation study with four treatment group mean aBMD values plotted over time	111
Figure 5.3: Radiation+Zoledronate study example Mineral to Matrix Ratio mapping for FTIR data. Embedding material appears dark blue to light blue and bone spans roughly green to green from left to right. Endosteal surface=left green, periosteal surface=right green	121

Figure 5.4: Example MATLAB calculation of full-width half maximum (green circle) for phosphate peak in Raman spectroscopy data.....	122
Figure 5.5: Example Raman MATLAB spectra of bone after baseline subtraction and PMMA subtraction (x-axis represents wave shift and y-axis represents intensity).....	122
Figure 5.6: Nanoindentation data collected for 14 day time point for Radiation+Zoledronate study.....	123
Figure 5.7: Nanoindentation data collected for 6 month time point for Radiation+Zoledronate study.....	123
Figure 5.8: Example setup for hemophilia study Raman spectroscopy array on uninjured limb distal femur cortical bone.....	130

LIST OF TABLES

Table 2.1: Body mass summary and DEXA aBMD results from right hindlimb and whole body. All data presented as mean \pm standard deviation. *= significant effect of irradiation within Sham or OVX groups; #=significant effect of OVX within NR or IRR groups ($p<0.05$).....	30
Table 2.2: MicroCT bone morphometry data for proximal tibia, midshaft femur and L1 vertebra. All data presented as mean \pm standard deviation. *= significant effect of irradiation within Sham or OVX groups; #=significant effect of OVX within NR or IRR groups ($p<0.05$).....	32
Table 3.1: Initial body mass, final body mass and average change in body mass for each treatment group and time point. *=statistically significant effect of irradiation ($p<0.05$)	59
Table 3.2: Mean and standard deviation for 3 day, 14 day and 6 month proximal tibia trabecular analysis. *=significant effect of irradiation with PLAC or ZOL groups, #=significant effect of ZOL within NR or IRR groups ($p<0.05$)	62
Table 3.3: 6 month nanoindentation fixed effect results from full-factorial mixed model analysis and significance ($p<0.05$) shown by p-value in Prob>F column on the far right.	65
Table 3.4: 14 day nanoindentation fixed effect results from full-factorial mixed model analysis and significance ($p<0.05$) shown by p-value in Prob>F column on the far right.....	66
Table 3.5: 6 month mineral to matrix ratio fixed effect results from full-factorial mixed model analysis and significance ($p<0.05$) shown by p-value in Prob>F column on the far right.	70
Table 3.6: 6 month carbonate to phosphate ratio fixed effect test results from full-factorial mixed model analysis and significance ($p<0.05$) shown by p-value in Prob>F column on the far right	71
Table 3.7: 6 month crystallinity fixed effect test results from full-factorial mixed model analysis and significance ($p<0.05$) shown by p-value in Prob>F column on the far right	72
Table 3.8: 14 day mineral to matrix ratio fixed effect test results from full-factorial mixed model analysis and significance ($p<0.05$) shown by p-value in Prob>F column on the far right	73

Table 3.9: 14 day carbonate to phosphate ratio fixed effect test results from full-factorial mixed model analysis and significance (p<0.05) shown by p-value in Prob>F column on the far right	74
Table 3.10: 14 day crystallinity fixed effect test results from full-factorial mixed model analysis and significance (p<0.05) shown by p-value in Prob>F column on the far right	75
Table 4.1: Mean mouse body mass at dissection for each time point.....	89
Table 4.2: Mean and standard deviation for 7 day microCT data (*=significant p<0.05)	94
Table 4.3: Mean and standard deviation for 14 day microCT data (*=significant p<0.05)	95
Table 4.4: Mean and standard deviation for 28 day microCT data (*=significant p<0.05)	96
Table 5.1: OVX+Radiation study proximal tibia trabecular microCT raw data.....	112
Table 5.2: OVX+Radiation study proximal tibia cortical microCT raw data. Mean and standard deviation highlighted in gray (mean on top)	113
Table 5.3: OVX+Radiation study midshaft femur cortical microCT raw data. Mean and standard deviation highlighted in gray (mean on top)	114
Table 5.4: OVX+Radiation study proximal tibia finite element analysis raw data. Mean and standard deviation highlighted in gray (mean on top).....	115
Table 5.5: OVX+Radiation study femoral neck finite element analysis raw data. Mean and standard deviation (mean on top)	116
Table 5.6: OVX+Radiation study L1 Vertebra trabecular microCT analysis and finite element analysis raw data. Mean and standard deviation highlighted in gray (mean on top)	117
Table 5.7: Radiation+Zoledronate study 3 day proximal tibia trabecular microCT raw data	118
Table 5.8: Radiation+Zoledronate study 14 day proximal tibia trabecular microCT raw data	119

Table 5.9: Radiation+Zoledronate study 6 month proximal tibia trabecular microCT raw data	120
Table 5.10: Hemophilia study 7 day female distal femur trabecular microCT raw data	124
Table 5.11: Hemophilia study 7 day male distal femur trabecular microCT raw data	124
Table 5.12: Hemophilia study 7 day male and female distal femur microCT smoothness ratio raw data	125
Table 5.13: Hemophilia study 14 day male distal femur trabecular microCT raw data	126
Table 5.14: Hemophilia study 14 day female distal femur trabecular microCT raw data	126
Table 5.15: Hemophilia study 14 day distal femur male and female microCT smoothness ratio raw data	127
Table 5.16: Hemophilia study 28 day male distal femur trabecular microCT raw data	128
Table 5.17: Hemophilia study 28 day female distal femur trabecular microCT raw data	128
Table 5.18: Hemophilia study 28 day male and female distal femur microCT smoothness ratio raw data	129

LIST OF ABBREVIATIONS

μ CT	Microcomputed tomography
aBMD	Areal bone mineral density
AFF	Atypical femoral fracture
Al	Aluminum
ANOVA	Analysis of Variance
BA/TA	Bone area per total area
BED	Biologically effective dose
BIS	Bisphosphonate
BMD	Bone mineral density
BMU	Basic Multicellular Unit
BV/TV	Bone volume per total volume
Conn. D	Connectivity density
CSF	Colony-stimulating factor
CT	Computed Tomography
Ct. Ar	Cortical Area
Ct. Po	Cortical Porosity
Ct. Th	Cortical Thickness
Ct. TMD	Cortical tissue mineral density
DEXA	Dual energy x-ray absorptiometry
DNA	Deoxyribonucleic acid
FDA	Food and drug administration
FEA	Finite element analysis

FTIR	Fourier transform infrared spectroscopy
FVIII ^{-/-}	Factor 8 deficient
GPa	Gigapascal
Gy	Gray (absorption of one joule of radiation energy per kilogram of matter)
HA	Hydroxyapatite
HIV	Human immunodeficiency virus
HO	Heterotopic ossification
HSCs	Hematopoietic stem cells
IRR	Irradiated
keV	Kiloelectron-volt
kVp	Kilovoltage peak
L1	First lumbar vertebra
M. Ar	Marrow area
microCT	Microcomputed tomography
MRI	Magnetic resonance imaging
NR	Non-irradiated
OPG	Osteoprotegerin
OVX	Ovariectomized
PBS	Phosphate-buffered saline
PLAC	Placebo
PMMA	Polymethyl methacrylate
pQCT	Peripheral quantitative computed tomography
QCT	Quantitative computed tomography

RANK	Receptor activator of nuclear factor-kappaB
RANKL	Receptor activator of nuclear factor-kappaB ligand
RNA	Ribonucleic acid
RT	Radiation therapy
Sham	Sham-operated
SMI	Structure model index
St. dev.	Standard deviation
T. Ar	Total area
Tb. N	Trabecular number
Tb. Sp	Trabecular spacing
Tb. Th	Trabecular thickness
TMD	Tissue mineral density
vBMD	Volumetric bone mineral density
ZOL	Zoledronate

CHAPTER 1: GENERAL BACKGROUND

Introduction

Bone is a dynamic tissue composed of 20-40% organic matrix, 50-70% mineral, 5-10% water and less than 3% lipids [12]. Hydroxyapatite ($\text{Ca}_{10}(\text{PO}_4)_6(\text{OH})_2$) is the main component of the mineral portion of bone, although carbonate, acid phosphate and magnesium can also appear in small amounts. Hydroxyapatite crystals are approximately 20-100 nm, but change in size, number of impurities and shape over time as they mature [12]. The organic matrix is primarily made up of Type 1 collagen (~90%). Other noncollagenous proteins exist in much smaller quantities within the organic matrix, including osteonectin, osteocalcin, osteopontin, fibronectin, bone morphogenetic proteins, proteoglycans and growth factors [13]. Together, the matrix of bone allows for energy absorption and the mineral component of bone provides support for high loads and resists deformation [12].

Bone Cells

Osteoblasts, osteoclasts and osteocytes are the three major cell types that make up bone and influence bone remodeling [14]. Osteoblasts are bone-forming cells roughly 20-30 microns in size that are derived from mesenchymal stem cell. Among other tasks, the osteoblast is responsible to producing and secreting Type 1 collagen that makes up the osteoid (unmineralized surface) [15]. These cells can be found lining bone surfaces and their differentiation is mediated by bone morphogenic proteins and other growth factor- β proteins [14].

Osteocytes are osteoblasts that have become embedded in the bone matrix and account for ninety percent of all bone cells [12, 14]. These cells form an extensive canalicular network

which connects them to both cells on the bone surface as well as other osteocytes. The area in the bone in which osteocytes are found are called lacunae. Through the lacunar-canalicular network, osteocytes can sense mechanical forces or microdamage within the bone and then signal for remodeling in order to repair the damage. Osteocytes are capable of responding to metabolic signaling as well, including changes in estrogen [15].

Osteoclasts are large, multinucleated cells approximately 150-200 microns in diameter that reside in shallow cavities of the bone surface, often referred to as Howship's lacunae [14]. Osteoclasts are derived from mononuclear precursor cells of the monocyte-macrophage lineage. The main role of the osteoclast is to resorb bone [12]. In order to resorb bone, osteoclasts secrete hydrogen ions and cathepsin K enzyme. The acidity of the hydrogen ions dissolves the mineral portion of the bone matrix and then cathepsin K can digest the bone matrix [12]. Osteoclast function is mediated by numerous cytokines and factors including receptor activator of nuclear factor kappa-B ligand (RANKL), osteoprotegerin (OPG), macrophage colony-stimulating factor (macrophage CSF), interleukin-1, interleukin-6 and calcitonin [14].

Hierarchical Structure of Human Bone

The organization of bone varies at different length scales, from sub-nanostructure up to macrostructure (Figure 1.1) [16]. At the nanostructure level, apatite crystals exist within discrete spaces of collagen fibrils. The collagen molecules self-assemble into a triple helix structure. Within the apatite crystals are certain impurities including carbonate, hydrogen phosphate, sodium, magnesium and others. Average crystal thickness is about 2-3 nm and the

average crystal lengths and widths are 50 by 25 nm [16]. A mineralized collagen fibril is approximately 100 nm in diameter [1].

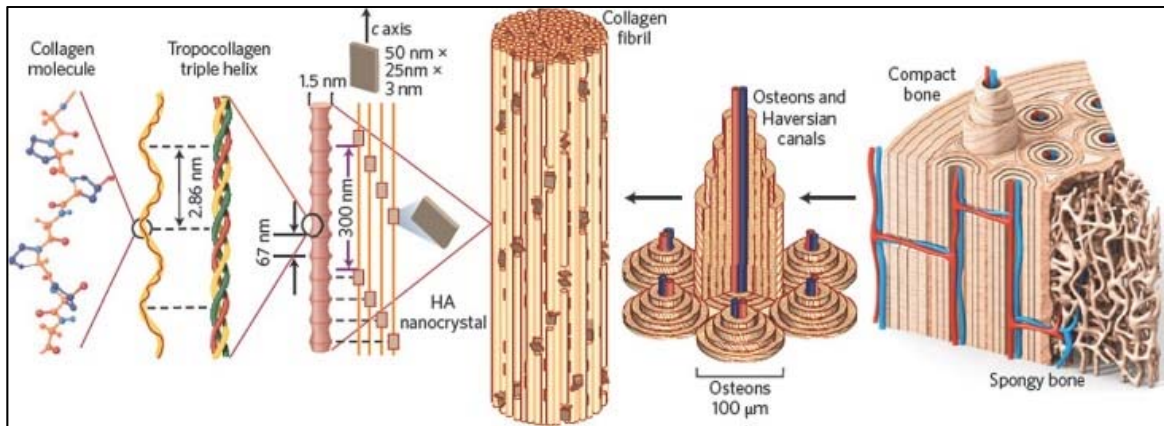


Figure 1.1: Hierarchical structure of bone. Reproduced from Liu et al. 2016 [1]

At the microstructure scale, bone lamellae are composed of tightly packed fibrils into bundles roughly 1 to 3 microns in diameter. Every other set of parallel bundles has a similar orientation and adjacent co-aligned bundles have between 40 and 80 degree angled offsets [17]. The fibrils and bundles create an anisotropic, cylindrical array. There is also a thin layer of disordered material between bundles where osteocyte canaliculi are found. An osteon is a concentric lamellar structure around a blood vessel [17]. Primary osteons can be differentiated from a secondary osteon by the absence of a cement line. A cement line is created where resorption stopped and new lamellae started being laid down. Secondary osteons, therefore, are products of bone remodeling and are about 100-200 microns in diameter with a 20-40 micron diameter central canal [17]. Secondary osteons are often referred to as Haversian systems and form parallel to the long axis of the bone.

In addition to the highly organized concentric structure of lamellar bone, there can also be woven bone. Woven bone is typically made during formation of primary bone and also during times of high turnover. The bone appears disorganized and is weaker than lamellar bone [12].

At the macrostructure, there is cortical and trabecular (or cancellous) bone. Cortical bone is dense, compact bone and can be seen as the outer surface of bone. Trabecular bone is highly porous bone (30-90% pores) found primarily at the ends of long bones, with bone marrow found in between struts. Within the human body, 80% of bone is cortical bone and 20% is trabecular bone). There are five main types of bones in the human body: long bones, short bones, flat bones, sesamoid bones and irregular bones. Long bones, such as the tibia and femur, support weight and provide structure [12]. Long bones can be divided into three main regions: diaphysis, metaphysis and epiphysis. The diaphysis contains mostly dense cortical bone and a hollow center. Both metaphysis and epiphysis contain trabecular bone surrounded by cortical bone, with the metaphysis being the wide portion of the bone below the growth plates. The epiphysis is the rounded portion at the end of the long bone [12]. The periosteum is a connective tissue that surrounds the outer cortical surface of bones except at the joints. The endosteum lines the interior cortical bone surface [12].

Bone Remodeling

Bone remodeling occurs in response to physiologic cues or mechanical forces in order to retain strength and mineral homeostasis [15]. The general process includes resorption of old bone and addition of new bone matrix, followed by mineralization. There are five main stages in the bone remodeling cycle: activation, resorption, reversal, formation and termination (Figure 1.2). One region of bone undergoing remodeling and including the cells involved is referred to as a basic multicellular unit (BMU).

The activation step occurs when a hormonal or mechanical signal is received by bone cells. This triggers the bone lining cells to separate from the surface of the bone to expose the area for remodeling. Then, osteoclast precursor cells circulating in the body are recruited and activated. Osteoclast activation leads to osteoclast differentiation and then attachment to the bone surface [18].

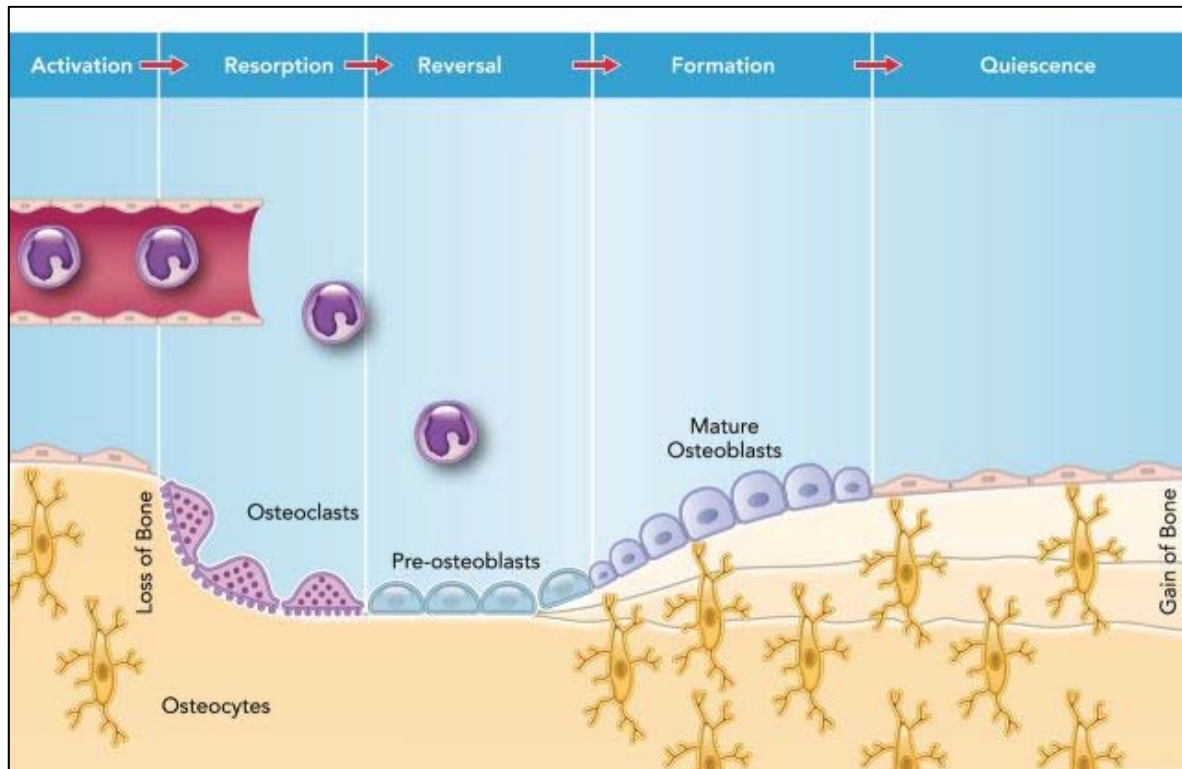


Figure 1.2: Bone remodeling cycle. Reproduced from Siddiqui and Partridge 2016 [9]

The next phase, resorption, takes place over the course of 2-4 weeks [15]. The osteoclast secretes hydrogen ions in order to lower the pH locally and dissolve the mineral. In order to digest the bone matrix, cathepsin K, metalloproteinase and other enzymes are secreted. The end result of resorption is the formation of Howship's lacunae (depressions on the bone surface) and osteoclast apoptosis [15]. The reversal phase happens when osteoclasts are replaced by osteoblast-lineage cells, though the exact signaling mechanism is still not fully understood [15]. This phase takes place over four to five weeks [18].

During the formation phase, osteoblasts produce and secrete the osteoid matrix composed primarily of type 1 collagen. Then, osteoblasts aid in mineralization and eventually either undergo apoptosis (50-70% of osteoblasts) or become osteocytes or bone-lining cells. The process of bone formation takes roughly 4 to 6 months [18]. The termination phase refers to the process of mineralization. Mineralization occurs up to 90 days following osteoid production in trabecular bone and 130 days after in cortical bone [15].

Bone Strength and Methods for Assessment of Relevant Bone Properties

Bone strength can be defined as the resistance to fracture. Bone structure, mass, geometry, composition and material properties all contribute to overall bone strength [15].

Clinical Assessment of Bone Strength:

Clinically, bone density is the most common method for evaluating bone strength [4]. The most common imaging modality to assess bone health is Dual-Energy X-ray Absorptiometry (DEXA) [4]. DEXA is relatively inexpensive and requires less radiation exposure compared to some other imaging options, such as computed tomography (CT) [19]. DEXA measures areal bone mineral density (BMD) and is quantified by the amount of hydroxyapatite scanned per unit area [20]. Compared to microCT, DEXA does not distinguish between trabecular and cortical bone and does not provide information on bone geometry [21]. Quantitative Computed Tomography (QCT) and high-resolution quantitative computed tomography provide three dimensional measurements of bone geometry, macrostructure and bone mineral distribution [22]. Magnetic resonance imaging (MRI) can also be used to evaluate bone structure and microarchitecture. This modality offers the advantages of being noninvasive and not requiring radiation exposure, but it is expensive and has a lower spatial resolution compared to CT [23]. Other than converting grayscale measures of bone into an estimation for mineral density,

material properties are not commonly measured in humans. However, occasionally a bone biopsy will be taken in order to assess tissue mineralization and composition [22].

Bone Structure Assessment in Mouse Model:

In research studies, mice are often used as a model to study osteoporosis and other bone pathologies (Figure 1.3) [24]. Micro-computed tomography (microCT) is a standard method for assessing bone structure in a mouse model. MicroCT scans can have a voxel size down to approximately two microns, allowing for detailed quantification of cortical and trabecular bone.

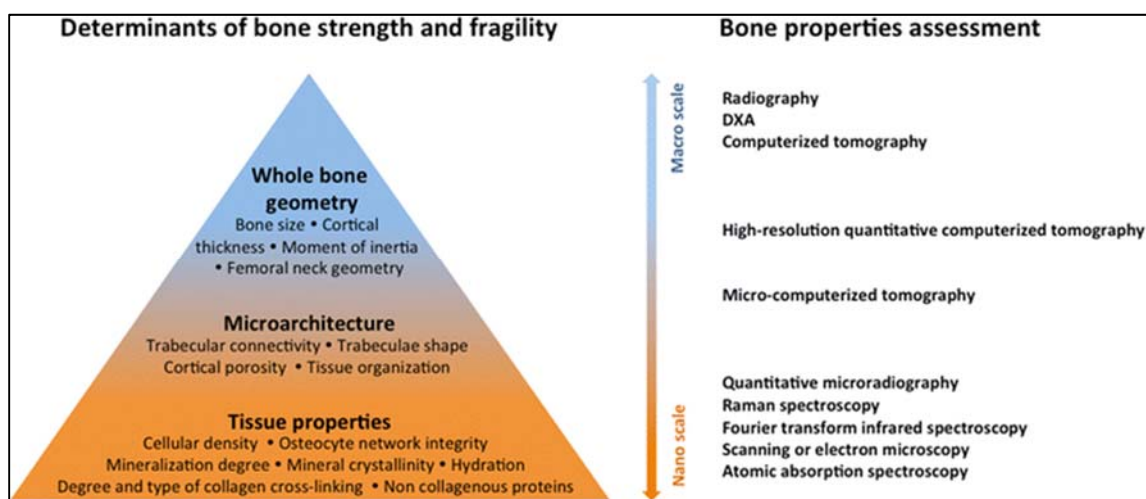


Figure 1.3: Bone strength determinants and methods to assess properties that influence bone strength. Reproduced from Fonseca et al. 2014 [4]

Several key parameters used to quantify trabecular structure include bone volume fraction (BV/TV), volumetric bone mineral density (vBMD), trabecular number, trabecular thickness (Tb.Th), trabecular separation (Tb.Sp) and connectivity density. Bone volume fraction is the ratio of the segmented bone volume to the total volume of the region of interest. Volumetric bone is a measure calculated by converting the linear attenuation coefficient from the target region into an average density of hydroxyapatite (grayscale) per unit volume. Trabecular number is a measure of the average number of trabeculae per length unit, trabecular spacing is the mean thickness of trabeculae using three dimensional assessment and trabecular separation is the mean

distance between trabeculae in three dimensions [25]. Connectivity density (Conn.D) is found by taking the number of marrow cavities fully surrounded by bone and the number of connections that would need to be broken to split the structure into two parts and dividing by the volume [25].

Common parameters used to assess cortical bone morphometry from microCT scans include cortical porosity (Ct.Po), cortical thickness (Ct.Th), total area (T.Ar), marrow area (M.Ar), cortical area (Ct.Ar) and cortical area fraction (Ct.Ar/T.Ar). Cortical porosity is the volume of pores divided by the volume of cortical bone in the segmented region. Cortical thickness describes the average cortical thickness in the selected region. Total area is an average of the sum of both marrow area and cortical area, or all area inside the periosteal surface. The cortical area fraction is found by taking the cortical area (endosteal to periosteal surface) divided by the total area.

In-vivo microCT can also be used to measure structural parameters pre-treatment and post-treatment in mice, but leads to further complications for data interpretation [26]. By taking microCT images of live mice, the mice are exposed to additional radiation from the scans themselves [27].

Bone is an anisotropic material and structural changes contribute to strength in different ways depending on the axis a load is applied to. Cortical bone is stronger in compression than tension, under higher strain rates and with longitudinal loads [28]. Trabecular bone transfers mechanical loads from articular surface to the cortical bone. Generally, this bone is also less mineralized, and forms an interconnected network within the bone marrow [29].

Bone Material Properties Assessment in a Mouse Model:

Fourier transform infrared spectroscopy (FTIR), Raman Spectroscopy and nanoindentation are three techniques used to characterize bone quality. FTIR illuminates a sample with infrared radiation and measures the vibrational dipole moment changes representative of the overall configuration of atoms and functional groups. The result is an absorption spectra that can be used to determine characteristic components of bone (Figure 1.4) [30]. Raman spectroscopy uses a laser to excite molecules. The vibrational motion can cause light to lose energy and scatter at longer wavelengths. These shifts in frequency are used to identify composition of the tissue (Figure 1.5) [10]. Nanoindentation measures Young's modulus by applying a force to a material using a well-defined instrument tip and measuring displacement (or vice versa) [31].

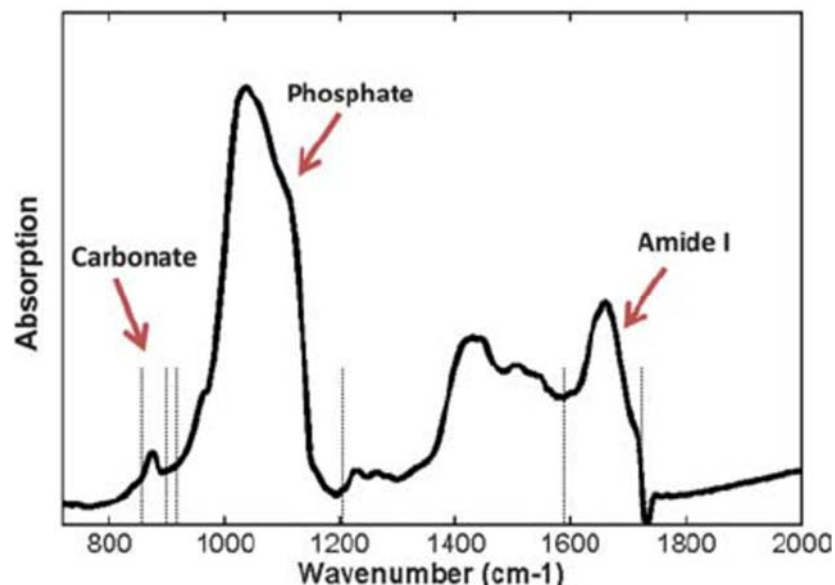


Figure 1.4: Example FTIR spectrum of bone. Reproduced from Kобрina et al. 2010 [2]

Both FTIR and Raman are used to quantify major bone material parameters including mineral to matrix ratio, carbonate to phosphate ratio and crystallinity/mineral maturity [30]. Mineral matrix ratio represents the amount of mineral normalized to the amount of collagen

present. Similarly, carbonate to phosphate ratio represents the amount of carbonate substitution in the crystal lattice and has been shown to correlate with fracture risk [32]. Crystallinity measures the maturity of the mineral and correlates with yield stress and hardness [32].

For FTIR images, mineral to matrix ratio is calculated as the ratio of the integrated phosphate band (900-1200 cm^{-1}) to any of the amide bands, but usually the Amide 1 band (1585-1725 cm^{-1}). Carbonate to phosphate ratio is found by taking the integrated area of the carbonate band (850-900 cm^{-1}) divided by the phosphate band (900-1200 cm^{-1}). Crystallinity is found by taking the 1030 cm^{-1} peak divided by the 1020 cm^{-1} peak [30].

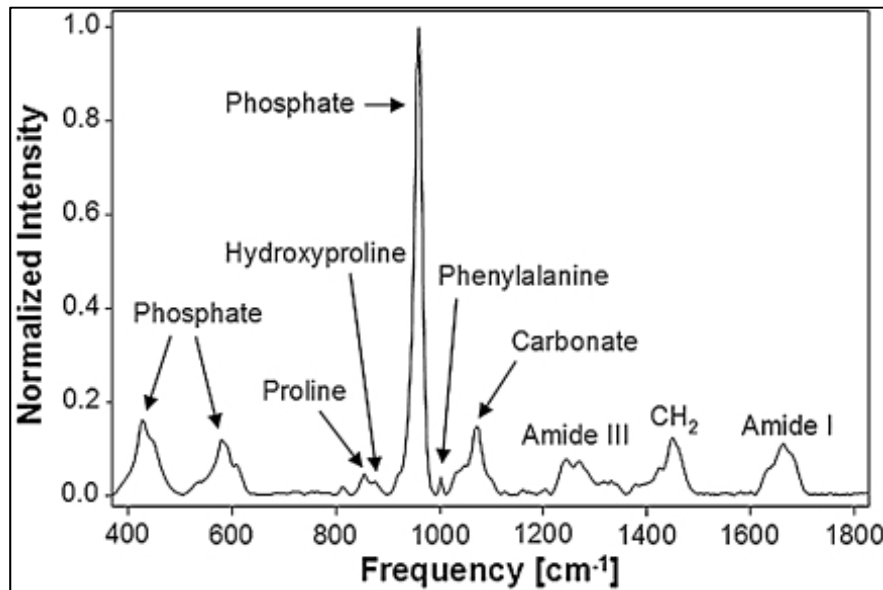


Figure 1.5: Example Raman spectrum of bone. Reproduced from Morris and Mandair 2011 [10]

For Raman spectroscopy, the mineral to matrix ratio is calculated based off a several different measures for matrix bands, including amide I, amide III, proline, hydroxyproline and phenylalanine. In this discussion, mineral to matrix ratio is calculated as the ratio between the primary phosphate peak (959 cm^{-1}) and the proline peak (855 cm^{-1}), due to the fact that the proline peak is less influenced by laser polarization [10]. Raman measures for carbonate to phosphate ratio are found by taking the carbonate intensity (1070 cm^{-1}) divided by the phosphate

peak intensity (959 cm^{-1}). Crystallinity is quantified by taking the full-width half-maximum for the phosphate band at 959 cm^{-1} [10].

Raman spectroscopy offers the advantages of not requiring specimen preparation (embedding/maximum thickness etc.) and greater spatial resolution [33]. On the other hand, Raman spectra can be influenced by laser polarization while this is not an issue with FTIR. Certain vibrations in Raman peaks are known to be weaker than in FTIR and vice versa. Therefore, these techniques are often used together [34]. Each of the parameters assessed using FTIR and Raman Spectroscopy have been correlated to bone strength. Increases in mineral to matrix ratio correlate with increased stiffness and brittleness, while decreased carbonate to phosphate ratio correlates with higher strain, greater maximum load and greater post-yield toughness [35]. Crystallinity is correlated with tissue-level strength and is inversely correlated to yield strain, ductility and fatigue-life [36, 37]. Since the publication of the Oliver and Pharr method, nanoindentation has emerged as a relevant test for determining the Young's modulus of

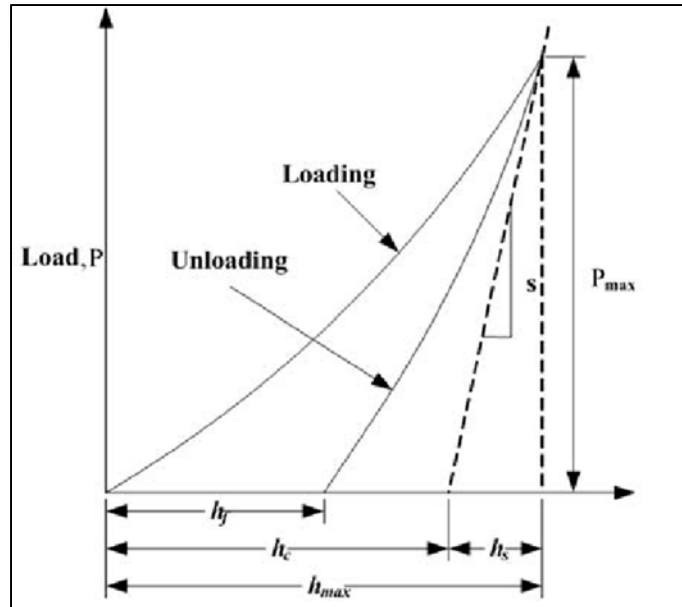


Figure 1.6: Example load vs. displacement plot with parameters used for Oliver-Pharr method calculation of Young's Modulus. Reproduced from Oliver and Pharr 1992 [7]

bone tissue [7]. The Oliver Pharr method allows for calculation of Young's modulus from the slope of the unloading curve based on the assumption that the unloading response is purely elastic.

The reduced modulus is calculated directly from the unloading curve by the equation $E_r = \frac{S\sqrt{\pi}}{2\sqrt{A}}$ where S is the slope of the upper portion of the unloading data and A is the projected area of the elastic contact [7]. The contact area is specific to tip geometry. In this case, a Berkovich tip, a three-sided pyramid, is used for indentation. The area function for a perfect Berkovich indenter is $A(h_c) = 24.5h_c^2$ where h_c is the contact depth. Prior to gathering data, the Berkovich tip area function is generally calibrated using fused silica. The Young's Modulus can be calculated from the reduced modulus (E_r) based on the equation $\frac{1}{E_r} = \frac{1-\nu^2}{E} + \frac{1-\nu_i^2}{E_i}$ where E and ν are the Young's modulus and Poisson's ratio for the specimen and E_i and ν_i are the same parameters for the indenter (see Figure 1.6). The reduced modulus is often reported instead of Young's modulus. It is important to keep in mind that sample preparation, hydration state, tip geometry, gender, age and loading conditions can all have an effect on collected data [31].

Studies have shown a decrease in Young's modulus in osteoporotic bone compared to healthy controls [38]. However, the relationship between Young's modulus and mechanical behavior is not straightforward. By taking into account bone composition through Raman spectroscopy and FTIR in combination with nanoindentation, the relationship between material quality, modulus and strength can be more accurately assessed. For example, an increased mineral to matrix ratio has been correlated with an increase in bone strength [39]. However, if additional mineral is not formed in a connected network that can transmit strain, there will not be a corresponding increase in Young's modulus. An increase in both mineralization and modulus

would suggest an increase in strength. A schematic of parameters that contribute to bone strength can be found in Figure 1.7.

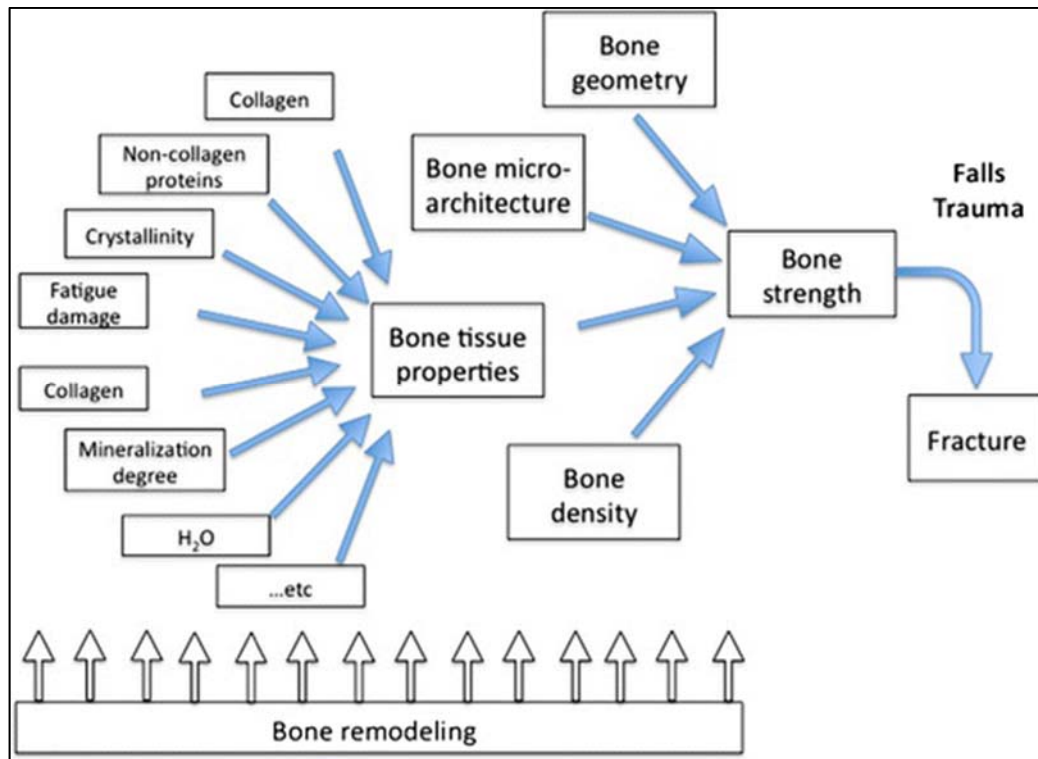


Figure 1.7: Factors that contribute to bone strength and fracture risk.
Reproduced from Torres-del-Piego et al. 2013 [8]

Postmenopausal Osteoporosis

Osteoporosis is defined clinically as a bone mineral density is 2.5 standard deviations or more below the mean for young normal people as measured by DEXA [40]. Each year in the United States of America, osteoporosis is responsible for 1.5 million fractures [41]. A majority of these fractures occur in postmenopausal women due to a decline in estrogen [42]. Estrogen inhibits RANKL-stimulated osteoclast differentiation and can induce osteoclast apoptosis [43]. Estrogen has also been shown to indirectly affect osteoclasts through suppressed RANKL production by osteoblastic, T and B-cells [44]. This results in accelerated bone resorption following a loss of estrogen [45].

In addition to increased resorption, there is also an increase in bone formation at the tissue level [45]. Estrogen inhibits osteoblast apoptosis and can increase osteoblast lifespan. However, the rate of formation is slower than the rate of bone resorption, leading to a net bone loss at each BMU [40].

Postmenopausal osteoporosis is studied in a mouse model through ovariectomy (OVX), or removal of the ovaries [46]. A longitudinal study in C57BL/6 mice 14 weeks of age at ovariectomy reports a 7% decline in BV/TV after two weeks and a 38% decline after eight weeks post-surgery [47].

Bisphosphonates

Bisphosphonates are a class of drugs that prevent bone loss by inhibiting bone resorption [48]. A bisphosphonate tightly adheres to the surface of the bone and inhibits the farnesyl pyrophosphate synthase enzyme necessary for cytoskeleton formation in osteoclasts [48]. The current bisphosphonates approved to treat postmenopausal osteoporosis include alendronate, ibandronate, risedronate and zoledronate. Of the bisphosphonates, zoledronate has the highest affinity and longest half-life in bone [49]. However, there are some concerns regarding their side effects and potential problems with long-term use [48]. Atypical femoral fracture and osteonecrosis of the jaw have recently been linked to long-term use, although these risks are estimated to occur in less than 0.00002% of the population [48].

Radiation Therapy and Bone

Radiation therapy for cancer treatment has been shown to increase fracture risk [3, 50-52]. A retrospective cohort study including 6428 women aged 65 years and older showed that women who underwent radiation therapy were more likely to have a pelvic fracture than women who did not undergo radiation therapy [3]. Additionally, 90% of those fractures were hip

fractures [3]. Pelvic fractures are particularly concerning due to the high mortality rate associated with their occurrence [53]. The one year mortality rate following hip fracture in patients 65 years of older is 24% for females and 48% for males [53]. In addition to local bone loss, radiation therapy also induces systemic declines in bone mineral density [54-57].

There is clinical evidence that premenopausal women with gynecological tumors may experience a premature and permanent menopause as a result of damage to the ovaries from radiation therapy [58]. The effects of an early onset estrogen deficiency may have a more severe impact on bone density due to the fact that these patients likely have not reached peak bone mass.

Ionizing radiation has enough energy to remove electrons from atoms and break molecular bonds [59]. This can cause damage to DNA, RNA, cell organelles and more. There are also indirect effects from ionizing radiation including the generation of reactive oxygen species created from ionization of water molecules. These reactive oxygen species can further damage DNA and destroy cell structures leading to cell death [60]. Radiation quickly diminishes vascular supply to bone through perivascular edema, small vessel hemorrhage and decreased perfusion [60]. Additionally, marrow fibrosis can develop and decrease hematopoiesis long term [60]. Both osteoblasts and osteoclasts are affected by radiation. Almost immediately following radiation, there is a decline in osteoblast number [61]. Initially, there is an increase in osteoclast number that leads to an increase in bone resorption after radiation exposure [62]. In the long term, there is a loss of osteoclasts due to damage of osteoclast progenitor cells [63].

Structural and material changes in bone resulting from ionizing radiation are dose dependent [55, 62-64]. The Fowler equation is used to calculate biologically effective dosing for mouse studies [65]. Biologically effective dose (BED) is the total dose required to give the same

log cell kill as the schedule being studied, at an infinitely low dose-rate or with infinitely small fractions spaced over time [65]. The relationship can be described through the Fowler equation $BED = T_d(1 + \frac{d}{(\alpha/\beta)})$ where T_d is the total physical dose, d is the dose-per-fraction and α/β depends on the tissue of interest and whether it is an early or late responding tissue. The α/β ratio can be calculated from cell survival curves by finding the dose where cell killing due to the linear and quadratic components are equal [65]. The number of fractions administered can also influence bone response. As radiation-induced cell damage occurs, other cells are recruited to clean up the damage, potentially leading to increased cell death upon further exposure [66].

Even radiation doses as low as 1 Gray (Gy) can significantly affect bone growth [64]. Experiments in mice have shown a single 2 Gy dose of X-rays leads to a 32% decrease in trabecular bone density after just one week in the proximal tibia [67]. Another mouse study showed a single 5 Gy dose of Cs-137 radiation led to a 40% decline in trabecular bone volume after 10 days and reached more than 45% decline by 56 days in the tibia [68]. While changes in material properties are not fully understood, a study by Gong et al. demonstrated that 20 Gy localized radiation in a mouse altered collagen crosslinking and mineralized matrix by one week following exposure [69]. FTIR studies have shown a decrease in mineral composition by 2 days following 5 Gy radiation exposure and persisting through at least 10 days [70]. Full characterization of the structural and material changes of bone following radiation therapy and long-term effects can lead to improved screening for potential therapeutics.

Hemophilia A and Bone

Hemophilia A is an X-linked disorder caused by an absent, deficient or defective plasma coagulation factor VIII [71]. Factor VIII is responsible for accelerating the rate of cleavage of factor X by activated factor IX during coagulation. In fact, factor VIII increases the rate of the

reaction several thousandfold. A diagram describing the coagulation pathways and where Factor VIII is required can be found in Figure 1.8. The disease can present in mild, moderate or severe forms depending on the level of factor VIII present in the plasma [71]. One of the hallmark symptoms of severe hemophilia patients is unprovoked bleeding into the joints (hemarthrosis) [71].

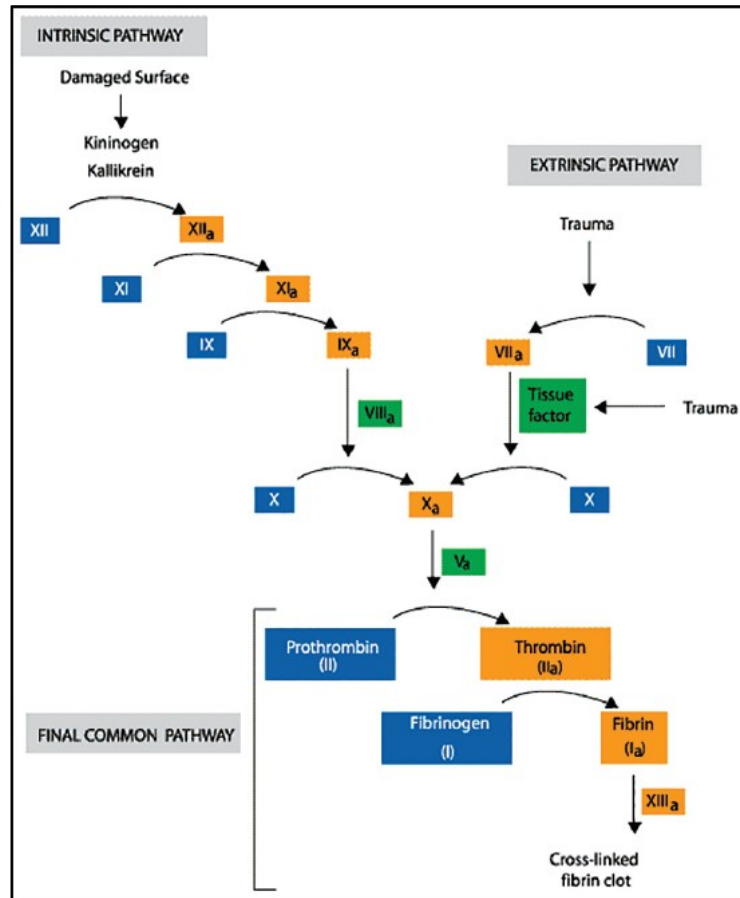


Figure 1.8: Overview of coagulation pathways. Reproduced from Goswami et al. 2014 [5]

Over time, repeated micro-hemorrhages into the joint will lead to joint arthropathy, characterized by synovial inflammation, osteophyte formation and cartilage degeneration [6]. In both adults and children with hemophilia, low bone density has been reported [72-76]. There are a number of factors contributing to the decline in bone mass including joint bleeding, lack of activity, low vitamin D and other infections, such as HIV [77]. A recent study showed that low

bone density in hemophilia patients also exists independently of joint bleeds and other factors [78].

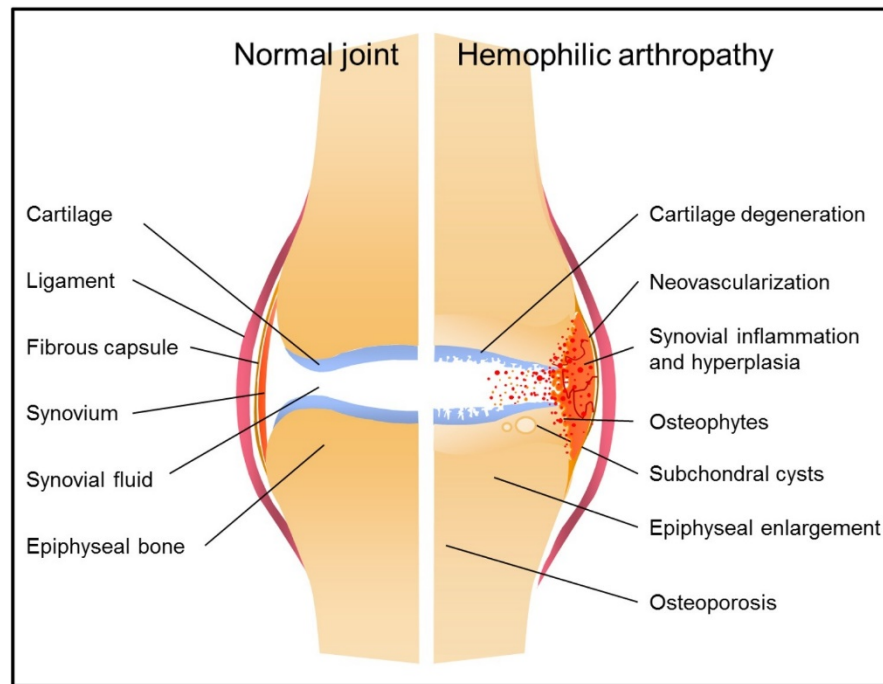


Figure 1.9: Comparison of hemophilic arthropathy to a normal joint. Reproduced from Pulles et al. 2017 [6]

Knee joint hemarthrosis is often modeled in factor VIII gene knockout mice by puncturing the knee joint capsule with a 30.5 gauge needle, followed by injection of 5 microliters of saline [79]. Recent investigations have shown a significant decrease of trabecular bone two weeks following knee hemarthrosis, but rapid calcification of joint soft tissues and cortical bone [79]. A timeline of the mineralization as well as identifying changes in structural and material properties could help elucidate targets for treatment.

Research Objectives

When it comes to determining fracture risk, both bone structure and material properties are essential for consideration. Structural parameters, such as bone volume and trabecular thickness, are often studied more frequently due to ease of access to imaging modalities and the ability to image in vivo. Finite element analysis can be used for simulated mechanical testing and

bone strength estimation based on these determined structural parameters. However, changes in bone composition and material properties resulting from disease states or treatment methods are just as critical in predicting bone function, but are more difficult to assess and interpret.

In Chapter 2, fractionated radiation therapy in a mouse model will be characterized by administering a biologically effective dose for cervical cancer treatment in humans. The added effect of induced menopause from radiation therapy on bone will also be explored through an ovariectomized mouse model. By quantifying the structural changes resulting from radiation therapy in a mouse model, potential therapeutics can then be evaluated.

In Chapter 3, the short and long term effects of zoledronate and concurrent fractionated radiation on bone morphology, compressive stiffness, composition and elastic modulus will be quantified. Bone health will be assessed through microCT, finite element analysis (FEA), fluorescent imaging, FTIR, Raman spectroscopy and nanoindentation. The results from this chapter can be used to inform clinical assessment of bisphosphonates for use during cancer treatment.

In Chapter 4, the structural and material properties of the femur and tibia will be assessed following knee joint hemarthrosis in both male and female mouse models. Three time points will be evaluated to understand the timeline of joint injury. The techniques developed for assessment of bone material properties from Chapter 2 will be used to inform experiment design. The results from this study can help elucidate the timeline of disrupted bone formation following knee hemarthrosis in male and female hemophilic mice and suggest potential mechanisms for therapeutic targets. Finally, key findings and future work will be presented in Chapter 5.

CHAPTER 2: A MOUSE MODEL FOR SKELETAL STRUCTURE AND FUNCTION CHANGES CAUSED BY RADIATION THERAPY AND ESTROGEN DEFICIENCY

Introduction

More than 110,000 women are diagnosed with a gynecological cancer each year in the United States [80]. As diagnosis and treatment of gynecological tumors have improved, so has the number of survivors. External beam radiation therapy is a common procedure used to treat gynecological tumors [81]. This treatment method typically requires the transmission of high energy, fractionated doses of x-rays to the pelvic region in an attempt to kill the cancer cells [81]. The dose targeted at the tumor can be as much as 50 to 55 Gray (Gy) x-rays throughout the course of treatment [82]. Healthy normal tissue, such as bone in the pelvic region and proximal femur, is exposed to x-rays as well, though at lower doses [51].

There is now a large population of patients who exhibit decreased bone density and increased fracture risk following external beam radiation therapy for cancer treatment. A 2005 study by Baxter et al. showed that postmenopausal women who received radiation therapy were more likely to experience a pelvic fracture, with the 5-year cumulative chance of fracture as high as 14% for anal cancer patients [3]. Additionally, 90% of these fractures were hip fractures [3]. A 2017 study determined that the rate of pelvic insufficiency fracture following radiation therapy for cervical cancer was 15.8% [52]. Of the patients who fracture, the fractures occur early: 38% of the women fracture within one year and 83% fracture within two years [83]. The one year mortality rate following hip fracture in patients 65 years or older is 24% for females and 38% for males [53].

Previous experiments in mice have shown that even a single dose of 2 Gy x-rays can lead to a 32% decrease in trabecular bone density after just one week in the proximal tibia [67]. Willey et al. showed that this loss is attributed to an early increase in osteoclast number evident at three days following a single 2 Gy x-ray exposure [62]. Similarly, three weeks following a single 1 Gy dose of x-rays resulted in a 21% decrease in bone volume fraction (BV/TV) in the mouse distal femur [84]. Decreases in bone density and strength correspond to an increased risk of fracture.

There are other confounding factors that may influence bone fragility following cancer treatment. Postmenopausal osteoporosis is a well-documented condition that leads to a decline in bone density due to a decrease in estrogen [85]. During the menopausal transition phase, an estimated 10% areal bone mineral density (aBMD) is lost in women [86]. Areal BMD is measured using Dual-energy X-ray absorptiometry (DEXA) and provides a two dimensional measure for bone mass in a projected area [87]. Elderly women lose approximately 1.2% areal BMD per year and elderly men lose about 0.8% areal BMD [88]. While areal BMD provides valuable information on bone strength, this measure is limited in describing specific changes to trabecular architecture and is influenced by bone size. On the other hand, quantitative computed tomography (qCT) provides measures for volumetric (3D) bone density (vBMD), as well as separate data for cortical and trabecular bone compartments [89]. Volumetric measures for cortical and trabecular bone mineral density are two-fold higher in elderly women than men [88].

There is clinical evidence that pre-menopausal women with gynecological tumors may experience a premature and permanent menopause as a result of damage to the ovaries caused by radiation therapy [11]. The effects of this early-onset estrogen deficiency on bone health may be more severe due to the fact that these patients likely have not reached peak bone mass. In order to simulate radiation-induced estrogen deficiency in a mouse model, an ovariectomy procedure is

performed two days prior to the first dose of radiation. Due to anatomical differences in mouse and human ovaries, mouse hindlimb radiation would not result in a loss of mouse ovarian function, as the ovaries are positioned outside the radiation field. In contrast, human ovaries are often located within the pelvic radiation field [58].

Menopause is commonly modeled in mice using the ovariectomy procedure. Just as occurs with menopause in women, ovariectomy in mice causes bone loss by increasing osteoclast number and lifespan [90-92]. Eight weeks following ovariectomy, female C57BL/6 mice lose up to 35% of their trabecular volumetric bone mineral density in the distal femur compared to Sham-operated controls. Just two weeks following the ovariectomy procedure, female C57BL/6J wild-type mice have been shown to lose 18% bone volume fraction (BV/TV) [90].

Previous studies have investigated the effect of induced ovariectomy performed two months prior to a single radiation dose on bone remodeling and distal femur bone volume fraction [93]. This model simulates the intentional disruption of ovarian function in order to induce estrogen deficiency in women undergoing treatment for estrogen-sensitive cancers. A key difference between this Hui et al. model and our study is the timeline between ovariectomy and radiation. In the Hui et al. study, mouse ovaries were removed fifty-seven days prior to radiation therapy [93]. There are several ways estrogen deficiency can occur during cancer treatment that may have a similar impact on bone, including chemotherapy, estrogen blockers or hysterectomy.

The overall goal of this study is to quantify bone architectural and functional changes in a mouse model simulating a clinically relevant, radiation-induced estrogen deficiency in pre-menopausal women receiving treatment for gynecological tumors. Specifically, we aim to characterize bone density, morphometric alterations and functional changes in order to establish a model to test potential bone therapeutics. This paper reports results of ovariectomy combined with

modeled radiation therapy on mouse bone structure and function using DEXA, micro-computed tomography (microCT) and computational mechanical testing via finite element analysis (FEA). We hypothesize that bone loss resulting from concurrent ovariectomy and fractionated radiation therapy will result in more drastic trabecular bone degradation than ovariectomy completed months prior to radiation. The implications of this study provide insight into the clinical condition of women undergoing radiation therapy for gynecological tumors.

Materials and Methods

X-ray Dose Validation

In order to determine whether radiation should be given in fractions or a single biologically effective dose, a preliminary dosing study was performed. Thirty-six female C57BL/6N mice were purchased from Charles River (Charles River Laboratories, Morrisville, NC). All mice were fourteen weeks of age at the start of the study with food and water available ad libitum throughout the study. All investigations were approved by the University of North Carolina, Chapel Hill Institutional Animal Care and Use Committee.

The mice were divided into three groups with twelve mice in each group (n=12). The first group received a single 18 Gray dose of X-rays to the hindlimbs on Day 0 and the second group received a 6 Gray dose of X-rays to the hindlimbs on Days 0, 3 and 7 (3x6 Gy). The final group served as a control and did not undergo irradiation. Mice were irradiated while under anesthesia (1.5% isoflurane) with a single field of 320 kV(p) x-rays at a dose rate of 0.5 Gy/min to the hindlimbs only (X-RAD 320, Precision X-Ray, North Branford, CT). All mice were humanely euthanized on Day 14 and the left hindlimb was collected at dissection for Microcomputed Tomography (MicroCT) analysis. The left tibiae were cleaned of soft tissue, fixed in 10% formalin for 48 hours and then placed into 70% ethanol for storage.

Proximal Tibia MicroCT for Dose Validation

MicroCT scans of the left tibiae were taken at 10-micron isotropic voxel size (μ CT80; Scanco Medical AG, Brüttisellen, Switzerland). The scans were acquired using a 70-kVp peak X-ray tube potential, a 0.5 mm Al filter, and an integration time of 800 ms to reduce beam hardening effects and improve the signal-to-noise ratio. Scanco software was used to analyze and quantify bone microarchitectural parameters from contoured regions. All contouring was performed semi-automatically to separate trabecular and cortical compartments. For the proximal tibia, a 1 mm section of the metaphysis just below the growth plate was chosen as the contour region. Trabecular bone volume fraction (BV/TV) was quantified for comparison between mouse groups.

OVX and Radiation Study

Animals and Study Design

Thirty-two female C57BL/6N mice were purchased from Charles River (Charles River Laboratories, Morrisville, NC). All mice were thirteen weeks of age at the start of the study with food and water available ad libitum throughout the study. All investigations were approved by the University of North Carolina, Chapel Hill Institutional Animal Care and Use Committee.

Sixteen mice had their ovaries surgically removed (OVX) and the other sixteen mice received a sham operation (Sham). The OVX and Sham surgeries were performed by Charles River Laboratories two days prior to the first irradiation procedure. Within each operation group, eight mice (n=8) were irradiated (IRR) and the other eight were not (NR). The ovariectomy procedure served as the start of the experiment (Day 0). The irradiated mice received a 6 Gy dose of X-rays to the hindlimbs at Day 2, Day 4 and Day 7 (18 Gy total). Mice were irradiated while under anesthesia (1.5% isoflurane) with a single field of 320 kV(p) x-rays at a dose rate of 0.5 Gy/min to the hindlimbs only (X-RAD 320, Precision X-Ray, North Branford, CT). The mouse radiation

dose was calculated based on the Fowler equation (biologically effective dose or BED) for the estimated 27 Gy total dose to each hip throughout radiation therapy (30 fractions of 0.9 Gy X-rays) for cervical cancer in women [65]. For the human BED calculation, the total dose was 27 Gy, the fraction dose was 0.9 Gy and the alpha to beta ratio was estimated to be 8, for a BED of 30.4 Gy. The alpha to beta ratio estimate was based on multiple studies indicating that bone is a very acute responding tissue, in terms of rapid bone loss and increased osteoclast activity [94-96]. For the animal calculation, the total dose was 18 Gy, the fraction dose was 6 Gy and the alpha to beta ratio was also 8, for a BED of 31.5 Gy.

Tissue Collection

Each mouse was weighed, then humanely euthanized on Day 35 (28 days following the final dose of radiation). The vertebral column, left hindlimb and right hindlimb were collected at dissection for further analysis. Tibiae, femora and vertebrae were cleaned of soft tissue and fixed in a solution of 10% formalin. After 48 hours, the bones were placed in 70% ethanol for storage.

Dual-energy X-ray absorptiometry (DEXA)

DEXA images (Lunar PIXImus, GE Lunar Corp.) were acquired at Day 2, Day 21 and Day 35 while mice were sedated using isoflurane. This scanner uses a cone beam X-ray source generating energies of 35 and 80 keV and a flat 100 × 80 mm detector having individual pixel dimensions of 0.18 × 0.18 mm. Each mouse was placed in the prone position with legs moved away from the body for scanning. Lunar PIXImus software was used to determine bone density for each mouse. Two regions of interest were evaluated per mouse: whole body and hindlimb region only.

Microcomputed Tomography (MicroCT)

The right tibiae, right femora and vertebral column were removed from ethanol and cleaned of nonosseous tissue for further analysis. MicroCT scans of the right tibia, right femora and L1 vertebrae were taken at 10-micron isotropic voxel size (μ CT80; Scanco Medical AG, Brüttisellen, Switzerland). The scans were acquired using a 70-kVp peak X-ray tube potential, a 0.5 mm Al filter, and an integration time of 800 ms to reduce beam hardening effects and improve the signal-to-noise ratio. Scanco software was used to analyze and quantify bone microarchitectural parameters from contoured regions. All contouring was performed semi-automatically to separate trabecular and cortical compartments. For the proximal tibia, a 1 mm section of the metaphysis just below the growth plate was chosen as the contour region. For the femur, contouring was performed at a 0.5 mm section at the femoral midshaft. The entire vertebral body between the two endplates was contoured for the L1 vertebra. Trabecular bone parameters including bone volume fraction (BV/TV), connectivity density (Conn.D), trabecular number (Tb.N), trabecular thickness (Tb.Th), trabecular separation (Tb.Sp), structure model index (SMI), volumetric bone mineral density (vBMD), cortical porosity (Ct. Po), cortical area (Ct. Ar), marrow area (M. Ar) and total area (T. Ar) were quantified.

Finite Element Analysis

Example visual representations of each bone segment mesh used for finite element analysis can be found in Figure 2.1 (a-h).

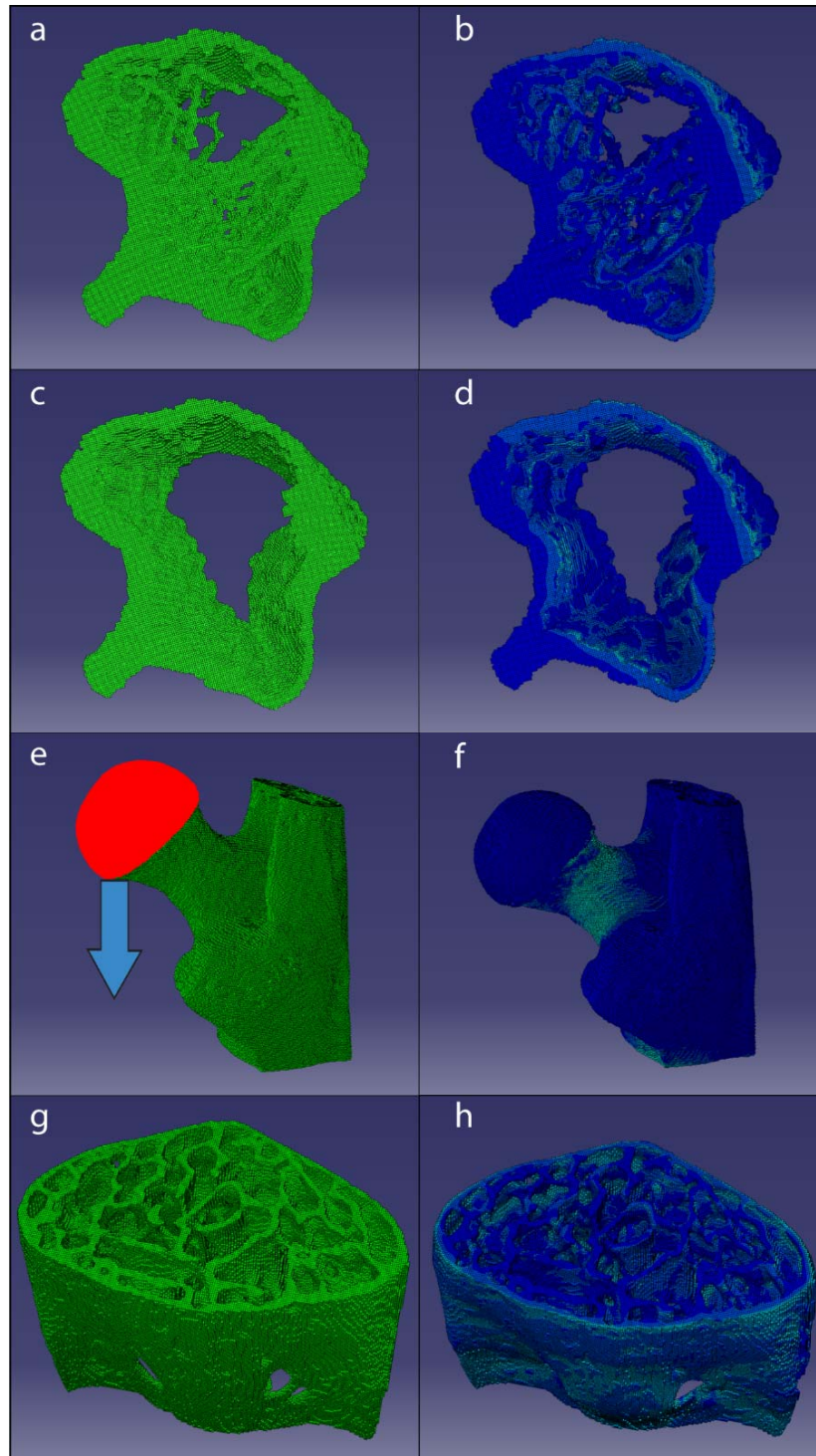


Figure 2.1: Example finite element analysis meshes for whole proximal tibia segment (a), loaded whole tibia (b), cortical proximal tibia segment (c), loaded cortical tibia (d), proximal femur mesh with nodes selected in red to be displaced (e), loaded femoral neck (f), L1 Vertebra (g) and loaded L1 Vertebra (h)

Proximal Tibia

The same 1 mm region of each proximal tibia used for microCT analysis was exported from the scanner and imported as a tetrahedral mesh into Abaqus software (Abaqus/CAE 6.9-EF1, Dassault Systems Simulia Corp, Providence, RI) for finite element analysis. For each individual bone section, homogenous material properties were applied to the tibia by assigning a Young's Modulus of 10 GPa and Poisson's Ratio of 0.3. Then, two nodes sets were created: one containing all nodes on the proximal end of the tibia segment and the other comprised of all distal nodes of the tibia segment. For the loading step, boundary conditions were applied to secure the distal end of the tibia while displacing the proximal end 50 microns (~5% strain) downward in the z-direction. The resultant force was measured and used to calculate compressive stiffness (force/displacement).

Proximal Femur

A 3.25 mm region of each right femur starting at the proximal end of the femoral head and continuing 3.25 mm (325 slices) distally was imported from the scanner into Abaqus as a tetrahedral mesh. Choosing a consistent place to measure the stress output is essential in ensuring that length will not play a role in the calculated bone stiffness. All nodes within the femoral head were selected manually and saved as a node set. The distal end nodes were also saved as a set. For the initial step, the boundary condition for these nodes were set to constrain both translation and rotation in all three directions, essentially holding the model fixed. For the loading step, the femoral head displacement was set to 50 microns in the downward z direction. The resultant force on the distal nodes was then measured.

Statistics

Significance was determined using SigmaPlot 12.0 (Systat Software Inc., San Jose, CA). The threshold for significance for all tests was set at a 5% probability of a type I error ($p=0.05$). All statistical comparisons were made using a two-way ANOVA. A Tukey post-hoc test was run to explore potential interactions and to maintain a Type 1 error of 0.05 across multiple comparisons (NR, IRR, OVX and Sham). This method was used to determine differences in final body mass, DEXA aBMD, DEXA BMC, microCT morphometric parameters and finite element analysis stiffness data.

Results

X-ray Dose Validation Study

Proximal Tibia MicroCT

At the proximal tibia, there was a 24% decline in BV/TV in the single 18 Gy dose mice compared to the non-irradiated control mice. For the 3x6 Gy dose mice, there was a 32% decrease in BV/TV compared to the non-irradiated control mice.

OVX and Radiation Study

Body Mass

At the start of the study (Day 0), there were no statistically significant differences in body mass between study groups. By Day 35, the OVX groups had gained more weight than Sham groups. The OVX+NR group body mass was 14% greater than the Sham+NR group and the OVX+IRR body mass was 7% greater than the Sham+IRR group body mass at sacrifice. More detailed body mass data can be found in Table 2.1.

DEXA

By the end of the study, there was a significant decrease in whole body and hindlimb aBMD resulting from ovariectomy in both irradiated (IRR) and non-irradiated (NR) mice, with no significant changes seen from irradiation. Hindlimb and whole body DEXA data can also be found in Table 2.1.

		SHAM-NR	SHAM-IRR	OVX-NR	OVX-IRR
Body Mass (grams)	Day 2	20.9 ± 0.7	20.8 ± 1.0	20.8 ± 1.4	20.7 ± 1.0
	Day 35	22.5 ± 0.8	23.0 ± 1.0	25.7 ± 1.5 [#]	24.7 ± 1.8 [#]
	Increase in body mass from start to end	1.6 ± 1.0	2.2 ± 1.0	4.9 ± 1.3 [#]	4.1 ± 1.6 [#]
Right Hindlimb aBMD (mg/cm²)	Day 2	52.4 ± 2.5	52.2 ± 1.7	53.1 ± 1.4	52.2 ± 2.5
	Day 21	56.6 ± 1.9	55.6 ± 2.0	54.4 ± 1.1 [#]	54.8 ± 1.7
	Day 35	57.1 ± 1.7	57.4 ± 1.1	54.1 ± 1.0 [#]	54.3 ± 1.5 [#]
Right Hindlimb BMC (mg)	Day 2	0.043 ± 0.003	0.042 ± 0.003	0.043 ± 0.003	0.041 ± 0.003
	Day 21	0.046 ± 0.003	0.045 ± 0.003	0.047 ± 0.002	0.046 ± 0.002
	Day 35	0.049 ± 0.003	0.048 ± 0.003	0.048 ± 0.003	0.046 ± 0.003
Whole Body aBMD (mg/cm²)	Day 2	47.7 ± 1.2	47.8 ± 1.7	46.8 ± 0.9	45.9 ± 2.7 [#]
	Day 21	50.0 ± 1.7	49.0 ± 0.9	47.2 ± 1.0 [#]	47.3 ± 1.3 [#]
	Day 35	49.7 ± 1.3	49.3 ± 0.8	47.0 ± 0.7 [#]	46.3 ± 1.2 [#]
Whole Body BMC (mg)	Day 2	0.41 ± 0.02	0.41 ± 0.03	0.41 ± 0.02	0.39 ± 0.04
	Day 21	0.40 ± 0.02	0.39 ± 0.02	0.38 ± 0.01	0.38 ± 0.02
	Day 35	0.43 ± 0.03	0.41 ± 0.01	0.39 ± 0.02 [#]	0.37 ± 0.03 [#]

Table 2.1: Body mass summary and DEXA aBMD results from right hindlimb and whole body. All data presented as mean ± standard deviation. * = significant effect of irradiation within Sham or OVX groups; # = significant effect of OVX within NR or IRR groups (p < 0.05)

Whole body aBMD

At Day 21, OVX+NR whole body aBMD was 6% lower than Sham+NR and OVX+IRR whole body aBMD was 3% less than Sham + IRR. At Day 35, OVX+NR whole body aBMD was 5% less than Sham+NR aBMD and OVX+IRR whole body aBMD was 6% less than Sham+IRR. There was a 9% decrease in bone mineral content (BMC) in the OVX+NR group compared to the

Sham+NR group and a 9% decrease in BMC in the OVX+IRR group compared to the Sham+IRR group on Day 35.

Right Hindlimb aBMD

On Day 21, there was a significant decrease (4%) in hindlimb aBMD for OVX+NR compared to Sham+NR. On Day 35, both OVX groups had a 5% decrease in hindlimb aBMD compared to Sham groups. There were no significant changes in right hindlimb BMC.

MicroCT Proximal Tibia

All microCT morphometry data can be found in Table 2.2 for the purpose of running statistics. Selected bone morphometric data for the proximal tibia have also been presented in Figure 2.3 (a-h). Example proximal tibia microCT images for each study group can be found in Figure 2.2.

MicroCT Analysis		SHAM-NR	SHAM-IRR	OVX-NR	OVX-IRR
Proximal Tibia Trabecular Analysis	BV/TV	0.090 ± 0.017	0.049 ± 0.007*	0.058 ± 0.012 [#]	0.034 ± 0.011 ^{*#}
	vBMD (mgHA/cm³)	78.1 ± 16.3	28.2 ± 9.24*	41.4 ± 11.6 [#]	6.67 ± 10.8 ^{*#}
	TMD	808 ± 17.0	794 ± 15.6	797 ± 23.9	794 ± 10.1
	Conn. Dens. (mm⁻³)	62.4 ± 16.4	19.6 ± 8.25*	36.9 ± 10.9 [#]	8.59 ± 6.69*
	Trab. Number (1/mm)	3.63 ± 0.326	2.53 ± 0.203*	3.15 ± 0.401 [#]	2.06 ± 0.308 ^{*#}
	Trab. Thickness (mm)	0.046 ± 0.002	0.050 ± 0.005*	0.041 ± 0.004 [#]	0.051 ± 0.003*
	Trab. Spacing (mm)	0.277 ± 0.02	0.396 ± 0.028*	0.322 ± 0.052	0.505 ± 0.071 ^{*#}
Proximal Tibia Cortical Analysis	BV/TV	0.926 ± 0.015	0.951 ± 0.006*	0.906 ± 0.033	0.931 ± 0.020*
	vBMD (mgHA/cm³)	718.9 ± 31.7	777.4 ± 15.6*	677.1 ± 43.5 [#]	739.4 ± 29.9 ^{*#}
	TMD	847 ± 25.8	879 ± 15.3*	822 ± 30.7 [#]	863 ± 18.8*
	Cortical Porosity	0.074 ± 0.015	0.049 ± 0.006*	0.094 ± 0.033	0.069 ± 0.020*
	Cortical Thickness (mm)	0.117 ± 0.012	0.159 ± 0.008*	0.102 ± 0.005 [#]	0.136 ± 0.007 ^{*#}
Midshaft Femur Cortical Analysis	BV/TV	0.904 ± 0.020	0.898 ± 0.014	0.900 ± 0.014	0.886 ± 0.022
	vBMD (mgHA/cm³)	1007.9 ± 28.5	1001.8 ± 26.4	994.6 ± 21.7	984.9 ± 21.9
	Cortical Porosity	9.65 ± 2.00	10.2 ± 1.43	10.0 ± 1.39	11.4 ± 2.24
	Cortical Thickness (mm)	0.181 ± 0.011	0.174 ± 0.007	0.170 ± 0.004 [#]	0.170 ± 0.004
	Marrow Area (mm²)	0.781 ± 0.055	0.806 ± 0.033	0.854 ± 0.059 [#]	0.852 ± 0.049
	Total Area (mm²)	1.48 ± 0.081	1.48 ± 0.046	1.53 ± 0.064	1.53 ± 0.057
	BA/TA	0.473 ± 0.018	0.456 ± 0.014*	0.443 ± 0.016 [#]	0.442 ± 0.014
	Cortical Area (mm²)	0.701 ± 0.041	0.677 ± 0.030	0.679 ± 0.014	0.675 ± 0.018
L1 Vertebra Trabecular Analysis	BV/TV	0.240 ± 0.027	0.219 ± 0.033	0.170 ± 0.014 [#]	0.162 ± 0.022 [#]
	vBMD (mgHA/cm³)	201.8 ± 20.8	182.3 ± 29.4	141.2 ± 12.7 [#]	135.4 ± 21.7 [#]
	TMD	781 ± 15.7	764 ± 23.8	744 ± 18.0 [#]	745 ± 29.5
	Conn. Dens. (mm⁻³)	194.6 ± 25.7	179.8 ± 17.1	168.2 ± 26.8 [#]	153.7 ± 14.3 [#]
	Trab. Number (1/mm)	4.65 ± 0.394	4.55 ± 0.336	4.15 ± 0.272 [#]	4.08 ± 0.252 [#]
	Trab. Thickness (mm)	0.048 ± 0.001	0.046 ± 0.002*	0.041 ± 0.001 [#]	0.041 ± 0.002 [#]
	Trab. Spacing (mm)	0.204 ± 0.020	0.209 ± 0.016	0.234 ± 0.016 [#]	0.238 ± 0.017 [#]

Table 2.2: MicroCT bone morphometry data for proximal tibia, midshaft femur and L1 vertebra. All data presented as mean ± standard deviation. *= significant effect of irradiation within Sham or OVX groups; # = significant effect of OVX within NR or IRR groups (p<0.05)

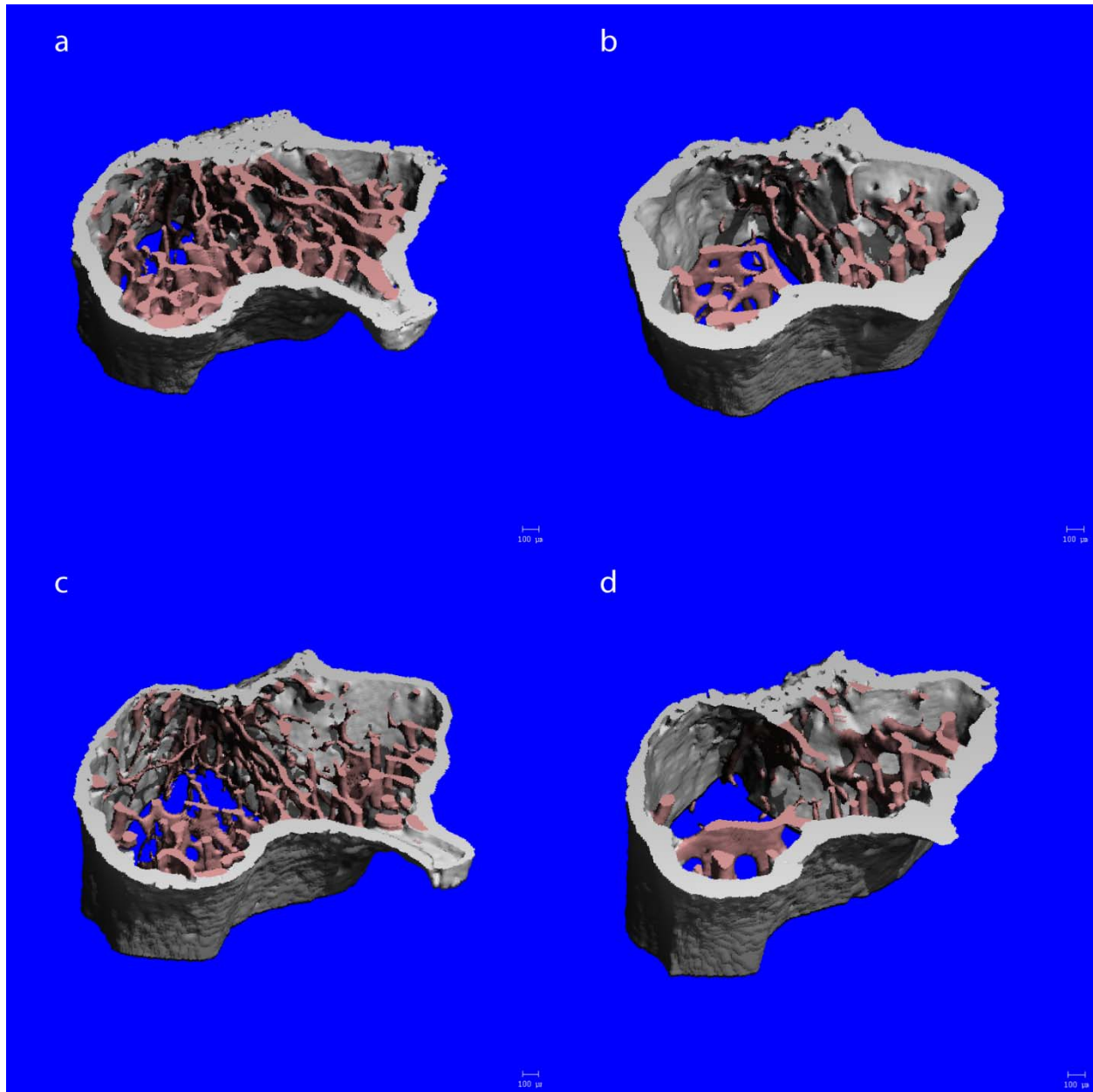


Figure 2.2: Example MicroCT scans of proximal tibia segment showing trabecular bone in pink and cortical bone in gray for Sham-NR mouse (a), Sham-IRR mouse (b), OVX-NR mouse (c) and OVX-IRR mouse (d)

Proximal Tibia Trabecular Morphometry (Figure 2.3a-2.3d)

In the proximal tibia region, both radiation and ovariectomy had an adverse effect on trabecular microarchitecture. BV/TV in the Sham+IRR group was 46% less than the Sham+NR group and OVX+IRR group BV/TV was 41% less than the OVX+NR group. There was a 36%

decline in BV/TV in the OVX+NR group compared to the Sham+NR group and a 30% decrease in BV/TV for the OVX+IRR group versus the Sham+IRR group.

Volumetric bone mineral density (vBMD) decreased 64% in Sham+IRR mice compared to Sham+NR mice and 84% in OVX+IRR mice compared to OVX+NR mice. Similarly, there was a 47% decline in vBMD for OVX+NR mice compared to Sham+NR mice and a 76% decrease in vBMD from OVX+IRR mice relative to Sham+IRR mice.

Connectivity density decreased 69% in the Sham+IRR group compared to the Sham+NR group and 77% in OVX+IRR group versus OVX+NR group. Within NR mice only, there was a 41% decrease in connectivity density from OVX compared to the Sham group.

There was a 10% increase in trabecular thickness in Sham+IRR mice compared to Sham+NR mice and a 24% increase in trabecular thickness from OVX+IRR mice compared to OVX+NR mice. On the other hand, the OVX+NR group had a 10% decline in trabecular thickness compared to the Sham+NR group.

Trabecular number decreased 30% in the Sham+IRR group versus the Sham+NR group and decreased 35% in the OVX+IRR group versus the OVX+NR group. The OVX+NR group resulted in a 13% decline in trabecular number compared to the Sham+NR group and a 19% decline in OVX+IRR compared to the Sham+IRR group.

Proximal Tibia Cortical Morphometry (Figure 2.3e-2.3h)

Cortical porosity decreased 33% in Sham+IRR mice compared to Sham+NR mice and decreased 26% in OVX+IRR group versus OVX+NR group. Changes in cortical porosity from both OVX groups compared to Sham groups were not statistically significant.

There was an 8% increase in vBMD in Sham+IRR mice compared to Sham+NR mice and a 9% increase in vBMD in the OVX+IRR mice compared to the OVX+NR mice. On the other

hand, vBMD in the OVX+NR group decreased 6% versus the Sham+NR group and decreased 5% in the OVX+IRR group compared to the Sham+IRR group.

Tissue Mineral Density (TMD) increased 4% in Sham+IRR mice compared to Sham+NR mice and increased 5% in the OVX+IRR mice versus OVX+NR mice. There was a 3% decrease in TMD in OVX+NR group compared to the Sham+NR group, but no significant change in the IRR mice.

Sham+IRR mice had a cortical thickness 36% greater than Sham+NR mice and OVX+IRR mice had a cortical thickness 33% greater than OVX+NR mice. Conversely, cortical thickness decreased 12% in OVX+NR mice compared to Sham+NR mice and decreased 14% in OVX+IRR mice relative to Sham+IRR mice.

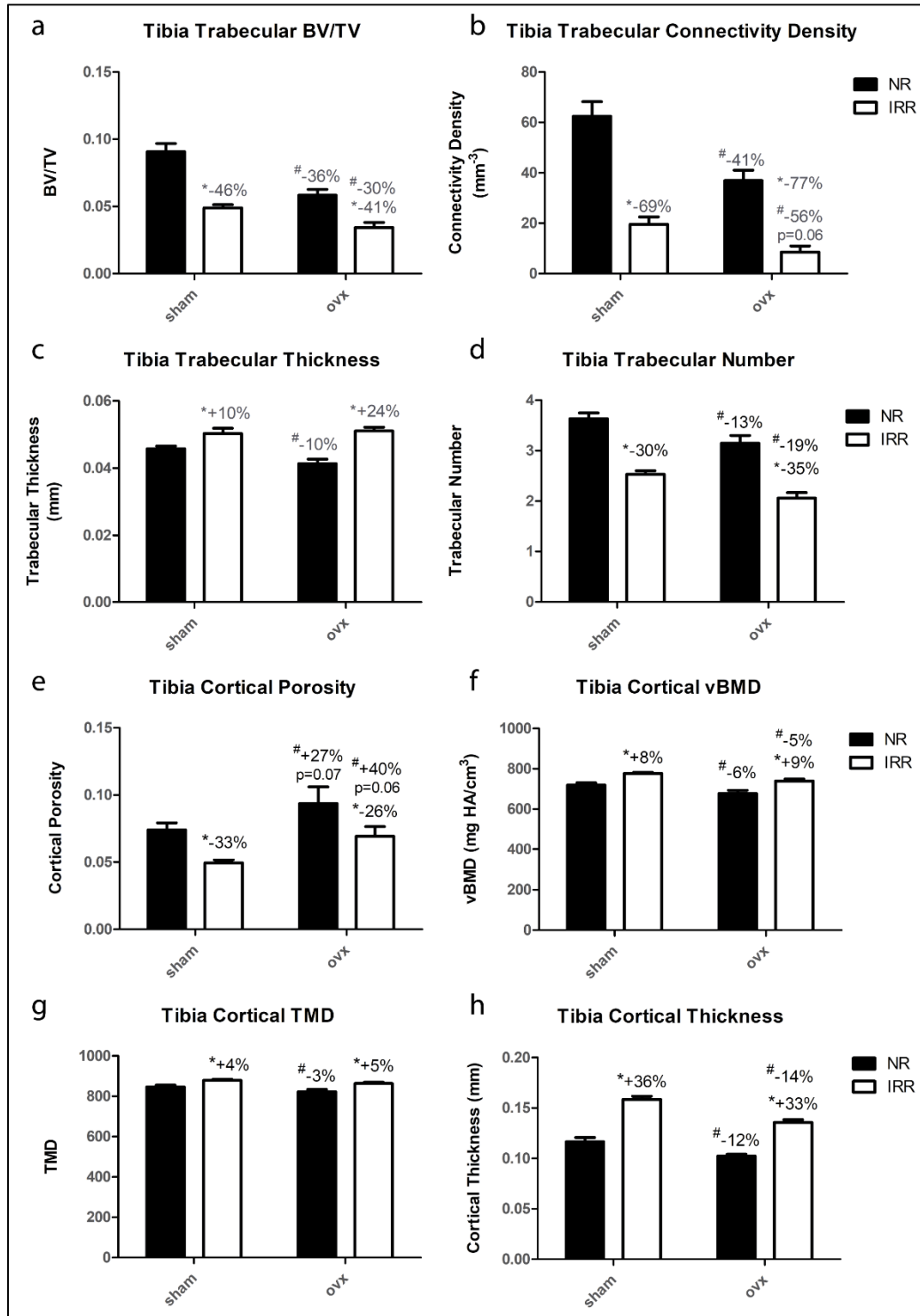


Figure 2.3: Graphs for MicroCT morphometry data for the proximal tibia segment including trabecular BV/TV (a), trabecular connectivity density (b), trabecular thickness (c), trabecular number (d), cortical porosity (e), cortical vBMD (f), cortical tissue mineral density (g) and cortical thickness (h). Error bars indicate standard error of the mean.

*=significant effect of irradiation within Sham or OVX groups; #=significant effect of OVX within NR or IRR groups (p<0.05)

Proximal Tibia Finite Element Analysis

Simulated compression testing using finite element analysis was performed on the isolated cortical compartment, trabecular compartment and whole bone (trabecular+cortical) segment. Proximal tibia FEA results are also presented in Figure 2.4.

Proximal Tibia Trabecular Bone Stiffness

Trabecular bone stiffness declined 47% in Sham+IRR mice compared to Sham+NR mice and declined 40% in OVX+IRR mice compared to OVX+NR mice. OVX+IRR trabecular bone stiffness was 21% less than Sham+IRR stiffness.

Proximal Tibia Cortical Bone Stiffness

In the isolated cortical bone segment, cortical stiffness increased 29% in Sham+IRR mice compared to Sham+NR mice and increased 32% in OVX+IRR mice compared to OVX+NR mice. Cortical stiffness declined 17% in OVX+NR group versus Sham+NR group and declined 15% in the OVX+IRR group relative to the Sham+IRR group.

Proximal Tibia Whole Bone Stiffness (Trabecular and Cortical Combined)

For the whole proximal tibia segment, there was a 10% increase in stiffness in the Sham+IRR mice relative to the Sham+NR mice and a 15% increase in stiffness in the OVX+IRR mice compared to the OVX+NR mice. Whole bone stiffness in OVX+NR mice was 18% less than Sham+NR mice and OVX+IRR stiffness was 14% less than Sham+IRR stiffness.

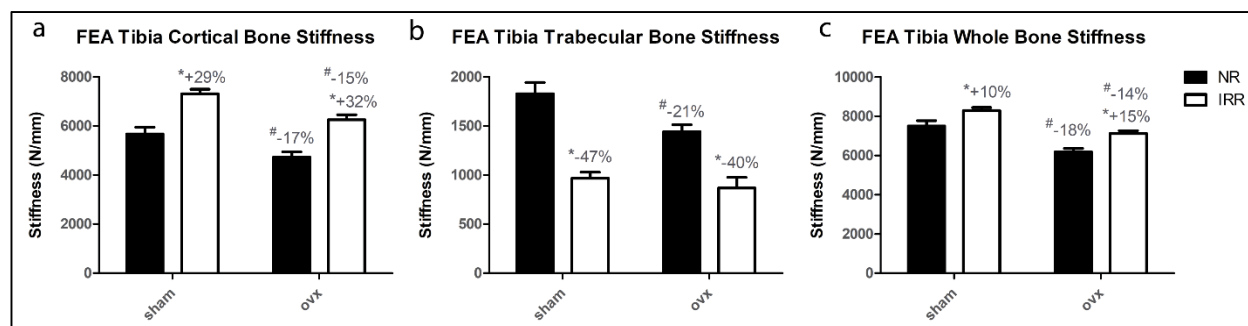


Figure 2.4: Graphs for proximal tibia finite element analysis data including proximal tibia cortical stiffness (a), proximal tibia trabecular stiffness (b) and whole proximal tibia segment stiffness (c). Error bars indicate standard error of the mean. *= significant effect of irradiation within Sham or OVX groups; # = significant effect of OVX within NR or IRR groups ($p < 0.05$)

MicroCT Midshaft Femur

Midshaft Femur Cortical Morphometry

At the midshaft of the femur, there were no statistically significant changes in cortical porosity for any groups. The only significant change in cortical thickness was a 6% decline in thickness in OVX+NR mice versus Sham+NR mice. The marrow area at the midshaft of the femur increased 9% in the OVX+NR group compared to the Sham+NR group. However, there were no statistically significant changes seen in cortical area or total area. Selected morphometry data for the midshaft femur can be found in Figure 2.5.

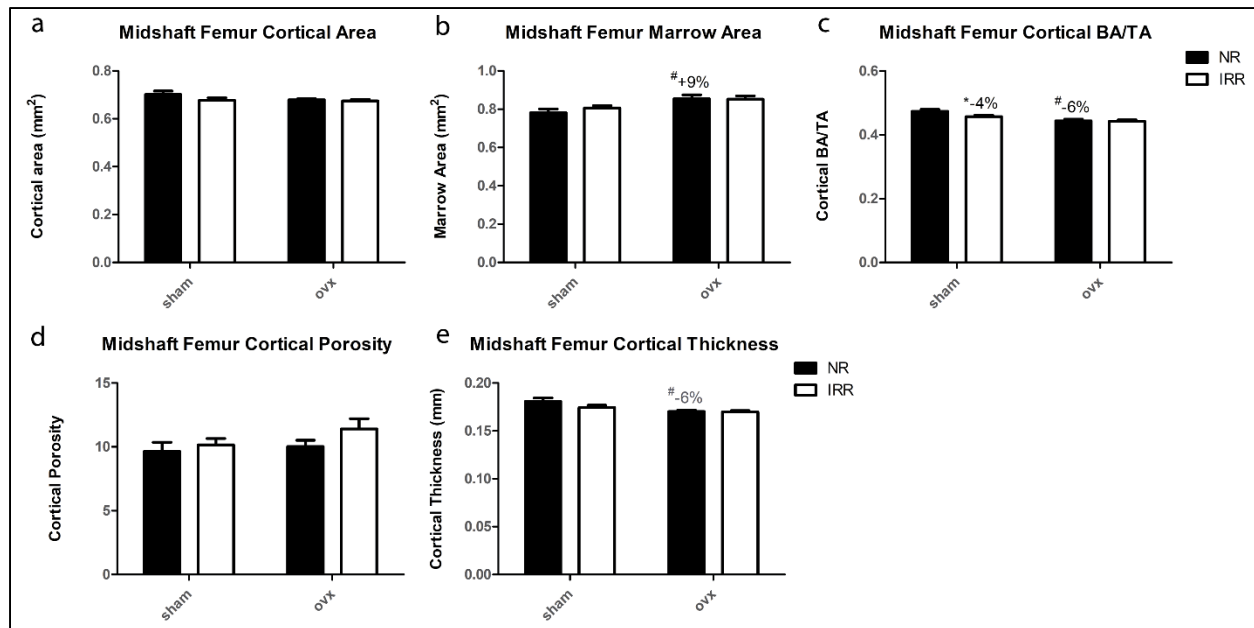


Figure 2.5: Graphs for MicroCT cortical morphometry data for the midshaft femur segment including cortical area (a), marrow area (b), BA/TA (c), cortical porosity (d) and cortical thickness (e). Error bars indicate standard error of the mean. *=significant effect of irradiation within Sham or OVX groups; #=significant effect of OVX within NR or IRR groups ($p<0.05$)

Proximal Femur Finite Element Analysis

Proximal Femur Stiffness

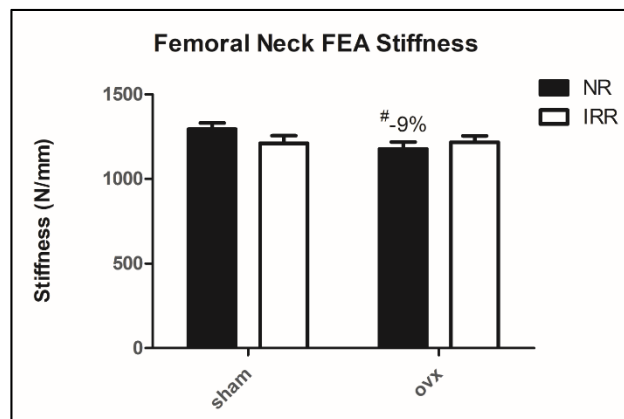


Figure 2.6: Graph for femoral neck stiffness determined using finite element compression simulation. Error bars indicate standard error of the mean. #=significant effect of OVX within NR or IRR groups ($p<0.05$)

At the femoral neck, the only significant change in stiffness was a 9% decline in stiffness in OVX+NR mice compared to Sham+NR mice. A graphical representation of this data is provided in Figure 2.6.

MicroCT L1 Vertebra

Selected morphometry data for the L1 Vertebra can be found in Figure 2.7 (a-c).

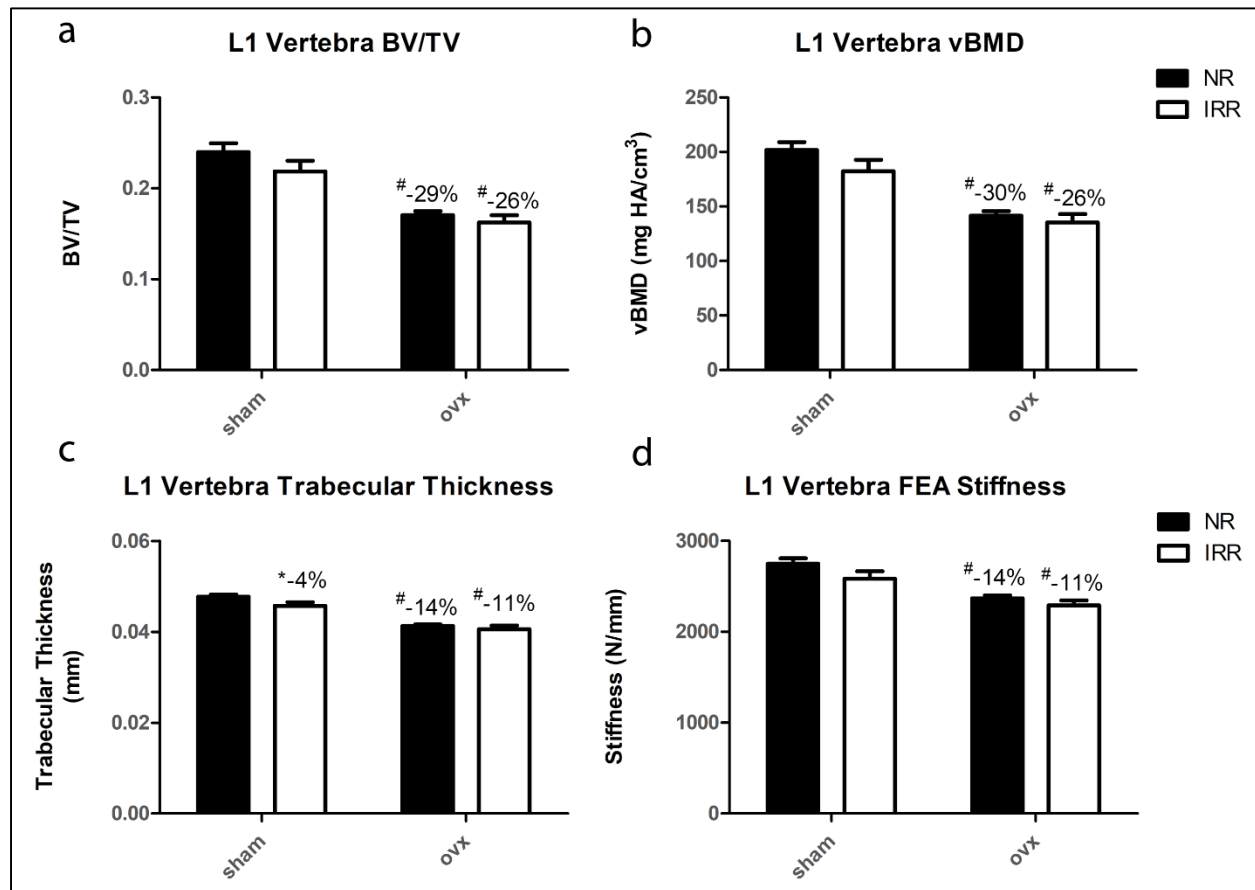


Figure 2.7: Graphs for MicroCT trabecular morphometry data for the L1 vertebra including BV/TV (a), vBMD (b), trabecular thickness (c) and stiffness determined through finite element compression simulation (d). Error bars indicate standard error of the mean. *= significant effect of irradiation within Sham or OVX groups; # = significant effect of OVX within NR or IRR groups (p < 0.05)

L1 Vertebra Trabecular Morphometry

BV/TV declined 29% in OVX+NR mice relative to Sham+NR mice and declined 26% in OVX+IRR mice compared to Sham+IRR mice. Similarly, there was a 30% decrease in vBMD in OVX+NR mice versus Sham+NR mice and a 26% decrease in OVX+IRR mice compared to Sham+IRR mice.

Trabecular thickness in Sham+IRR mice was 4% less than in Sham+NR mice. The OVX+NR group had a 14% decrease in trabecular thickness compared to the Sham+NR group and the OVX+IRR group had an 11% decrease in trabecular thickness relative to the Sham+IRR group.

L1 Vertebra Finite Element Analysis

L1 Vertebra Stiffness

Based on the finite element model, the OVX+NR group stiffness was 14% less than the Sham+NR group and the OVX+IRR group stiffness was 11% less than the Sham+IRR group. These results are also presented as a graph in Figure 2.7 (d).

Discussion

In 2017, gynecological cancers constituted approximately 13% of all new cancer diagnoses for women in the United States [42]. Improved screening guidelines and advances in treatment have led to an increase in the number of survivors who may experience various long-term adverse side effects of radiation therapy. The results from this study characterize the structural and functional changes in bone resulting from fractionated irradiation in a mouse model for treatment of both pre- and post-menopausal women with gynecological tumors. In addition to gynecological cancers, radiation therapy is used to treat many other cancers where bone loss has been similarly reported. There are currently several ongoing clinical trials to look at the efficacy of larger dose fractions of stereotactic body radiotherapy (SBRT) given in a smaller number of fractions to treat oligometastatic cancers, such as breast cancer. Two examples of this treatment protocol use three fractions of 10 Gy X-rays within three weeks to treat breast metastases in the bone [97, 98]. This is becoming a new standard of treatment and the dosing protocol is similar to the one used in our mouse model. The results from this study may be extrapolated to understand bone structural and functional changes resulting from radiation therapy for prostate, anorectal, lung or breast cancers

as well. In 2017, prostate, anorectal, lung and breast cancers accounted for a combined 40% of cancer diagnoses for men and women in the United States [42].

There are two distinct mouse models utilized and compared in this study: fractionated radiation therapy for treatment of gynecological tumors in women and the ovariectomy mouse model for the onset of menopause in women. Both models provide quantitative information on bone mechanisms, structure and function altered through radiation and menopause in women. However, it is important to note that mice lack the Haversian systems for vasculature seen within human bone [99]. Vasculature-related damage may therefore affect mouse and human bone differently. In contrast to humans, the mouse femoral neck has minimal trabecular bone due to the small size. Therefore, the proximal tibia region just distal to the epiphyseal plate is a common skeletal site for microCT analysis in a mouse to quantify changes in trabecular microarchitecture [100]. The ovariectomized mouse model has been shown to closely model changes in cancellous bone seen in postmenopausal women, but not cortical bone [24]. However, the mechanisms involved in estrogen deficiency are consistent with those seen in women, including increased bone resorption. There is also an increase in bone formation (bone surface) that cannot compensate for the increase in resorption, leading to a net imbalance in bone remodeling.

The fractionated radiation protocol used for this study was developed based on the data gathered from the X-ray dose validation preliminary data, BED calculations and anesthesia considerations. In the X-ray dose validation preliminary data, mice that received three fractions of 6 Gy x-rays saw a greater decline in proximal tibia BV/TV than mice that received one single 18 Gy dose. Hong et al. demonstrated that inflammatory genes are rapidly induced (within one to six hours) in the lung following irradiation and that fractionated radiation maintains an up-regulation of cytokine gene expression for a longer period than single dose [66]. These results suggest

differences in tissue response to fractionated vs. single doses of radiation. In response to the cell damage within bone, macrophages are recruited and osteoclast numbers increase. We posit that this additional recruitment of cells to the field of radiation between fractions increases the overall damage to the bone. Therefore, fractionated radiation therapy in the mouse model should more closely mimic clinical treatment in humans.

Ideally, radiation in a mouse study would be given in the same number (~30) of fractions as in women with gynecological tumors. However, the mouse must be anesthetized each time a radiation fraction is given. If more fractions were given, the anesthesia would have too large of an effect in the mice, including loss of body mass, lethargy and lack of eating. Female mice have been shown to experience greater side effects than males, including a higher stress level [101].

With DEXA, there were both whole body and hindlimb declines in aBMD detected from OVX compared to Sham groups. This is not due a loss of body mass, as the OVX mice gained weight throughout the study.

Both ovariectomy and fractionated irradiation in this mouse model caused significant loss of trabecular bone in the proximal tibia. Additionally, the combination of irradiation and ovariectomy had an apparent additive effect in the proximal tibia, with greater trabecular bone loss than either procedure alone. These data suggest that there are different mechanisms being activated in each case. The decrease of estrogen during menopause in women results in an increase in the number and lifespan of osteoclasts, leading to an imbalance in resorption and formation [91, 92, 102]. Ovariectomy models the acute effects of menopause including bone loss driven by stimulated bone marrow macrophages.

With radiation, there is a rapid early increase in osteoclasts, although a depletion of osteoclast progenitor cells, leading to long-term osteoclast decline [63]. Previous studies have

shown increased osteoclast numbers persist for only two weeks [67]. Ionizing radiation causes cell damage in several ways, such as DNA interactions with reactive oxygen species resulting in cell death [59]. The cell death seen in the bone marrow triggers the infiltration and activation of macrophages and neutrophils. Lymphocytes are particularly sensitive to radiation, whereas monocyte-lineage leukocytes are significantly less affected [103]. The suppression of estrogen from ovariectomy in combination with radiation therapy may increase the inflammatory response to radiation through greater infiltration of radiation resistant phagocytes. Bone formation is also impaired following radiation therapy due to a reduction in the number of osteoblasts and osteoblast precursors [59].

Clinical data provides evidence for the decline in trabecular bone density within the radiation field for women with gynecological tumors [104], but cortical bone data is not well-documented in women. Rapid, longitudinal cortical bone loss in the ribs of patients treated with radiosurgical protocols for lung cancer was identified by only 3 months after starting stereotactic body radiation therapy, at all sites absorbing greater than 10 Gy [105]. Moreover, rapid loss of trabecular and cortical bone were observed from the proximal femur was observed from the proximal femur of anal cancer patients within two months of completing intensity modulated radiation therapy [106]. From non-human primate models, a single 10 Gy fraction delivered to the chest of rhesus macaques simulated radiosurgical protocols caused cortical thinning within the exposed vertebrae [107]. In our mouse model, there is an increase in cortical thickness and decrease in cortical porosity seen at the proximal tibia 28 days following the final radiation dose, despite major loss of trabeculae. In a study by Turner et al., C57Bl/6 mice saw an increase in bone formation as a result of activation of bone lining cells within one day of 6 Gy gamma-irradiation [108]. Additionally, there was a strong correlation between marrow cell death resulting from

irradiation and activation of bone lining cells to express osteoblast phenotype, which could offer insight into cortical thickening [108]. Our animal model might provide an understanding of what happens in the cortical bone, although it is important to recognize the absence of a tumor in the model. The 2014 study by Oest et al. provides insight as to the potential mechanism leading to compartmental differences in the bone response [63]. There is an early increase (2 days) of osteoclasts following irradiation, but a long term depletion of osteoclasts. This accounts for a rapid early decrease in trabecular bone, followed by long term matrix deposition without bone turnover. While the thickness of the cortical bone has increased, the bone is likely becoming brittle with time [63].

There is also evidence that adoptive transfer of hematopoietic stem cells (HSCs) and unpurified bone marrow are successful in repopulating bone marrow in irradiated mice, but those cells are unable to prevent trabecular bone loss or reduce the bone loss after two months [109]. We hypothesize that macrophages are rapidly activated following radiation damage in response to the dead and dying marrow cells. Since osteoclasts are closely related to macrophages, they are also activated in a way that causes a rapid and profound bone loss. Osteoclast activation has been demonstrated within three days of irradiation and most bone loss is evident seven to ten days following irradiation [62]. Once trabecular connections are lost, they can no longer transmit mechanical loads that may be necessary for communicating bone repair.

Since radiation rapidly activates osteoclasts, it makes sense to use bisphosphonates early on to prevent the initial activation of osteoclasts. Bisphosphonates are already commonly used clinically to prevent further bone loss resulting from post-menopausal osteoporosis [110]. Risedronate has been tested in a mouse model and demonstrated the ability to mitigate bone loss resulting from 2 Gy x-rays, though not for a dose modeling the BED for fractionated radiation

therapy [67]. One study found a rapid decrease in fecal calcium excretion in both OVX and Sham mice after a zoledronate injection following a 16 Gy single dose of irradiation, suggesting a rapid increase in bone remodeling [111]. Another mouse study showed zoledronate given out to 3 weeks following radiation effectively prevented bone loss, but did not significantly improve bone compressive strength following irradiation [112]. These results suggest the need to further examine material properties altered through concurrent bisphosphonate and radiation treatment. It is also important to consider the side effects of bisphosphonate treatment, including immune suppression. Alendronate and zoledronic acid directly decrease macrophage survival and impair monocyte differentiation into macrophages [113]. Many cancer patients may already be immunosuppressed and therefore, further studies need to be done to assess the risk to the patient.

Loss of bone density and structural stiffness following ovariectomy occurred at all skeletal sites analyzed in this study: tibia, femur and L1 vertebra. Since the L1 vertebra is located outside of the radiation field, there was no significant change in trabecular bone resulting from the radiation treatment. As expected, the suppression of estrogen via ovariectomy had a systemic effect while radiation was largely specific to the X-ray field.

In the proximal tibia, the cortical porosity decreases while cortical thickness increases following radiation. This decrease in porosity could indicate lamellar bone rather than woven bone at one month following the final radiation dose.

In summation, an animal model for women receiving radiation therapy for gynecological tumors was studied. To accomplish this, the standard, well-characterized ovariectomized mouse model was combined with fractionated radiation to the lower limbs. There was a loss of bone structure and function, which is consistent with clinical study results. During the acute phase of bone loss, it makes sense to test bisphosphonate therapies to reduce osteoclast proliferation.

Further studies can be used to expand this model to other cancers, such as prostate cancer. The addition of a tumor to the mouse model prior to radiation therapy could also be employed to further improve the mouse model to be more like the human condition.

CHAPTER 3: EFFECTS OF RADIATION AND HIGH-DOSE ZOLEDRONATE TREATMENT ON THE STRUCTURAL AND MATERIAL PROPERTIES OF BONE IN A MOUSE MODEL

Introduction

From 2016 to 2018, the number of cancer survivors in the United States grew from 15.5 to 16.9 million [114, 115]. This number is expected to continue to increase as treatment options and diagnostic screenings improve [115]. Radiation therapy is commonly used in the oncological setting to kill cancer cells and reduce tumor size. By 2020, the number of cancer survivors who have been treated with radiation is projected to reach 3.38 million [114]. However, this treatment method has damaging side effects including altered bone morphology and increased fracture risk [60, 116]. Several studies have shown that women receiving therapeutic pelvic radiation are more likely to experience a pelvic fracture [3, 83]. The median time from the final radiation dose to fracture is 14.1 months, with 83% of fractures happening within two years of treatment completion [83].

Both bone structure and material properties contribute to overall bone function and fracture risk. In the clinical setting, bone structure is the main parameter for assessing bone health [22]. Imaging modalities, including DEXA and pQCT, allow for visualization of bone structure and quantification of bone morphometric parameters. These techniques also offer the advantage of being minimally invasive and easy to administer [22]. Bone quality and material properties, on the other hand, are more difficult to assess, but just as important in contributing to clinical bone strength [117]. Developments in spectroscopy have allowed for spatial mapping of bone composition using Fourier Transform Infrared Imaging (FTIR) and Raman Spectroscopy.

Generally, studies are performed in animal models so that samples can be embedded or a laser can be focused directly to the bone. In a mouse study, Gong et al. found changes in mineralization resulting from four fractions of 5 Gy x-ray irradiation using Raman to assess mineral to matrix ratio [69]. The study suggests time-dependence of bone quality changes with increase in mineralization seen at 4 weeks, but decreased mineralization at 12 weeks following irradiation [69]. A complete analysis and timeline for changes in bone material quality resulting from radiation and bisphosphonate treatment can provide information on overall changes in bone function.

During treatment of cervical cancer, the total radiation dose targeted at the tumor can be up to 55 Gy given in smaller daily fractions for several weeks [82]. In mice, a single dose of 2 Gy X-rays causes a 32% decrease in trabecular bone density at the proximal tibia after just one week [67]. Willey et al. demonstrated an early increase in osteoclast number evident at three days following a single 2 Gy X-ray exposure [62]. This initial increase is followed by a long-term depletion of osteoclasts [63]. Oest et al. showed that elevated levels of osteoclasts persist for approximately two weeks following either a single 5 Gy X-ray dose or four fractions of 5 Gy X-ray dose and then drop in number significantly [63]. Since trabecular bone resorption correlates temporally with elevated osteoclast levels, bisphosphonates could be used in the short term to prevent trabecular bone loss during radiation therapy.

Bisphosphonates are a class of drugs that inhibit osteoclasts in order to prevent bone loss [118]. Compared to the other bisphosphonates, zoledronate has the highest potency and affinity for bone and is commonly used for other reasons in the oncological setting [119, 120]. Since bisphosphonates are already FDA-approved and in use for osteoporosis treatment, the

demonstration of their efficacy in mitigating radiation-induced bone loss can have a rapid clinical impact.

Currently, risedronate and zoledronate have been tested within different mouse models for radiation therapy. In a risedronate study, mice received 2 Gy x-rays to their whole body and treated with 30 $\mu\text{g/kg}$ every other day for one, two or three weeks [67]. Risedronate prevented trabecular bone loss and reduced osteoclast number following radiation therapy [67]. In another study, mice received a single hindlimb exposure of 20 Gy and were given 100 $\mu\text{g/kg}$ zoledronate injections four days prior to irradiation and once a week for up to three weeks following radiation treatment depending on the group time point [112]. Zoledronate improved bone morphology in irradiated mice, but did not increase compressive strength through mechanical testing [112]. While the therapeutic potential of bisphosphonates during radiation therapy has been shown, there is limited data for use with radiation fractionation, long-term bone morphology and characterization of material properties.

The goal of this study is to characterize the short and long term effects of zoledronate and concurrent fractionated radiation on bone morphology, compressive stiffness, composition and elastic modulus. We hypothesize that zoledronate will improve bone morphology, increase mineralization and overall compressive stiffness of bone following irradiation. In order to assess the therapeutic efficacy of zoledronate for radiation therapy, micro-computed tomography (microCT), finite element analysis (FEA), Fourier Transform Infrared Spectroscopy (FTIR), Raman spectroscopy and nanoindentation will be employed. The results from the study can be used to inform clinical assessment of bisphosphonates for use during cancer treatment.

Methods

Animals and Study Design

One hundred and twenty female C57BL/6 mice were purchased from Charles River (Charles River Laboratories, Morrisville, NC). All mice were 14 weeks of age at the start of the study with food and water available ad libitum throughout the study. All investigations were approved by the University of North Carolina, Chapel Hill Institutional Animal Care and Use Committee.

The mice were divided into 3 groups of 40 mice per group based on time points for sacrifice: 3 days, 14 days and 6 months. Within each group, half of the mice were irradiated (IRR) and half were not (NR). The IRR mice received three fractions of 6 Gy X-rays per fraction to the hindlimbs given on days 0, 2 and 4 (18 Gy total). Within NR and IRR mice, half of the mice received a 50 µg/kg injection of zoledronate (ZOL) every other day for two weeks starting Day 0, while the other half received placebo (PLAC) saline injections (n=10). For all mice, a calcein fluorescent label (10 mg/kg) was injected subcutaneously on Day 0 prior to irradiation. A tetracycline fluorescent label (20 mg/kg) was given two days prior to sacrifice. Following dissections, the left hindlimb was wrapped in PBS soaked gauze and frozen at -20C and the right hindlimb was stored in 70% ethanol. All mice were weighed at the start of the study and at dissection.

Microcomputed Tomography

MicroCT scans of the right tibia were taken at 10-micron isotropic voxel size (µCT80; Scanco Medical AG, Brüttisellen, Switzerland). The scans were acquired using a 70-kVp peak X-ray tube potential, a 0.5-mm Al filter and an integration time of 800 ms to reduce beam-hardening effects and improve the signal-to-noise ratio. Scanco software was used to analyze and

quantify bone microarchitectural parameters from contoured regions. All contouring was performed semi-automatically to separate trabecular and cortical compartments. For the proximal tibia, a 1 mm section of the metaphysis just below the growth plate was chosen as the contour region. Structural parameters including bone volume fraction (BV/TV), connectivity density (Conn.D), trabecular number (Tb.N), trabecular thickness (Tb.Th), trabecular separation (Tb.Sp), structure model index (SMI), volumetric bone mineral density (vBMD), cortical porosity, cortical area, marrow area and total area were quantified.

Finite Element Analysis

The same 1-mm region of each proximal tibia used for microCT analysis was exported from the scanner and imported as a tetrahedral mesh into Abaqus software (Abaqus/CAE 6.9-EF1, Dassault Systems Simulia Corp, Providence, RI) for finite element analysis. For each individual bone section, homogenous material properties were applied to the tibia by assigning a Young's Modulus of 10 GPa and Poisson's Ratio of 0.3. Then, two node sets were created: one containing all nodes on the proximal end of the tibia segment and the other comprised of all distal nodes of the tibia segment. For the loading step, boundary conditions were applied to secure the distal end of the tibia while displacing the proximal end 5 μm ($\sim 0.5\%$ strain) downward in the z-direction. The resultant force was measured and used to calculate compressive stiffness (force/displacement).

Statistical Analysis

Significance was determined using SigmaPlot 12.0 (Systat Software Inc., San Jose, CA). The threshold for significance for all tests was set at a 5% probability of a type I error ($p = 0.05$). All statistical comparisons for MicroCT and Finite Element Analysis data were made using a two-way ANOVA within each time point (3 day, 14 day and 6 month). A Tukey post hoc test

was run to explore potential interactions and to maintain a Type 1 error of 0.05 across multiple comparisons (NR, IRR, ZOL and PLAC).

Nanoindentation

In order to characterize changes to the average elastic modulus of bone resulting from radiation and zoledronate, nanoindentation was performed on tibiae from the 14 day and 6 month time points. Each tibia was embedded in Clarocit resin and then sectioned using a low-speed diamond saw approximately 2 mm from the proximal end (about 0.5 mm from the distal border of the growth plate). The end of the tibia distal to the cut was ground using wet silicon carbide paper (600, 800, 1200 and 2400 grit) and then polished using 0.1 micron aluminum oxide paste and rayon cloth. The same region was used for testing in each bone (Figure 3.1) with the area for the indentation array shown in red rectangle. Starting from the endosteal surface, six rows of four indents were made with a maximum load of 5 mN/indent. Between all neighboring indents in an array, there was a separation distance of 20 microns. A Berkovich tip and a ramp and hold profile with a one minute hold at the maximum load was used for every indent. Twenty four tibiae total were tested, with n=3 per treatment group.

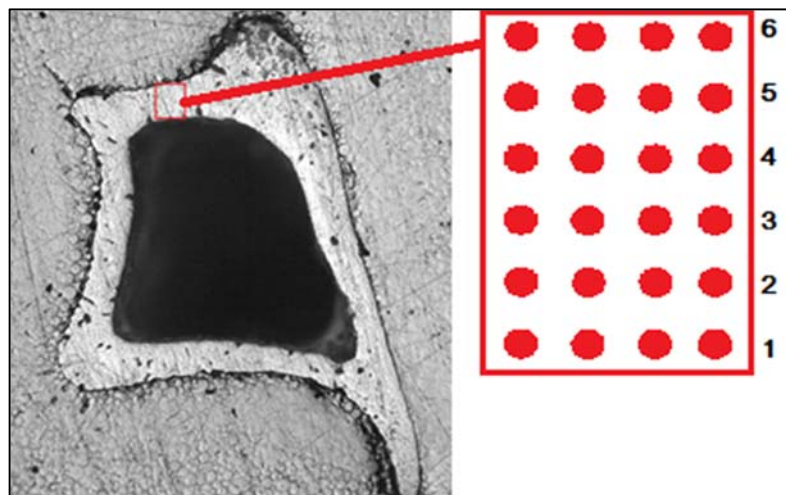


Figure 3.1: Optical microscope proximal tibia image with region for nanoindentation array in a red rectangle. Six rows of four indents per row were performed starting close to the endosteal surface and ending close to the periosteal surface

Upon testing completion, the force-displacement curves were analyzed to determine whether the tip used for indenting had hit a pore in the bone and should be eliminated from the data set (outlier). From the remaining curves, the Hysitron software was used to calculate the reduced modulus based on the Oliver-Pharr method [7]. Histograms for all reduced modulus data were created to look for skew. In order to determine statistical significance, two different approaches were used. First, a Two-Way ANOVA was run within each time point (14 day and 6 month) to compare average reduced modulus between groups (NR-PLAC, NR-ZOL, IRR-PLAC, IRR-ZOL) using SigmaPlot 12.0 (Systat Software Inc., San Jose, CA). Specifically, an average reduced modulus value from all 24 indents within each bone was calculated and used as one data point within a test group (i.e. NR-PLAC) resulting in $n=3$ per test group. The threshold for significance for all tests was set at a 5% probability of a type I error ($p = 0.05$). A Tukey post hoc test was run to explore potential interactions and to maintain a Type 1 error of 0.05 across multiple comparisons (NR, IRR, ZOL and PLAC).

In order to look for changes from endosteal to periosteal surface of the cortical thickness, a mixed model approach was used for the 14 day and 6 month time points with JMP Software from SAS (SAS Institute, Cary, NC). Tibia sample number was added as a random effect, nested within radiation and zoledronate. The fixed effects were radiation group, zoledronate group and percentage of cortical thickness from endosteal surface. A full factorial of the three fixed effects was used to look both at independent effects and interaction effects. The reduced modulus was chosen for the outcome or dependent variable. The threshold for significance for all tests was set at a 5% probability of a type I error ($p = 0.05$).

Fourier Transform Infrared Spectroscopy Imaging

In order to investigate bone composition, the proximal tibiae were evaluated using FTIR imaging. The embedded tibiae used for nanoindentation were cut down to 4 mm thickness by removing material from the distal tibia end and leaving the proximal surface intact. Spectral images were collected using the Perkin Elmer Spotlight FT-IR Imaging system (Perkin Elmer, Seer Green, UK) at a spectral resolution of 4 cm^{-1} and spatial resolution of 1.56 microns in Attenuated Total Reflection Imaging mode. Background and Clarocit resin spectra were also collected for each sample to allow for correction. A 50 by 500 micron region was imaged for each tibia as shown in Figure 3.2 to ensure a full cross-section of the cortical bone was captured.

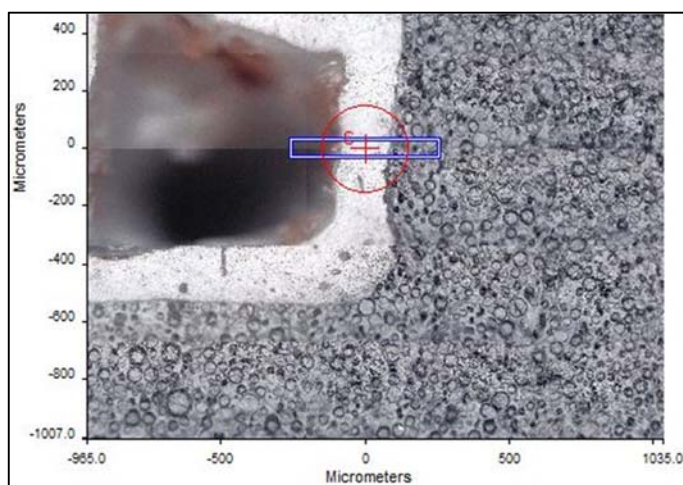


Figure 3.2: Example image of proximal tibia set up for FTIR imaging. The blue rectangle represents the area for FTIR assessment.

Using Spectrum Image Software, all spectra were atmosphere corrected, baseline corrected and Clarocit contributions were subtracted. Images of three tibiae for each treatment group (NR-PLAC, NR-ZOL, IRR-PLAC, IRR-ZOL) within the 14 day and 6 month time points were taken and evaluated. Each pixel in an image represents the absorbance spectra of infrared light at that location in the bone. Based on this spectra, significant ratios relating to bone quality and composition can be calculated [121]. Mineral to matrix ratio was calculated by taking the

integrated area of the phosphate band ($900\text{-}1200\text{ cm}^{-1}$) and dividing by the amide I band ($1585\text{-}1725\text{ cm}^{-1}$). Carbonate to phosphate ratio was calculated as the integrated area of the carbonate band ($850\text{-}900\text{ cm}^{-1}$) divided by the phosphate band ($900\text{-}1200\text{ cm}^{-1}$). Crystallinity, which is a measure of crystal size/strain and maturation, is determined by taking the 1030 cm^{-1} absorbance peak divided by the 1020 cm^{-1} peak [121]. Average ratios were calculated for each bone and used as one data point for $n=3$ per group. A Two-Way ANOVA was run within each time point (14 day and 6 month) to compare average reduced modulus between groups (NR-PLAC, NR-ZOL, IRR-PLAC, IRR-ZOL). The threshold for significance for all tests was set at a 5% probability of a type I error ($p = 0.05$). A Tukey post hoc test was run to explore potential interactions and to maintain a Type 1 error of 0.05 across multiple comparisons (NR, IRR, ZOL and PLAC).

Raman Spectroscopy

Raman spectroscopy mapping of the proximal tibia was performed in order to evaluate bone composition from endosteal to periosteal surface. A Renishaw inVia confocal microscopy system (Renishaw, Wotton-under-Edge, Gloucestershire, UK) using 785 nm wavelength laser light routed through fiberoptic cables to a $50\times$ objective (NA 0.75) and mounted on a nanoindenter z-stage (TI 950, Hysitron, Minneapolis, MN) was used [122]. The laser power was set to 100 and 6 accumulations of 10 seconds exposure were collected from each location in the

array. Spectra were taken in three rows spaced 15 microns between each acquisition in either direction and extending the full thickness of the cortical bone (Figure 3.3).

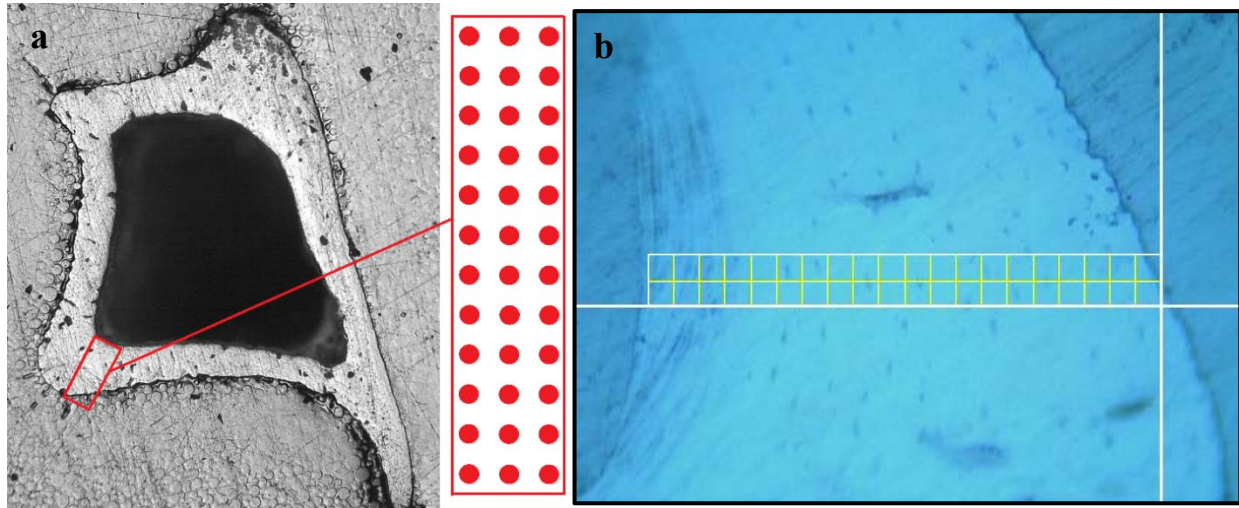


Figure 3.3: (a) Proximal tibia cross section with area for Raman array in a red rectangle. Three indents per row were spaced 15 microns apart from periosteal to endosteal surface. (b) Example setup of array to gather spectral data across the cortical thickness

The baseline was subtracted and cosmic rays were removed using the Renishaw WIRE software. Custom MATLAB code developed in Dr. Virginia Ferguson's lab by Dr. Chelsea Heveran was used to subtract a reference PMMA spectrum from each point and calculate all ratios. Mineral to matrix ratio was calculated by taking the area of the phosphate (961 cm^{-1}) peak divided by the area of the proline peak (855 cm^{-1}). Carbonate to phosphate ratios were evaluated by taking the area ratios of carbonate (1071 cm^{-1}) to phosphate (961 cm^{-1}). Lastly, crystallinity was determined by taking the inverse of the half-width at the full maximum height of the ν_1 phosphate peak. In order to determine statistical significance, two different approaches were used. First, a Two-Way ANOVA was run within each time point (14 day and 6 month) to compare average parameter values (mineral to matrix ratio, carbonate to phosphate ratio, crystallinity) between groups (NR-PLAC, NR-ZOL, IRR-PLAC, IRR-ZOL). Specifically, an average parameter value from all three rows of spectra taken across the cortical thickness within each bone was calculated

and used as one data point within a test group (i.e. NR-PLAC) resulting in n=5 per test group at the 6 month time point and n=3 at the 14 day time point.

A mixed methods approach was used to look for changes from endosteal to periosteal surface of the cortical thickness with JMP software from SAS. Tibia sample number was added as a random effect, nested within radiation and zoledronate. The fixed effects were radiation group, zoledronate group and percentage of cortical thickness from endosteal surface. A full factorial of the three fixed effects was used to look both at independent effects and interaction effects. The mineral to matrix ratio, carbonate to phosphate ratio and crystallinity were assigned dependent variables. The threshold for significance for all tests was set at a 5% probability of a type I error ($p = 0.05$).

Results

Body Mass (Table 3.1)

At the start of the study (Day 0), there were no statistically significant differences in body mass between study groups. At the 3 day time point and 14 day time point, there were no differences in body mass between study groups as well. For the 6 month time point, there was a 17% increase in body mass in the IRR-ZOL group compared to the NR-ZOL group.

	NR-PLAC	NR-ZOL	IRR-PLAC	IRR-ZOL
3 day initial body mass	21.4 ± 1.1	21.5 ± 1.2	21.5 ± 0.7	21.4 ± 1.2
3 day final body mass	21.8 ± 1.2	22.3 ± 1.4	21.7 ± 0.5	21.6 ± 1.1
3 day average change in body mass	0.39 ± 0.64	0.84 ± 0.49	0.18 ± 0.79	0.15 ± 0.50
14 day initial body mass	21.4 ± 1.3	21.4 ± 1.0	21.3 ± 1.3	21.6 ± 1.4
14 day final body mass	22.0 ± 1.1	22.5 ± 1.2	21.9 ± 1.6	22.3 ± 1.3
14 day average change in body mass	0.62 ± 0.76	1.11 ± 0.60	0.54 ± 1.01	0.72 ± 0.67
6 month initial body mass	22.0 ± 1.1	21.2 ± 1.0	21.6 ± 0.9	21.5 ± 0.8
6 month final body mass	28.7 ± 3.6	29.9 ± 3.6	32.0 ± 5.2	34.9 ± 5.2*
6 month average change in body mass	11.1 ± 7.8	8.7 ± 3.1	10.5 ± 4.5	13.5 ± 5.0*

Table 3.1: Initial body mass, final body mass and average change in body mass for each treatment group and time point. *=statistically significant effect of irradiation (p<0.05)

Proximal Tibia MicroCT

All microCT proximal tibia data can be found in Table 3.2. Example microCT images of a 6 month NR-ZOL proximal tibia can be found in Figure 3.4. Graphs for proximal tibia bone volume fraction at each time can be found in Figure 3.5 below.

3 Day Time Point

There were no significant changes in bone volume fraction (BV/TV), volumetric bone mineral density (vBMD) or connectivity density at Day 3. Trabecular number increased 10% from NR-PLAC to NR-ZOL. Trabecular thickness declined 9% from NR-PLAC to NR-ZOL and increased 12% from NR-ZOL to IRR-ZOL. There was a 10% decrease in trabecular spacing from NR-PLAC to NR-ZOL.

14 Day Time Point

Overall, radiation damaged trabecular architecture and zoledronate improved trabecular morphometric parameters. Bone volume fraction (BV/TV) decreased 31% from NR-PLAC to IRR-PLAC, but increased 38% from NR-PLAC to NR-ZOL and increased 117% from IRR-PLAC to IRR-ZOL. Similarly, vBMD decreased 43% from NR-PLAC to IRR-PLAC, but increased 33% from NR-PLAC to NR-ZOL and increased 120% from IRR-PLAC to IRR-ZOL. Connectivity density decreased 61% from NR-PLAC to IRR-PLAC. There was an increase in connectivity density from NR-PLAC to NR-ZOL (+41%) and from IRR-PLAC to IRR-ZOL (+222%). Trabecular number decreased 21% from NR-PLAC to IRR-PLAC, increased 20% from NR-PLAC to NR-ZOL and increased 40% from IRR-PLAC to IRR-ZOL. There was a 10% increase in trabecular thickness from IRR-PLAC to IRR-ZOL and an 11% increase in trabecular thickness from NR-ZOL to IRR-ZOL. Trabecular spacing increased 30% from NR-PLAC to IRR-PLAC, but decreased 17% from NR-PLAC to NR-ZOL and decreased 30% from IRR-PLAC to IRR-ZOL.

6 Month Time Point

There was a 1292% increase in BV/TV from NR-PLAC to NR-ZOL and an 1139% increase from IRR-PLAC to IRR-ZOL, with no changes resulting from irradiation after six months. The high-dose zoledronate treatment had similarly dramatic effects on other trabecular microarchitecture parameters after 6 months, including large increases in vBMD, trabecular number and thickness. Figure 3.4 shows an example NR-ZOL image for the 6 month time point, in which the trabecular compartment is almost entirely solidified.

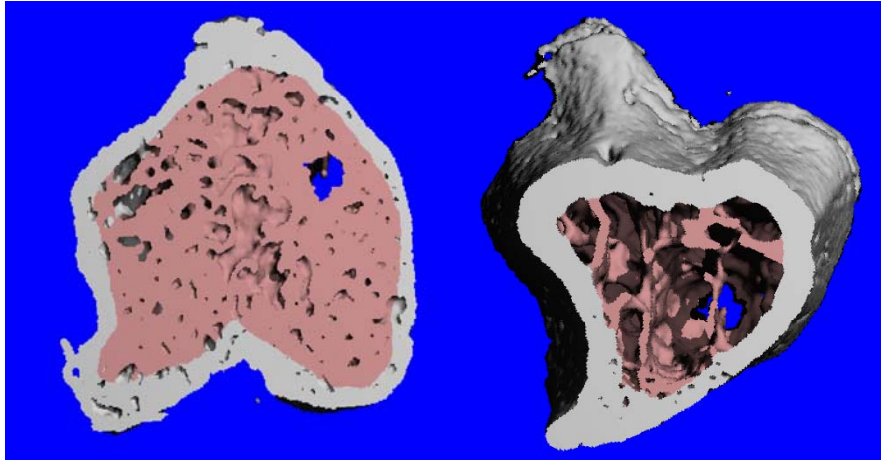


Figure 3.4: MicroCT example images of NR-ZOL bone at 6 month time point. The trabecular compartment (show in pink) is almost entirely filled in with bone.

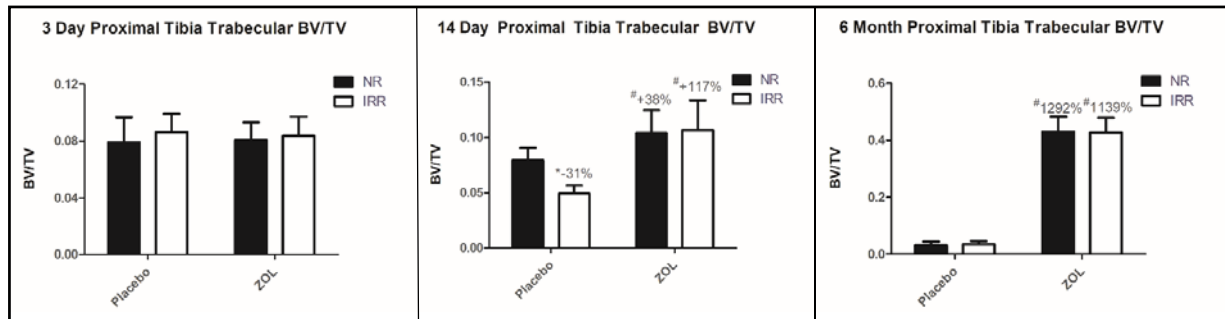


Figure 3.5: Proximal tibia trabecular bone volume fraction at 3 day, 14 day and 6 month time points. *=significant effect of irradiation with PLAC or ZOL groups, #=significant effect of ZOL within NR or IRR groups ($p < 0.05$)

MicroCT Analysis		NR-PLAC	NR-ZOL	IRR-PLAC	IRR-ZOL
3 Day Proximal Tibia Trabecular Analysis	BV/TV	0.079 ± 0.018	0.081 ± 0.012	0.086 ± 0.013	0.084 ± 0.014
	vBMD (mgHA/cm³)	88.2 ± 15.3	86.3 ± 11.9	91.1 ± 10.6	87.4 ± 14.4
	Conn. Dens. (mm⁻³)	41.0 ± 14.0	50.4 ± 20.2	40.1 ± 13.9	45.3 ± 17.6
	Trab. Number (1/mm)	3.06 ± 0.27	3.36 ± 0.37 [#]	3.20 ± 0.38	3.31 ± 0.22
	Trab. Thickness (mm)	0.050 ± 0.004	0.046 ± 0.003 [#]	0.052 ± 0.006	0.051 ± 0.005 [*]
	Trab. Spacing (mm)	0.33 ± 0.03	0.30 ± 0.03 [#]	0.31 ± 0.04	0.30 ± 0.02
14 Day Proximal Tibia Trabecular Analysis	BV/TV	0.079 ± 0.011	0.103 ± 0.021 [#]	0.049 ± 0.007 [*]	0.107 ± 0.027 [#]
	vBMD (mgHA/cm³)	88.4 ± 10.6	117.6 ± 20.1 [#]	50.6 ± 8.4 [*]	111.4 ± 25.4 [#]
	Conn. Dens. (mm⁻³)	43.1 ± 13.1	60.6 ± 20.8 [#]	16.7 ± 7.7 [*]	53.7 ± 16.3 [#]
	Trab. Number (1/mm)	3.04 ± 0.28	3.64 ± 0.43 [#]	2.41 ± 0.42 [*]	3.34 ± 0.34 [#]
	Trab. Thickness (mm)	0.050 ± 0.004	0.049 ± 0.002	0.050 ± 0.005	0.055 ± 0.004 ^{*#}
	Trab. Spacing (mm)	0.332 ± 0.031	0.274 ± 0.040 [#]	0.430 ± 0.067 [*]	0.299 ± 0.033 [#]
6 Month Proximal Tibia Trabecular Analysis	BV/TV	0.031 ± 0.013	0.429 ± 0.052 [#]	0.034 ± 0.011	0.427 ± 0.051 [#]
	vBMD (mgHA/cm³)	36.2 ± 7.3	412.0 ± 47.4 [#]	35.5 ± 14.8	424.2 ± 49.4 [#]
	Conn. Dens. (mm⁻³)	7.9 ± 14.3	121.3 ± 21.1 [#]	6.3 ± 7.4	102.2 ± 36.1 [#]
	Trab. Number (1/mm)	1.83 ± 0.25	5.20 ± 0.43 [#]	1.96 ± 0.32	4.77 ± 0.50 ^{*#}
	Trab. Thickness (mm)	0.058 ± 0.007	0.081 ± 0.005 [#]	0.070 ± 0.007 [*]	0.084 ± 0.010 [#]
	Trab. Spacing (mm)	0.566 ± 0.071	0.223 ± 0.021 [#]	0.529 ± 0.107	0.227 ± 0.030 [#]

Table 3.2: Mean and standard deviation for 3 day, 14 day and 6 month proximal tibia trabecular analysis. *=significant effect of irradiation with PLAC or ZOL groups, #=significant effect of ZOL within NR or IRR groups (p<0.05)

Proximal Tibia Finite Element Analysis

At three days, there were no changes in stiffness in the whole proximal tibia segment or isolated trabecular compartment. However, there was an 11% increase in stiffness in the isolated cortical bone from NR-PLAC to IRR-PLAC.

In the 14 Day groups, zoledronate increased whole bone stiffness in both NR mice (+15%) and IRR mice (+17%). There was also a 9% increase in whole bone stiffness from NR-ZOL to IRR-ZOL. In the isolated trabecular compartment, there was an increase in stiffness resulting from zoledronate in both NR (+18%) and IRR (+74%) mice. Trabecular stiffness declined 37% from NR-PLAC to IRR-PLAC. Cortical stiffness, however, increased 19% from NR-PLAC to IRR-PLAC and increased due to zoledronate within both NR (+14%) and IRR (+14%) mice.

At 6 months, zoledronate increased whole bone stiffness within NR (+90%) and IRR (+116%) mice. Most of this increase in stiffness came from the trabecular compartment, with a 108% and 867% increase in isolated trabecular bone stiffness from zoledronate within NR mice and IRR mice, respectively. Cortical stiffness also increased with zoledronate treatment in both NR (+23%) and IRR (+26%). There were no changes between NR and IRR mice in whole bone, trabecular bone or cortical bone stiffness. Graphs for proximal tibia FEA stiffness can be found in Figure 3.6.

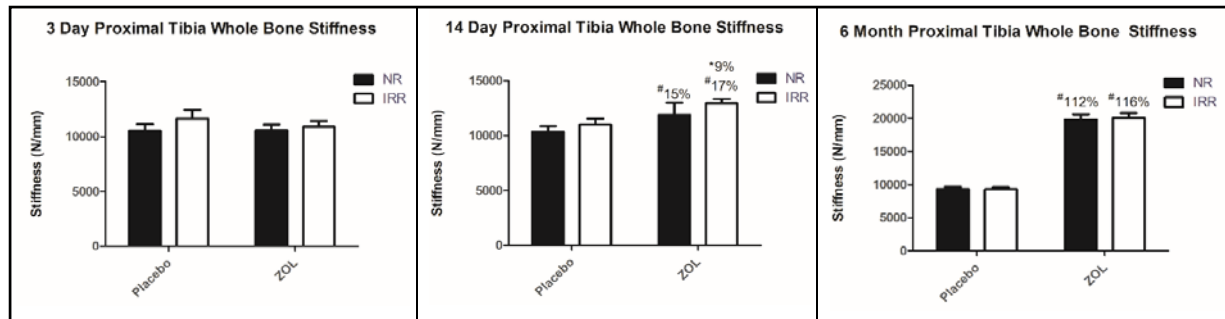


Figure 3.6: FEA proximal tibia stiffness comparison for treatment groups at 3 day, 14 day and 6 month time points. *=significant effect of irradiation with PLAC or ZOL groups, #=significant effect of ZOL within NR or IRR groups ($p < 0.05$)

Nanoindentation

Two-way ANOVA

Based on the two-way ANOVA using single value modulus averages for each bone, there were no significant changes in reduced modulus between any groups in the study (NR-PLAC, NR-ZOL, IRR-PLAC, IRR-ZOL) resulting from radiation or zoledronate treatment at the 14 day or 6 month time points (Figure 3.7).

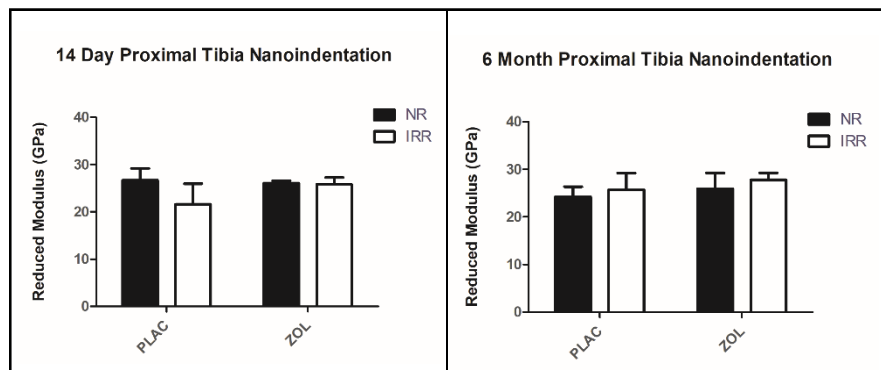


Figure 3.7: Mean and standard deviation bar graphs of nanoindentation data for 14 days and 6 month time points by using average modulus for each bone as single data point ($n=3$).

Mixed Effects Model

6 Month Analysis

The mixed effects model including all indents across the cortical thickness of each bone revealed modulus changes within the bone from endosteal to periosteal surface. There was a

significant effect ($p=0.0001$) of percentage of cortical thickness from endosteal surface within both 6 month and 14 day time points (Table 3.3 and 3.4). The effects of radiation and zoledronate from endosteal to periosteal surfaces within 6 month and 14 day time points are shown below in Figure 3.8 and 3.9.

Fixed Effect Tests					
Source	Nparm	DF	DFDen	F Ratio	Prob > F
RAD	1	1	11.01	1.2209	0.2928
ZOL	1	1	11.01	2.6430	0.1323
RAD*ZOL	1	1	11.01	0.3179	0.5842
Percentage of Cortical Thickness From Endosteal Surface	5	5	310.3	10.6077	<.0001*
RAD*Percentage of Cortical Thickness From Endosteal Surface	5	5	310.3	1.8468	0.1035
ZOL*Percentage of Cortical Thickness From Endosteal Surface	5	5	310.3	0.8213	0.5352
RAD*ZOL*Percentage of Cortical Thickness From Endosteal Surface	5	5	310.3	1.4722	0.1986

Table 3.3: 6 month nanoindentation fixed effect results from full-factorial mixed model analysis and significance ($p<0.05$) shown by p-value in Prob>F column on the far right.

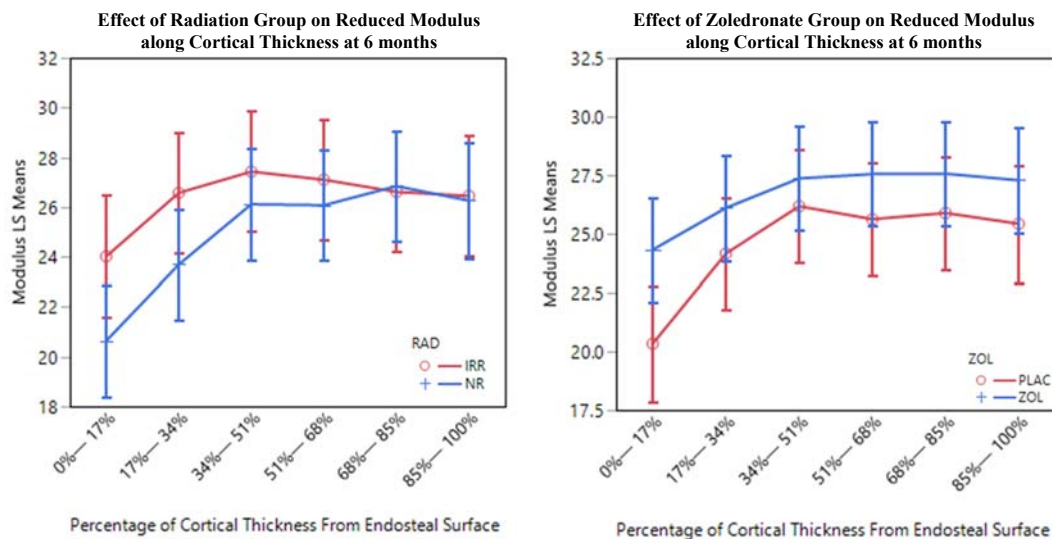


Figure 3.8: Reduced modulus least square means for 6 month time point along cortical thickness from endosteal to periosteal surface from the mixed model analysis. Left graph compares irradiated mice (red) to non-irradiated mice (blue) and right graph compared zoledronate treated mice (blue) with placebo treated mice (red).

14 Day Analysis

Source	Nparm	DF	DFDen	F Ratio	Prob > F
RAD	1	1	9.829	2.2398	0.1659
ZOL	1	1	9.829	2.3849	0.1541
RAD*ZOL	1	1	9.829	2.4423	0.1497
Percentage of Cortical Thickness from Endosteal Surface	5	5	277.2	2.4113	0.0367*
RAD*Percentage of Cortical Thickness from Endosteal Surface	5	5	277.2	1.3015	0.2634
ZOL*Percentage of Cortical Thickness from Endosteal Surface	5	5	277.2	0.4446	0.8171
RAD*ZOL*Percentage of Cortical Thickness from Endosteal Surface	5	5	277.2	0.6035	0.6973

Table 3.4: 14 day nanoindentation fixed effect results from full-factorial mixed model analysis and significance ($p < 0.05$) shown by p-value in Prob>F column on the far right.

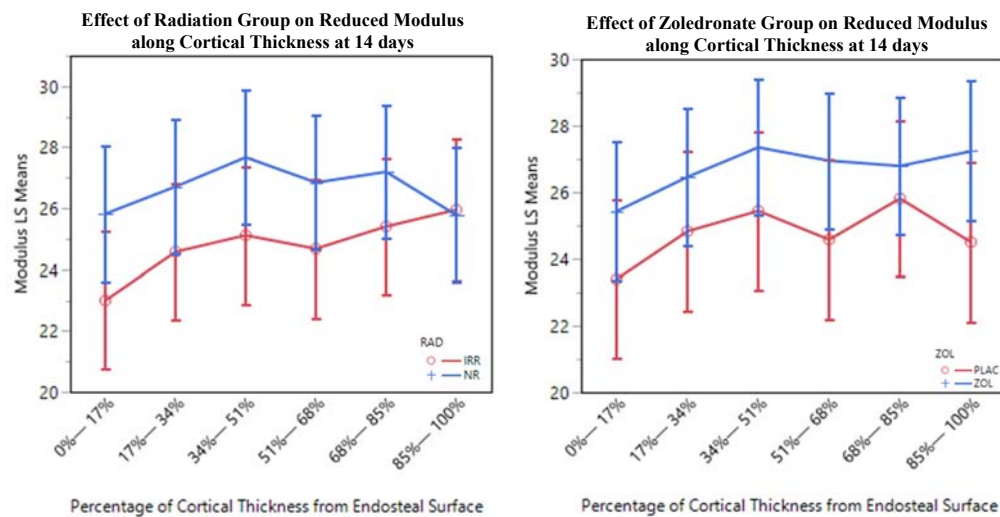


Figure 3.9: Reduced modulus least square means for 14 day time point along cortical thickness from endosteal to periosteal surface using the mixed model analysis. Left graph compares irradiated mice (red) to non-irradiated mice (blue) and right graph compared zoledronate treated mice (blue) with placebo treated mice (red).

Fourier Transform Infrared Spectroscopy

There were no significant differences between groups (NR-PLAC, NR-ZOL, IRR-PLAC, IRR-ZOL) within the 14 day or 6 month time point for mineral to matrix ratio, carbonate to phosphate ratio or crystallinity. The data for mineral to matrix ratio, carbonate to phosphate ratio and crystallinity for the 14 day and 6 month time points are displayed in graphs found in Figure 3.10.

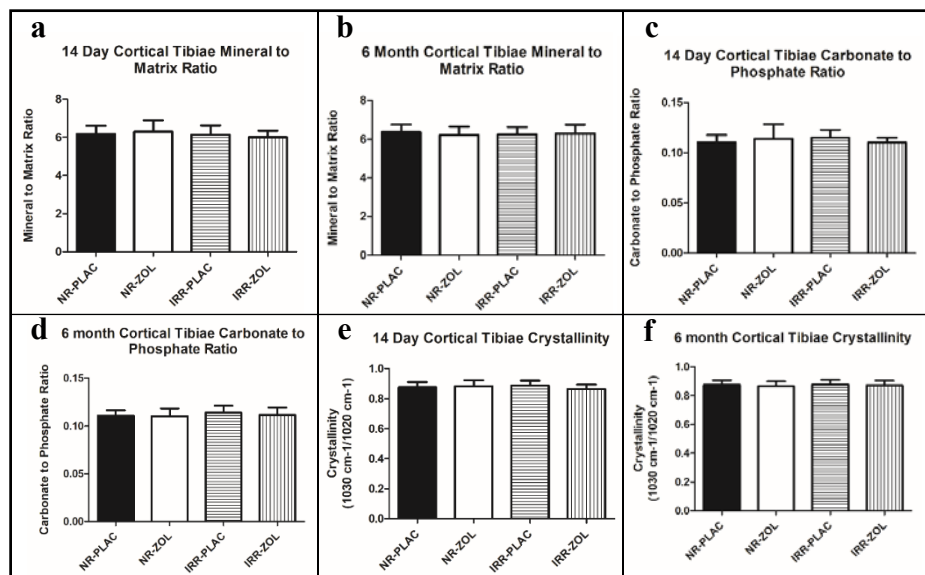


Figure 3.10: FTIR graphs for relevant bone material ratios at the cortical tibia. (a) 14 day mineral to matrix ratio (b) 6 month mineral to matrix ratio (c) 14 day carbonate to phosphate ratio (d) 6 month carbonate to phosphate ratio (e) 14 day crystallinity (f) 6 month crystallinity

Raman Spectroscopy

Two-Way ANOVA

Based on the two-way ANOVA using single value parameter averages for each bone, there were no significant changes in mineral to matrix ratio, carbonate to phosphate ratio or crystallinity between any groups in the study (NR-PLAC, NR-ZOL, IRR-PLAC, IRR-ZOL) resulting from radiation or zoledronate treatment at the 14 day or 6 month time points (Figure 3.11). Example mineral to matrix heat maps for each bone can be found below in Figure 3.12.

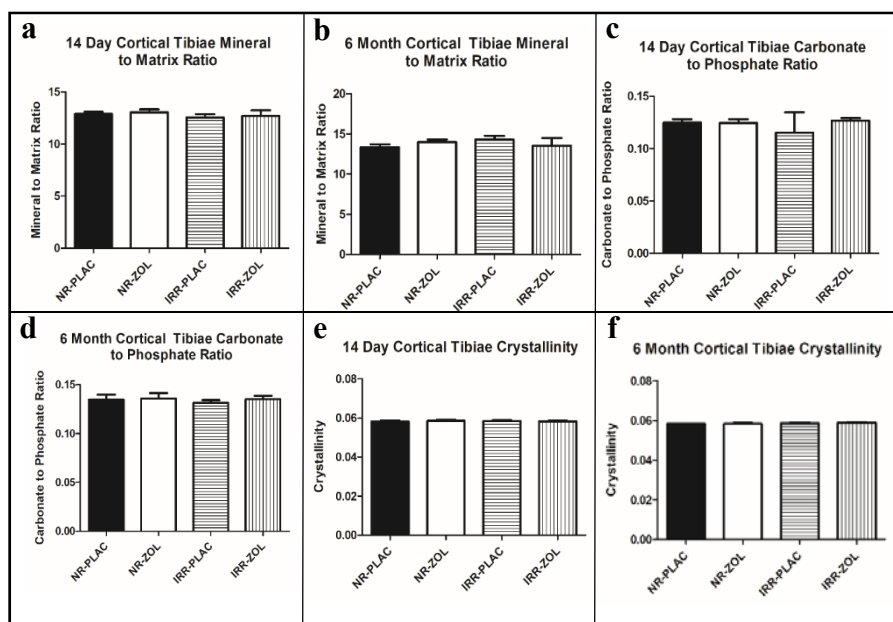


Figure 3.11: Raman spectroscopy graphs for relevant bone material ratios at the cortical tibia using a single average value per bone sample within a treatment group. (a) 14 day mineral to matrix ratio (b) 6 month mineral to matrix ratio (c) 14 day carbonate to phosphate ratio (d) 6 month carbonate to phosphate ratio (e) 14 day crystallinity (f) 6 month crystallinity

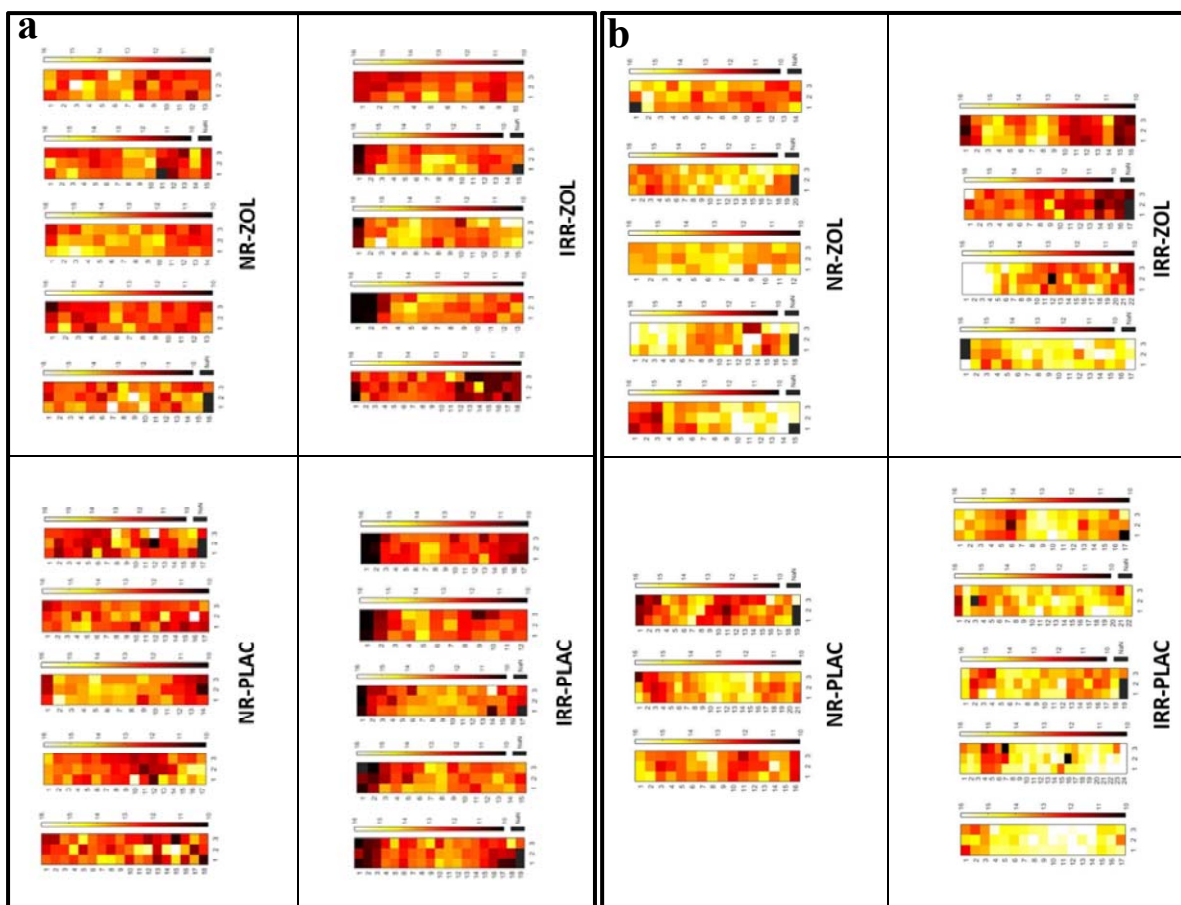


Figure 3.12: Heat maps for Raman Mineral to Matrix Ratio from each bone (white/yellow=high mineral to matrix ratio, red/black=low mineral to matrix ratio).
(a) 14 day time point heat maps (b) 6 month time point heat maps

Mixed Model Statistical Analysis

6 month analysis

Mineral to Matrix Ratio at 6 month time point (Figure 3.13): There was a significant effect of percentage of cortical thickness from endosteal surface for mineral to matrix ratio (Table 3.6). There was also a significant interaction ($p=0.0095$) between radiation and percentage of cortical thickness.

Fixed Effect Tests					
Source	Nparm	DF	DFDen	F Ratio	Prob > F
RAD	1	1	9.911	2.2670	0.1633
ZOL	1	1	9.911	0.1490	0.7077
RAD*ZOL	1	1	9.911	0.0000	0.9993
Percentage of Cortical Thickness Binned	4	4	814.9	12.5279	<.0001*
RAD*Percentage of Cortical Thickness Binned	4	4	814.9	3.3693	0.0095*
ZOL*Percentage of Cortical Thickness Binned	4	4	814.9	2.1084	0.0780
RAD*ZOL*Percentage of Cortical Thickness Binned	4	4	814.9	1.4912	0.2029

Table 3.5: 6 month mineral to matrix ratio fixed effect results from full-factorial mixed model analysis and significance ($p < 0.05$) shown by p-value in Prob>F column on the far right.

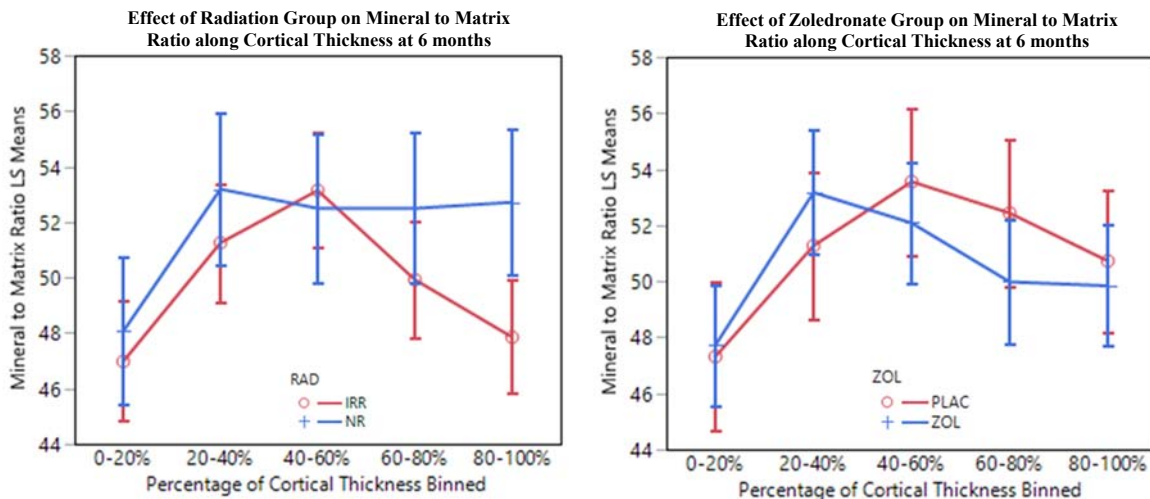


Figure 3.13: Mineral to matrix ratio least square means for 6 month time point along cortical thickness of the proximal tibia from endosteal to periosteal surface using the mixed model analysis. Left graph compares irradiated mice (red) to non-irradiated mice (blue) and right graph compared zoledronate treated mice (blue) with placebo treated mice (red).

Carbonate to Phosphate Ratio at 6 month time point (Figure 3.14): There was a significant effect of percentage of cortical thickness from endosteal surface for carbonate to phosphate ratio (Table 3.7). In addition, there was a significant interaction between zoledronate and percentage of cortical thickness ($p = 0.0324$), as well as radiation, zoledronate and percentage of cortical thickness ($p = 0.0013$).

Fixed Effect Tests					
Source	Nparm	DF	DFDen	F Ratio	Prob > F
RAD	1	1	11.76	0.5468	0.4741
ZOL	1	1	11.76	0.5952	0.4556
RAD*ZOL	1	1	11.76	0.1668	0.6904
Percentage of Cortical Thickness Binned	4	4	813.7	40.1712	<.0001*
RAD*Percentage of Cortical Thickness Binned	4	4	813.7	1.3153	0.2625
ZOL*Percentage of Cortical Thickness Binned	4	4	813.7	2.6470	0.0324*
RAD*ZOL*Percentage of Cortical Thickness Binned	4	4	813.7	4.5129	0.0013*

Table 3.6: 6 month carbonate to phosphate ratio fixed effect test results from full-factorial mixed model analysis and significance ($p < 0.05$) shown by p-value in Prob>F column on the far right

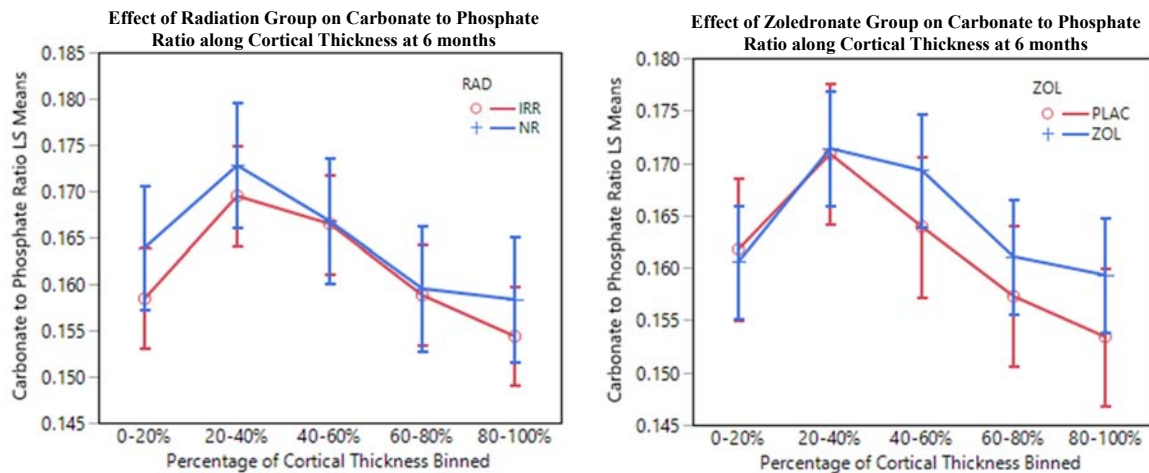


Figure 3.14: Carbonate to phosphate ratio least square means for 6 month time point along cortical thickness of the proximal tibia from endosteal to periosteal surface using the mixed model analysis. Left graph compares irradiated mice (red) to non-irradiated mice (blue) and right graph compared zoledronate treated mice (blue) with placebo treated mice (red).

Crystallinity at 6 month time point (Figure 3.15): There was a significant effect of percentage of cortical thickness from endosteal to periosteal surface for crystallinity (Table 3.8).

Fixed Effect Tests					
Source	Nparm	DF	DFDen	F Ratio	Prob > F
RAD	1	1	12.03	3.8774	0.0724
ZOL	1	1	12.03	1.0268	0.3309
RAD*ZOL	1	1	12.03	0.3834	0.5473
Percentage of Cortical Thickness Binned	4	4	815.8	5.8610	0.0001*
RAD*Percentage of Cortical Thickness Binned	4	4	815.8	0.8102	0.5188
ZOL*Percentage of Cortical Thickness Binned	4	4	815.8	1.8465	0.1180
RAD*ZOL*Percentage of Cortical Thickness Binned	4	4	815.8	1.8112	0.1246

Table 3.7: 6 month crystallinity fixed effect test results from full-factorial mixed model analysis and significance ($p < 0.05$) shown by p-value in Prob>F column on the far right

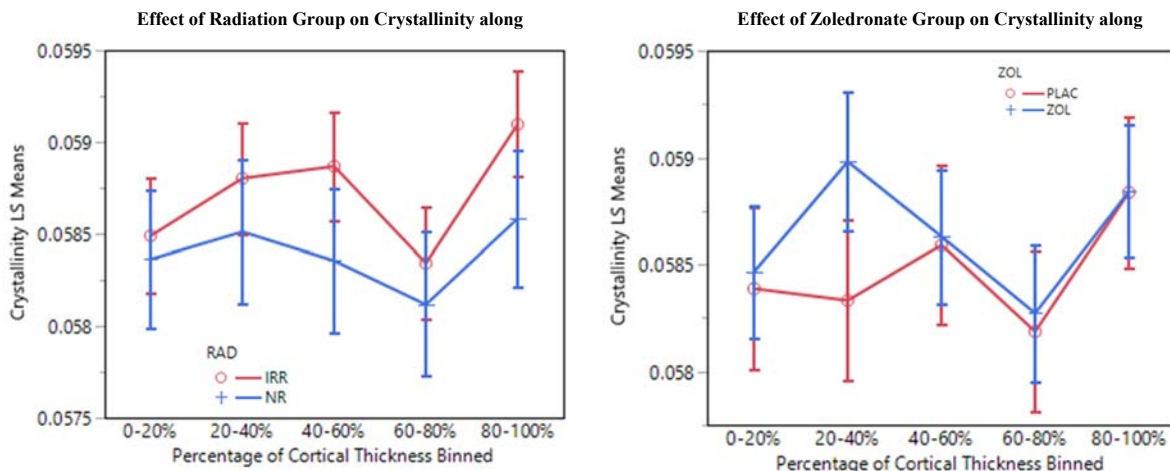


Figure 3.15: Crystallinity least square means for 6 month time point along cortical thickness of the proximal tibia from endosteal to periosteal surface using the mixed model analysis. Left graph compares irradiated mice (red) to non-irradiated mice (blue) and right graph compared zoledronate treated mice (blue) with placebo treated mice (red).

14 day analysis

Mineral to Matrix Ratio at 14 day time point (Figure 3.16): There was a significant effect of percentage of cortical thickness from endosteal surface for mineral to matrix ratio (Table 3.9). Additionally, there was a significant interaction between radiation group and percentage of cortical thickness from endosteal surface as well as between radiation, zoledronate and percentage of cortical thickness.

Fixed Effect Tests					
Source	Nparm	DF	DFDen	F Ratio	Prob > F
RAD	1	1	16.48	0.0520	0.8225
ZOL	1	1	16.48	0.8426	0.3719
RAD*ZOL	1	1	16.48	0.1972	0.6628
Percentage of Cortical Thickness from Endosteal Surface	4	4	866.9	29.9291	<.0001*
RAD*Percentage of Cortical Thickness from Endosteal Surface	4	4	866.9	4.6480	0.0010*
ZOL*Percentage of Cortical Thickness from Endosteal Surface	4	4	866.9	1.1660	0.3244
RAD*ZOL*Percentage of Cortical Thickness from Endosteal Surface	4	4	866.9	2.4575	0.0442*

Table 3.8: 14 day mineral to matrix ratio fixed effect test results from full-factorial mixed model analysis and significance ($p < 0.05$) shown by p-value in Prob>F column on the far right

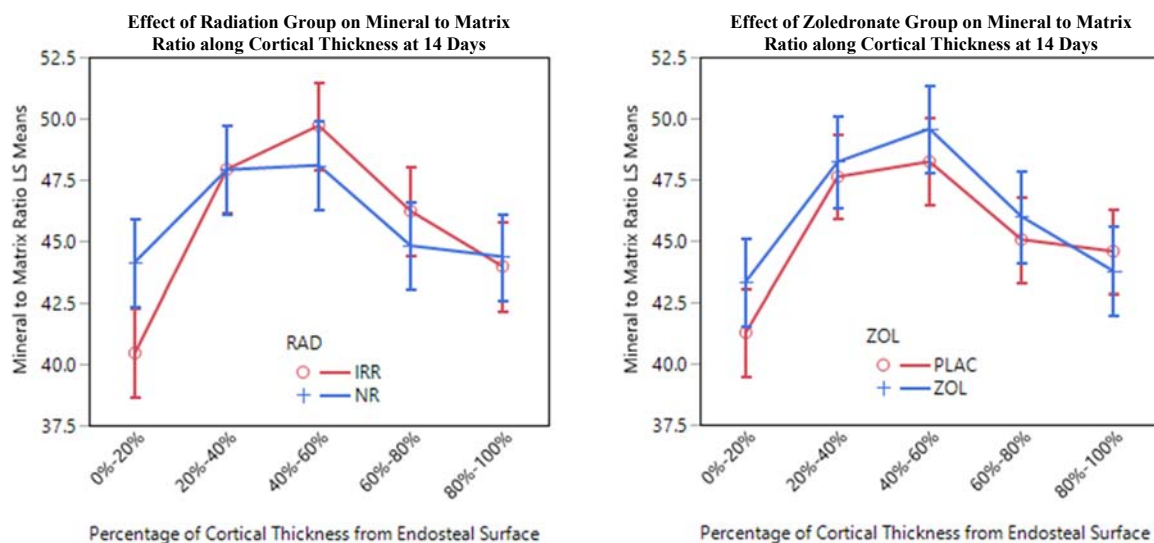


Figure 3.16: Mineral to matrix ratio least square means for 14 day time point along cortical thickness of the proximal tibia from endosteal to periosteal surface using the mixed model analysis. Left graph compares irradiated mice (red) to non-irradiated mice (blue) and right graph compared zoledronate treated mice (blue) with placebo treated mice (red).

Carbonate to Phosphate Ratio at 14 day time point (Figure 3.17): There was a significant effect of percentage of cortical thickness from endosteal surface for carbonate to phosphate ratio (Table 3.10). There was also a significant interaction between radiation and percentage of cortical thickness.

Fixed Effect Tests					
Source	Nparm	DF	DFDen	F Ratio	Prob > F
RAD	1	1	16.1	1.0000	0.3321
ZOL	1	1	16.1	0.2043	0.6573
RAD*ZOL	1	1	16.1	0.0804	0.7804
Percentage of Cortical Thickness from Endosteal Surface	4	4	865.9	98.4121	<.0001*
RAD*Percentage of Cortical Thickness from Endosteal Surface	4	4	865.9	3.8734	0.0040*
ZOL*Percentage of Cortical Thickness from Endosteal Surface	4	4	865.9	1.5383	0.1891
RAD*ZOL*Percentage of Cortical Thickness from Endosteal Surface	4	4	865.9	1.3698	0.2425

Table 3.9: 14 day carbonate to phosphate ratio fixed effect test results from full-factorial mixed model analysis and significance ($p < 0.05$) shown by p-value in Prob>F column on the far right

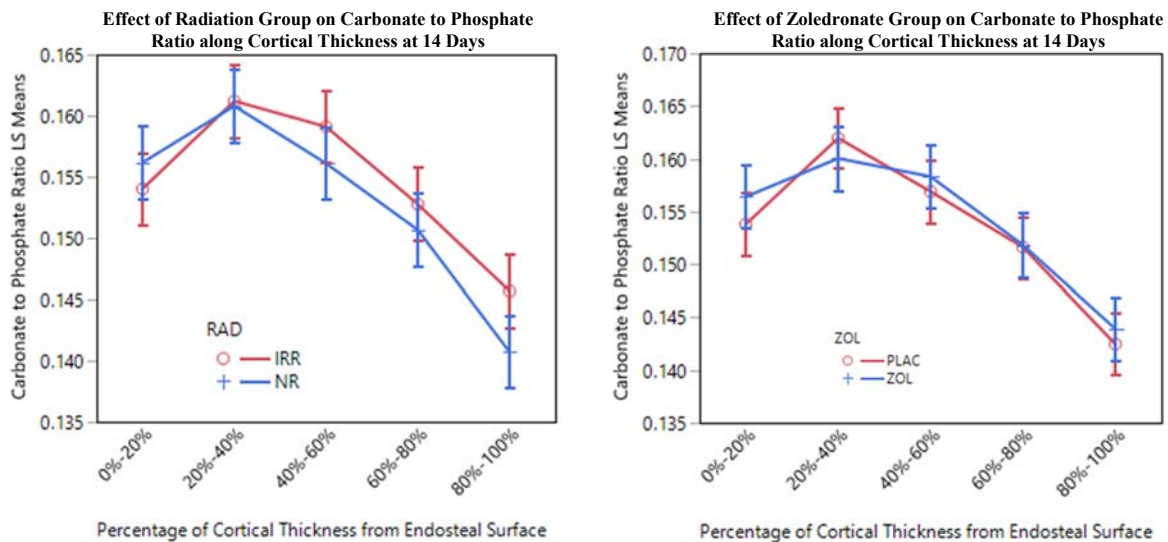


Figure 3.17: Carbonate to phosphate ratio least square means for 14 day time point along cortical thickness of the proximal tibia from endosteal to periosteal surface using the mixed model analysis. Left graph compares irradiated mice (red) to non-irradiated mice (blue) and right graph compared zoledronate treated mice (blue) with placebo treated mice (red).

Crystallinity at 14 day time point (Figure 3.18): There was a significant effect of percentage of cortical thickness from endosteal surface for crystallinity (Table 3.11). Also, there was a significant interaction between zoledronate and percentage of cortical thickness.

Fixed Effect Tests					
Source	Nparm	DF	DFDen	F Ratio	Prob > F
RAD	1	1	16.16	0.0258	0.8743
ZOL	1	1	16.16	0.2834	0.6017
RAD*ZOL	1	1	16.16	1.0649	0.3173
Percentage of Cortical Thickness from Endosteal Surface	4	4	866.2	5.4382	0.0003*
RAD*Percentage of Cortical Thickness from Endosteal Surface	4	4	866.2	2.0476	0.0858
ZOL*Percentage of Cortical Thickness from Endosteal Surface	4	4	866.2	3.7247	0.0052*
RAD*ZOL*Percentage of Cortical Thickness from Endosteal Surface	4	4	866.2	1.0591	0.3756

Table 3.10: 14 day crystallinity fixed effect test results from full-factorial mixed model analysis and significance ($p < 0.05$) shown by p-value in Prob>F column on the far right

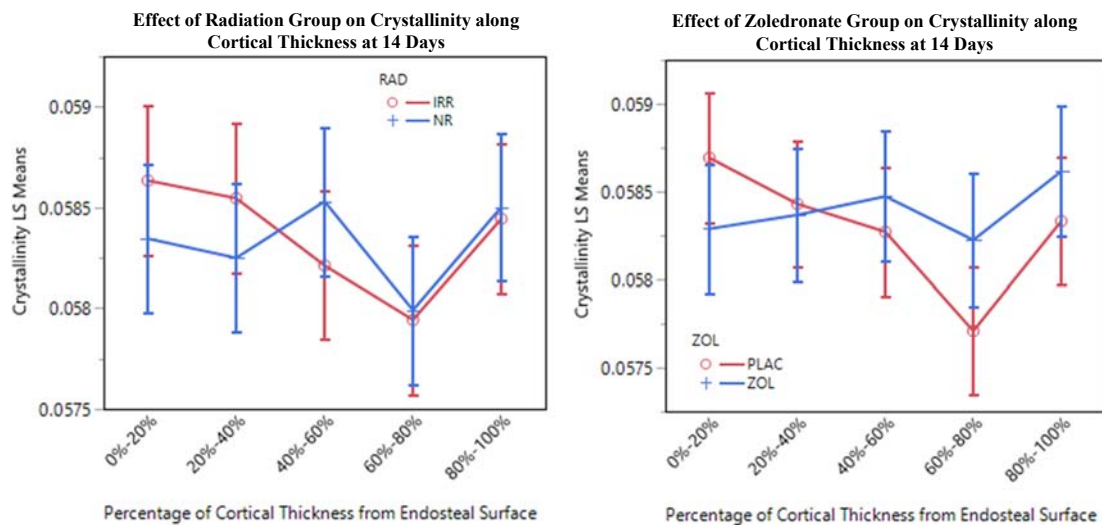


Figure 3.18: Crystallinity least square means for 14 day time point along cortical thickness of the proximal tibia from endosteal to periosteal surface using the mixed model analysis. Left graph compares irradiated mice (red) to non-irradiated mice (blue) and right graph compared zoledronate treated mice (blue) with placebo treated mice (red).

Discussion

The main goal of this study was to look at the effects of high-dose zoledronate treatment combined with fractionated irradiation on the material properties of bone in a mouse model. Radiation therapy for treatment of gynecological tumors has been shown to increase fracture risk [3, 83]. Bisphosphonates, such as zoledronate, offer the potential to prevent bone loss seen from radiation therapy, but their effect on material properties and bone quality is not fully understood [123]. Alterations in material properties of bone influence fracture risk and bone strength. Each of the parameters assessed using FTIR and Raman Spectroscopy have been correlated to bone strength. Increases in mineral to matrix ratio correlate with increased stiffness and brittleness, while decreased carbonate to phosphate ratio correlates with higher strain, greater maximum load and greater post-yield toughness [35]. Crystallinity is correlated with tissue-level strength and is inversely correlated to yield strain, ductility and fatigue-life [36, 37]. Also, by definition, the elastic modulus determined by nanoindentation measures bone's resistance to deformation when a stress is applied.

However, one of the challenges in comparing tissue level properties is that bone is a heterogeneous and dynamic tissue. Both aging and bone turnover result in changes in compositional markers, such as mineral to matrix ratio. Recently, heterogeneity has emerged as another predictor of bone strength. The literature suggests more heterogeneous bone, as measured as the full-width half maximum of target spectral markers, prevents crack propagation [36]. Therefore, it is important to keep in mind while interpreting results that a direct relationship between changes in bone quality and fracture risk is not clearly defined.

We observed a significant effect of the percentage of the cortical thickness from endosteal surface for all nanoindentation and Raman spectroscopy data collected. This result

highlights the complex relationship between material properties and overall bone strength [124]. New bone formation in a mouse takes place primarily on the endosteal and periosteal surfaces, as evidenced by fluorescent labeling in our study. Since mineral to matrix ratio and crystallinity are shown to increase with aging/time, it makes sense that the newer surface bone has different material properties than bone in the middle of the cortical segment [39]. By plotting least square mean values from a mixed model analysis of data by location in the cortical bone, important trends in material properties emerge. For example, at 14 days, irradiated bone modulus is lower than that of non-irradiated bone. By six months, the exact opposite is true. Chauhan et al. showed these changes also exist in human bone. Specifically, a single large dose (50 Gy) of radiation decreased mineral content and elastic modulus after 6 weeks [125]. Another study looked at four different time points following fractionated radiation and finds transient changes in material properties. Mineral to matrix ratio increases at 4 weeks compared to control, decreases compared to control at 12 weeks and is equivalent to control at 26 weeks [69]. Most post-radiation therapy fractures occur within two years of treatment [83]. These results emphasize the importance of establishing relevant time points for comparison between specimens. Osteoclast levels are elevated until fourteen days following irradiation, but then there is a long term loss of osteoclasts [63]. Without osteoclastic bone remodeling, the modulus increases, but the bone may become more brittle over time.

Zoledronate binds to hydroxyapatite and reduces bone turnover. Time plays a major role in the bone material changes affected by zoledronate, with long-term use (3+ years) shown to increase incidence of osteonecrosis of the jaw [126]. It is clear from the literature that there is an association between long-term bisphosphonate use and atypical femoral fractures (AFF) [127, 128]. Other studies have demonstrated that no changes in mean elastic modulus occur six-week

post single injection zoledronate treatment [129]. It is also important to characterize the rodent model to see how well the results mirror changes seen clinically. Our zoledronate dosing was intentionally large in order to determine potential changes before assessing a clinically relevant dose. Looking only at bone in the first 20% of the cortical thickness from endosteal surface, zoledronate-treated bone crystallinity is decreased compared to the placebo groups. At 6 months, the first 20% of the cortical thickness is equal to that of placebo groups. Additionally, the 20%-40% region zoledronate-treated bone is increased compared to placebo.

In the short term, treatment with zoledronate seems highly advantageous: preventing trabecular bone loss related to elevated osteoclast levels and potential increases in mineral to matrix ratio and elastic modulus. However, the long term effects on bone health are less clear. Radiation leads to a long term loss of osteoclasts, so the increased osteoclast suppression through zoledronate treatment could lead to decreased heterogeneity. The potential increases in crystallinity and modulus at the 6 month time point are not necessarily beneficial if the bone is becoming more homogenous and brittle. These compositional changes suggest the predominant mechanism for atypical fractures from zoledronate use is increased microcrack progression due to suppressed bone turnover [128].

Since certain vibrations in Raman peaks are known to be weaker than in FTIR and vice versa, these techniques are often used together [34]. If zoledronate treatment were to alter cortical bone material properties in a mouse model, we would expect those changes to be amplified with such high dosing. There is conflicting literature on the effect of zoledronate therapy on bone material properties and many of the discrepancies can be explained by the testing location within the bone or bisphosphonate dosing. For example, Little et al. found that a single dose (0.1 mg/kg) of zoledronate does not alter material properties of fracture healing in a

rat model [129]. In a study looking at callus formation, there were no tissue compositional changes evident with treatment of zoledronate detected by Raman spectroscopy, but there were differences between existing tibia and newly forming callus mineralization [130]. Increases in mineral to matrix ratio as well as increased tissue modulus resulting from zoledronate were found in another study looking at the treatment of osteoporotic sheep, though only at the trabecular surface [131]. Changes may be more apparent at the trabecular surface than the cortical bone and differences in material properties are site specific. Additionally, dosing plays a major role in detection of material changes. A study by Olejnik et al. revealed no changes in bone material properties with single low dose or fractionated low dose treatment compared to control animals [132]. However, with large, fractionated dosing, there was a significant decrease in crystallinity and hydroxyproline-to-proline ratio [132].

Another important consideration when looking at Raman, FTIR and nanoindentation data is the animal model, length scale and overall size of the areas of interest. Many of the studies that see changes in the material properties of bone are performed in larger animal models, such as ewes [131, 133]. Since bone is a heterogeneous tissue and there is generally a relatively large variance when working with biological tissues, techniques for assessment of nanoscale properties require a greater number of data points within each specimen to make comparisons. If interested in assessing actively forming bone compared to existing bone properties, the testable area in mice is much smaller than in large animals or humans, making it harder to confirm such changes. We chose to perform 24 indents per bone in order to account for spatial variability. However, the number of bones per group was rather small ($n=3$), though commonly used in nanoindentation studies [129].

Loss of trabecular bone mass following radiation therapy for cancer treatment is well-documented [57, 59, 134, 135]. As expected, a significant decrease in trabecular BV/TV is evident at 14 days in the IRR-PLAC mice compared to the NR-PLAC mice. By 6 months, the effects of aging have resulted in diminished BV/TV in the NR-PLAC equal to that of IRR-PLAC mice. Temporal studies of trabecular microarchitecture in C57BL/6 mice over mouse lifespan have been performed in both male and female mice. In female C57BL/6 mice, the distal femur trabecular BV/TV peaks by 6 weeks and then begins to decline [136]. Female C57BL/6 mice also experience a more severe trabecular bone decline than males in adolescence, but then maintain a similar steady decline to male mice during adulthood [136]. It is important to note that fractures resulting from radiation therapy typically happen soon after treatment, with 83% of fractures occurring within two years of treatment completion [83].

Following the initial large dosing, zoledronate was incorporated into the bone and continued to increase bone density through a slow release mechanism. Bisphosphonates adhere to the bone matrix and will persist in bone for a long time, as demonstrated by the trabecular compartment of the proximal tibia continuing to increase bone volume up to the 6 month time point despite administration within a two week window [137]. While we only looked at the proximal tibia region near the growth plate, other studies have shown that this bone formation from zoledronate is mainly seen in the area of the growth plate of long bones [138].

At the 14 day time point, trabecular BV/TV declined significantly compared to controls, yet finite element modeling to simulate compression of the proximal tibia revealed an overall increase in bone stiffness. Since homogenous material properties were applied to the model, this confirms there was an increase in cortical BV/TV at the proximal tibia as seen in previous studies [139].

In order to expand upon this model, future studies to look at trabecular material property changes as well as solely newly formed bone would help confirm changes resulting from radiation and zoledronate treatment. This study also suggests the importance of long-term characterization to see whether bone material and structural changes continue to progress or whether recovery and function are maintained.

This first assessment of material properties across three different testing techniques suggests changes are not as large in material as structure. However, small changes in material properties would result in large changes in function in the three dimensional environment and should be incorporated into functional assessment. Overall, the changes in structure caused by zoledronate treatment and radiation therapy are much more significant than the material changes in a mouse model.

CHAPTER 4: CHARACTERIZATION OF STRUCTURAL AND MATERIAL CHANGES IN BONE FOLLOWING KNEE JOINT BLEEDING IN MALE AND FEMALE FACTOR VIII DEFICIENT MICE

Introduction

Hemophilia refers to a class of bleeding disorders resulting from gene mutations in coagulation proteins located on the X chromosome [140]. Hemophilia A, caused by a Factor VIII deficiency, is the most common form of the disease worldwide [141]. While the disease affects mostly males, females can also have hemophilia or experience bleeding abnormalities as a carrier [142]. In both males and females, recurrent joint bleeding often leads to hemophilic arthropathy, characterized by reduced joint space and limited joint motion [143]. Additionally, reduced bone density has been observed in patients with hemophilia [72-76, 144].

In order to better understand the effects of hemarthrosis on joint health, a hemophilic mouse model for knee joint hemorrhage has been commonly used [79, 145-153]. Lau et al. demonstrated that joint hemorrhage in hemophilic mice causes an acute loss of trabecular bone in the injured joint as early as two weeks following knee injury [79]. The effects of rapid bone loss following hemarthrosis can greatly increase fracture risk, especially since research studies have shown FVIII deficiency independently leads to decreased bone mineral density [78, 154, 155]. The FVIII/von Willebrand Factor complex inhibits Receptor activator of nuclear factor kappa-B ligand (RANKL)-induced osteoclastogenesis [154]. Therefore, Factor VIII deficiency increases bone resorption through an increase in osteoclasts. Further research needs to be done to look at long-term effects of acute hemarthrosis on trabecular bone density.

In addition to trabecular bone loss, Lau et al. showed acute mineralization of the femur, tibia, fibula tendon insertion points, patella, patellar tendon, menisci, ligaments and cartilage following knee injury [79]. Evidence of increased osteoblast number and decreased IL-6 number at one day post-injury and roughening cortical bone surface by three days post-injury may explain this heterotopic mineralization [153]. By one week following injury, IL-6 levels increase and osteoclast number increases, resulting in bone resorption [153]. Calcifications of the knee joint may lead to osteoarthritis and further joint degradation through altered knee function [156]. The material properties and timeline of this calcification are not well understood.

The main goal of this study is to characterize the structure and material properties of both the femur and tibia following joint bleeding in both hemophilic male and female mouse models. Three time points were examined for changes in bone density using micro-computed tomography and fluorescent imaging. At twenty-eight days following knee injury, material properties of the distal femur were also examined using nanoindentation and Raman spectroscopy. The results from this study can help elucidate the timeline of disrupted bone formation following knee hemarthrosis in male and female hemophilic mice and suggest potential mechanisms for therapeutic targets.

Methods

Animals and Study Design

All investigations were approved by the University of North Carolina-Chapel Hill Institutional Animal Care and Use Committee and were performed in accordance with relevant guidelines and regulations. FVIII^{-/-} male and female mice were originally supplied by Dr. H. H. Kazazian Jr [157] and then bred in house and back-crossed 12 generations with C57Bl/6J mice. At 18-19 weeks of age, the FVIII^{-/-} mice were subjected to knee joint hemorrhage induced by puncture of the joint capsule using a Hamilton syringe with a 30.5-G needle via a small (~0.5 mm) incision of the skin overlying the patella. Following injury, all of the mice had access to Tylenol gel for pain relief.

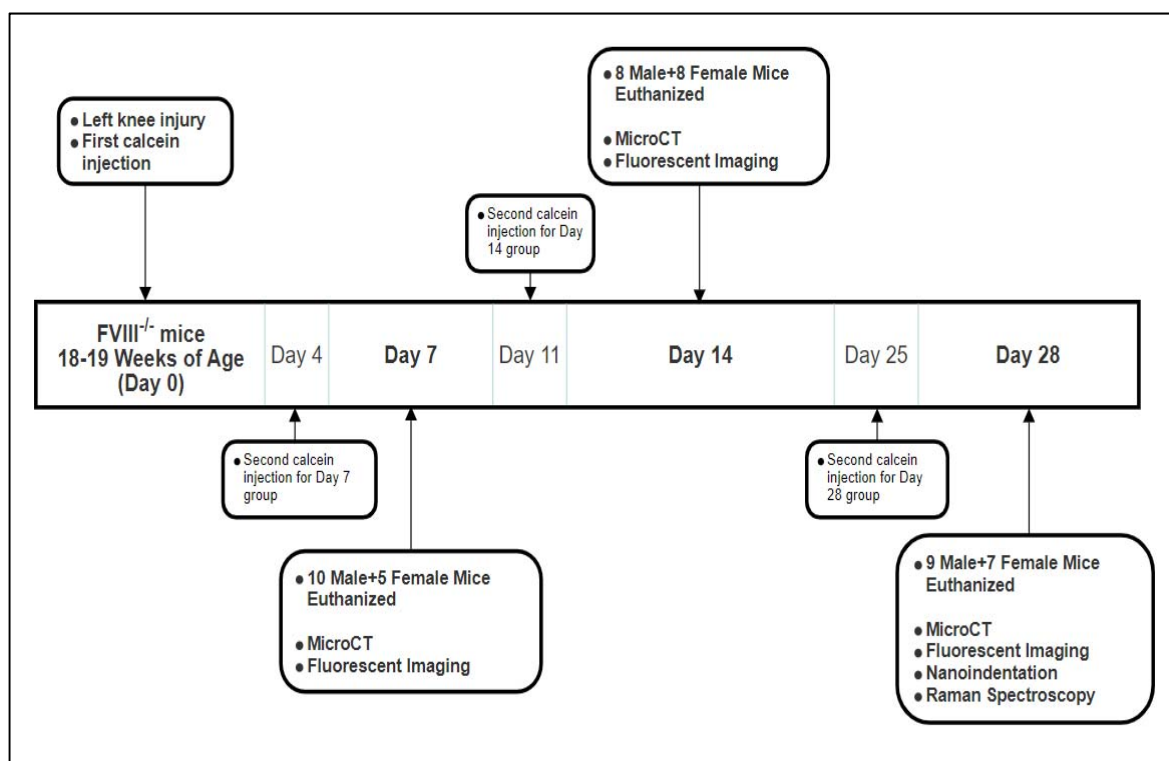


Figure 4.1: Study design schematic including timeline for assessment and methods for bone characterization

The mice were divided into four groups based on the number of days following injury for euthanization. There were 16 mice (9 Male, 7 Female) in the 28 day group, 16 mice (8 Male, 8 Female) in the 14 day group and 15 mice (10 Male, 5 Female) in the 7 day group. All mice received a calcein fluorescent label (10 mg/kg) injected subcutaneously on Day 0 and 3 days prior to euthanization as shown in Figure 4.1. The hindlimbs were removed at dissection and stored in ethanol at 4 degrees C. The three time points allow for characterization of the progression of the mineralization. All mice were weighed at euthanization.

Microcomputed Tomography

MicroCT scans of the whole knee joint, including proximal tibia and full femur, were taken at 10-micron isotropic voxel size (μ CT80; Scanco Medical AG, Brüttisellen, Switzerland). Both injured and contralateral limbs were scanned per mouse. The scans were acquired using a 70-kVp peak X-ray tube potential, a 0.5-mm Al filter and an integration time of 800 ms to reduce beam-hardening effects and improve the signal-to-noise ratio. Scanco software was used to analyze and quantify bone microarchitectural parameters from contoured regions. All contouring was performed semi-automatically to separate trabecular and cortical compartments. For the proximal tibia, a 1 mm section of the metaphysis just below the growth plate was chosen as the contour region. For the distal femur, a 1 mm section starting 0.5 mm proximal to the most proximal point of the continuous epiphyseal line is used as the contour region. Trabecular bone parameters including bone volume fraction (BV/TV), connectivity density (Conn.D), trabecular number (Tb.N), trabecular thickness (Tb.Th), trabecular separation (Tb.Sp), structure model index (SMI), volumetric bone mineral density (vBMD) were quantified for the proximal tibia and distal femur. For both the proximal tibia and distal femur, the cortical smoothness ratio was calculated by taking the smoothed cortical surface volume divided by the unsmoothed cortical

surface volume, to quantify the post-injury surface mineralization [153]. For the midshaft of the femur, BV/TV, periosteal volume, endosteal volume, cortical porosity, cortical thickness, bone area fraction (BA/TA), cortical vBMD and cortical tissue mineral density (Ct. TMD) were quantified.

Finite Element Analysis

The same 1 mm region of each male distal femur (injured and contralateral, all time points) used for microCT analysis was converted to a tetrahedral mesh for finite element analysis using Scanco software (SCANCO Medical FE-software, SCANCO Medical AG, Bassersdorf, Switzerland). Both whole bone and cortical bone stiffness were determined. For each bone section, homogenous material properties were applied to the distal femur by assigning a Young's Modulus of 10 GPa and Poisson's Ratio of 0.3. The distal surface was fixed and the proximal surface was displaced 0.02 mm longitudinally (2% strain) to simulate axial compression. The stiffness of each section was calculated by taking the resultant force on the distal surface divided by the displacement (0.02 mm). Trabecular bone stiffness was determined by subtracting the cortical bone stiffness from the corresponding whole segment stiffness.

Sample Preparation and Keyence Profilometry

Following microCT analysis, 8 male injured femurs and the 8 contralateral femurs were dehydrated in increasing concentrations of ethanol followed by one day in xylene. Then, each femur was embedded in poly(methyl)methacrylate (PMMA). Embedded bones were sectioned at 2 mm proximal to the distal end of the femur using a low speed diamond saw (Isomet, Buehler, Lake Bluff, IL). The embedded bones were then ground using wet silicon carbide paper (600, 800, 1200, 2400) and then polished using wet diamond lapping films (3 μm , 1 μm and 0.5 μm , Allied Tech). Samples were sonicated between each polishing step and at the end.

In order to ensure minimal surface roughness for nanoindentation testing, all embedded femurs were imaged using a Keyence Confocal Laser Scanning Microscope (Keyence VKx1100, Osaka, Japan). Through a combination of optical microscopy and laser profilometry, this microscope can obtain high resolution images and measure surface roughness.

Nanoindentation

Nanoindentation was performed for five randomly selected male mice, both injured and contralateral femurs, within the 28 day time point (n= 5 injured, n=5 uninjured). A Hysitron Ubi-1 Nanoindenter (Hysitron Inc., Minneapolis, MN) was used to perform all indents. Indents were performed with a Berkovich tip and a ramp and hold profile with a one minute hold at the maximum load. For uninjured femurs, two rows of ten indents per row spaced 20 μm between each indent were performed from endosteal to periosteal surface, spanning the cortical bone. The first row had a maximum load of 5 mN and the second row had a maximum load of 10 mN to make sure data is independent of load. To account for increased cortical thickness and increased porosity in the injured femurs, each of the two rows were split in half, with five indents starting from the endosteal surface spaced 10 μm apart and five indents starting from the periosteal surface spaced 10 μm apart. The maximum loads per row remained the same as the uninjured femurs (5mN and 10 mN). The test area within injured and uninjured femurs is shown in red rectangles in Figure 4.2.

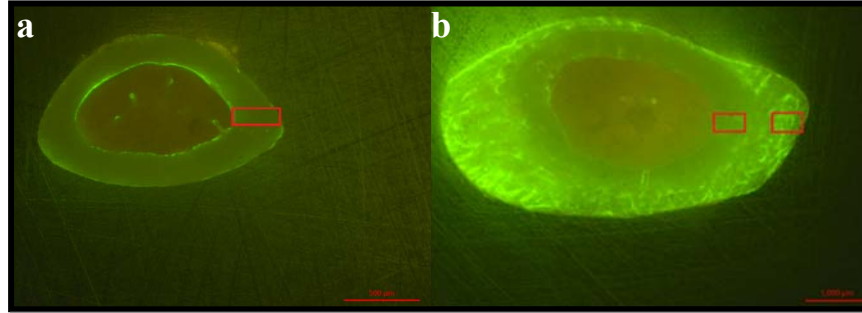


Figure 4.2: Fluorescent image of cross-section of 28 day distal femurs for (a) non-injured limb and (b) injured limb with red rectangles marking the area for nanoindentation. Fluorescent green (calcein label) represents bone formation following injury.

Raman Spectroscopy

Raman spectroscopy mapping of the distal femur was performed in order to evaluate bone composition from endosteal to periosteal surface. A Horiba XploRA PLUS Confocal Raman Microscope (HORIBA Scientific, Kyoto, Japan) with 785 nm wavelength laser and 1200 gr/mm grating was used to collect all spectra. The laser power was set to 100 and 3 accumulations of 10 seconds exposure were collected from each location in the array. Spectra were taken in three rows spaced 36.5 microns between rows (same region as nanoindentation from Figure 4.2). Within each row, seven spectra were taken evenly spaced throughout the cortical thickness from endosteal to periosteal surface (21 total spectra per bone). The baseline was subtracted using Horiba software and spectra were exported as .txt files for further analysis. Custom MATLAB code developed in Dr. Virginia Ferguson's lab by Dr. Chelsea Heveran was used to subtract a reference PMMA spectrum from each point and calculate all ratios. Mineral to matrix ratio was calculated by taking the area of the phosphate (961 cm^{-1}) peak divided by the area of the proline peak (855 cm^{-1}). Carbonate to phosphate ratios were evaluated by taking the area ratios of carbonate (1071 cm^{-1}) to phosphate (961 cm^{-1}). Lastly, crystallinity was determined by taking the inverse of the half-width at the full maximum height of the v1 phosphate peak.

Statistical Analysis

Significance was determined using SigmaPlot 12.0 (Systat Software Inc., San Jose, CA). The difference between the injured and uninjured limb (within each time point) was evaluated by a paired t-test at a level of significance of $p < 0.05$. If the differences were non-normally distributed, a Wilcoxon Signed Rank test was used to determine significance ($p < 0.05$). For nanoindentation and Raman spectroscopy data, measurements were averaged within each bone and the average value was used for the paired t-test.

Results

Final mouse weights within male and female groups were consistent at all three time points, showing mice did not gain weight following injury. Male weights were higher than female weights at all time points.

	Male	Female
7 day final body mass (g)	24.8 ± 1.0	20.3 ± 2.7
14 day final body mass (g)	23.3 ± 1.4	20.7 ± 1.5
28 day final body mass (g)	24 ± 1.3	19.6 ± 1.3

Table 4.1: Mean mouse body mass at dissection for each time point.

MicroCT

All microCT data for each time point can be found in Tables 4.2-4.4. Selected microCT parameter graphs can also be found in Figures 4.3 and 4.4. Example knee joint microCT images for an injured limb at 7 days, 14 days and 28 days can be found in Figure 4.5. Example fluorescent calcein images of the distal femur in male and female injured limbs can be found in Figure 4.6. Within male mice, there was a decrease in trabecular bone volume fraction (BV/TV) seven days following injury in both the proximal tibia (-15%) and distal femur (-29%) compared to the contralateral limb. At 14 days, the trabecular BV/TV continued to decline at the proximal

tibia (-26%) and distal femur (-44%) compared to the contralateral limb. By day 28, there was a 29% decline in the injured distal femur BV/TV, but no statistically significant differences between injured and contralateral proximal tibiae.

At the midshaft of the femur within male mice, there were no significant changes in cortical area or cortical porosity at day 7. Cortical area increased 19% at 14 days and 16% at 28 days following injury compared to the contralateral limb. Cortical porosity increased 2220% at 14 days and 97% at 28 days compared to the contralateral limb.

Smoothness ratio is a measure of surface roughness for quantification of post-injury surface mineralization. At day 7, smoothness had decreased 2% at the proximal tibia and 6% at the distal femur from injury compared to the contralateral limb. Smoothness following injury decreased 5% compared to the contralateral limb at day 14 and 4% at day 28 in both the proximal tibia and the distal femur.

Within female mice, there were no differences in trabecular BV/TV at the proximal tibia between injured and contralateral limbs at day 7, 14 or 28. At the distal femur, there was a 28% increase in trabecular BV/TV at day 14 from injury compared to the contralateral limb, but no changes seen at day 7 or day 28.

At the midshaft of the femur, there were no changes in the cortical area observed at day 7. There was a 21% and 37% increase in midshaft femur cortical area from injury compared to contralateral limb at day 14 and day 28, respectively. Cortical porosity increased 88% by day 7 in the injured femur and continued to increase 1076% at day 14 compared to contralateral limb. By day 28, there was a 570% increase in cortical porosity resulting from injury.

At day 7, there was a 4% decrease in smoothness ratio at the proximal tibia, but no statistically significant changes at the distal femur. At day 14, there was a 6% decline in

smoothness at the proximal tibia and a 5% decline at the distal femur compared to the contralateral limb. Smoothness decreased 5% and 6% at the proximal tibia and distal femur, respectively, at day 28.

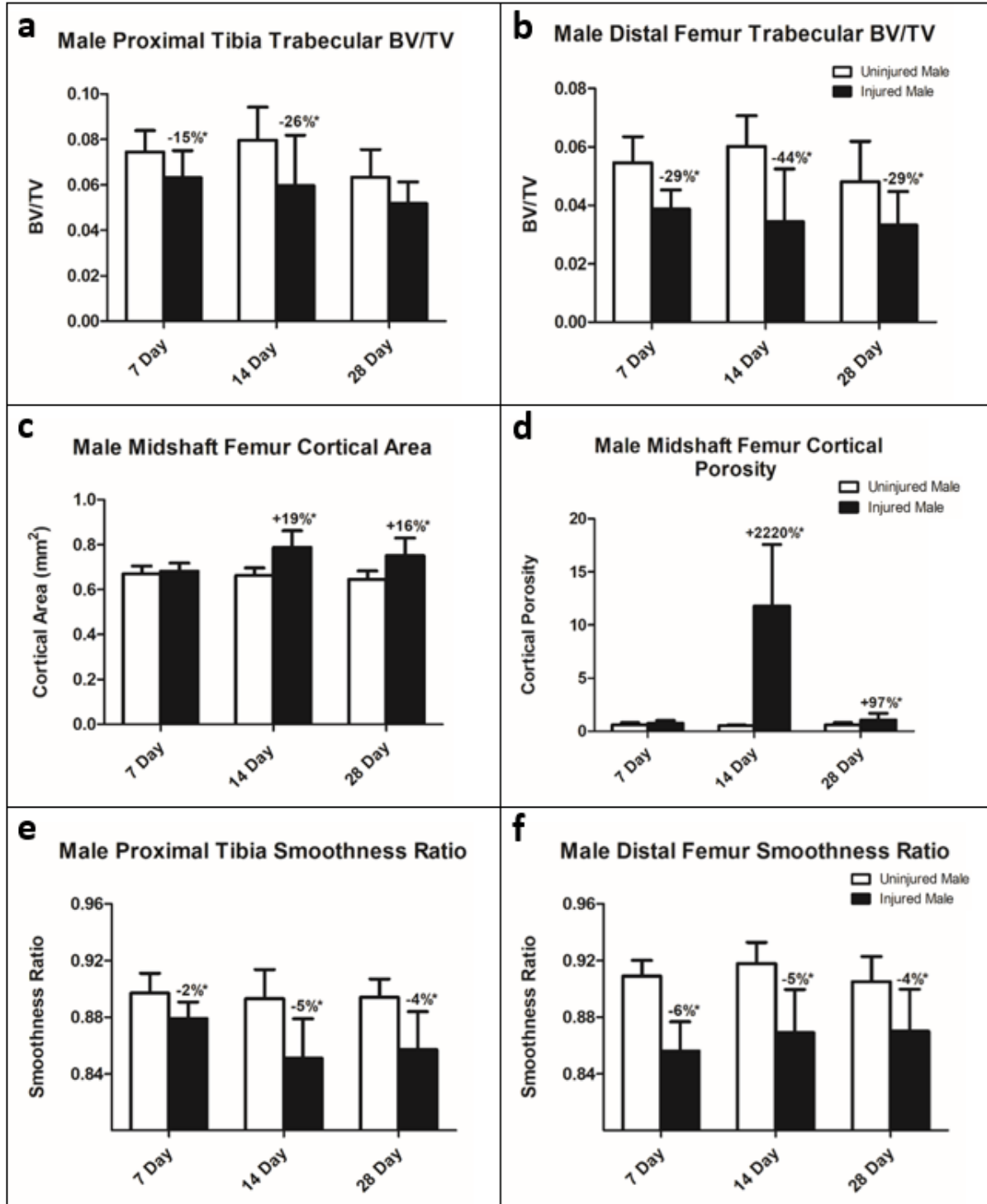


Figure 4.3: Selected microCT data comparing injured limb to contralateral limb in male mice. (a) Proximal tibia BV/TV (b) Distal femur BV/TV (c) Midshaft femur cortical area (d) Midshaft femur cortical porosity (e) Proximal tibia smoothness ratio (f) Distal femur smoothness ratio

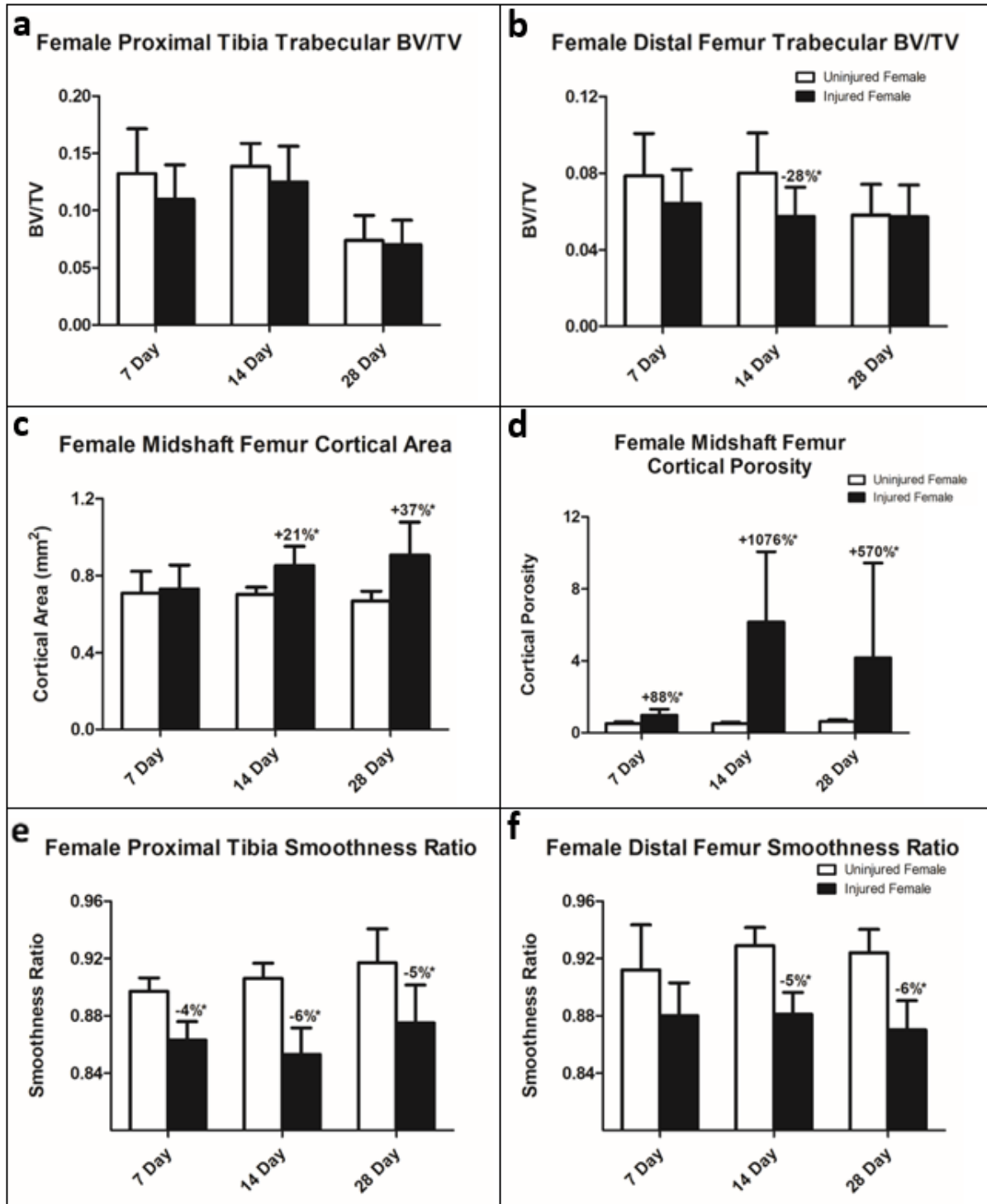


Figure 4.4: Selected microCT data comparing injured limb to contralateral limb in female mice. (a) Proximal tibia BV/TV (b) Distal femur BV/TV (c) Midshaft femur cortical area (d) Midshaft femur cortical porosity (e) Proximal tibia smoothness ratio (f) Distal femur smoothness ratio

7 Day MicroCT Analysis		Uninjured Male	Injured Male	Uninjured Female	Injured Female
7 Day Proximal Tibia Trabecular Analysis	BV/TV	0.075 ± 0.01	0.063 ± 0.01*	0.132 ± 0.04	0.110 ± 0.03
	vBMD (mgHA/cm³)	85.16 ± 11.7	75.43 ± 12.7	154.63 ± 41.1	134.03 ± 33.2
	Conn. Dens. (mm⁻³)	47.33 ± 14.6	42.82 ± 17.0	91.02 ± 39.05	67.78 ± 29.67
	Trab. Number (1/mm)	3.98 ± 0.2	3.84 ± 0.3*	3.98 ± 0.3	3.63 ± 0.2*
	Trab. Thickness (mm)	0.042 ± 0.002	0.038 ± 0.002*	0.047 ± 0.003	0.046 ± 0.004
	Trab. Spacing (mm)	0.25 ± 0.01	0.26 ± 0.02	0.25 ± 0.02	0.28 ± 0.02
7 Day Distal Femur Trabecular Analysis	BV/TV	0.05 ± 0.01	0.04 ± 0.01*	0.08 ± 0.02	0.06 ± 0.02
	vBMD (mgHA/cm³)	53.06 ± 8.06	38.16 ± 7.35*	88.08 ± 21.31	70.00 ± 15.47
	Conn. Dens. (mm⁻³)	83.71 ± 25.9	37.27 ± 13.7*	103.81 ± 22.4	85.10 ± 24.2
	Trab. Number (1/mm)	3.57 ± 0.2	3.36 ± 0.2*	3.64 ± 0.2	3.60 ± 0.3
	Trab. Thickness (mm)	0.034 ± 0.001	0.032 ± 0.001*	0.037 ± 0.003	0.036 ± 0.004
	Trab. Spacing (mm)	0.28 ± 0.02	0.30 ± 0.02*	0.27 ± 0.01	0.28 ± 0.02
7 Day Midshaft Femur Cortical Analysis	vBMD (mgHA/cm³)	741.5 ± 39.8	763.9 ± 28.9	759.1 ± 40.4	769.3 ± 55.6
	Peri. Volume (mm³)	0.57 ± 0.03	0.58 ± 0.04	0.60 ± 0.08	0.60 ± 0.07
	Endo. Volume (mm³)	0.24 ± 0.02	0.24 ± 0.03	0.25 ± 0.03	0.24 ± 0.02
	Cortical Porosity	0.62 ± 0.19	0.76 ± 0.26	0.52 ± 0.08	0.97 ± 0.34*
	Cortical Thickness (mm)	0.20 ± 0.01	0.20 ± 0.01	0.21 ± 0.02	0.22 ± 0.03
	Marrow Area (mm²)	0.48 ± 0.04	0.49 ± 0.05	0.50 ± 0.05	0.47 ± 0.03
	Total Area (mm²)	1.15 ± 0.05	1.17 ± 0.08	1.21 ± 0.16	1.20 ± 0.15
	BA/TA	0.583 ± 0.02	0.585 ± 0.02	0.584 ± 0.03	0.605 ± 0.04
	Cortical Area (mm²)	0.67 ± 0.03	0.68 ± 0.04	0.71 ± 0.11	0.73 ± 0.12
7 Day Smoothness Ratios	Prox. Tib. Smoothness Ratio	0.897 ± 0.01	0.879 ± 0.01*	0.897 ± 0.01	0.863 ± 0.01*
	Distal Fem. Smoothness Ratio	0.909 ± 0.01	0.856 ± 0.02*	0.912 ± 0.03	0.880 ± 0.02

Table 4.2: Mean and standard deviation for 7 day microCT data (*=significant p<0.05)

14 Day MicroCT Analysis		Uninjured Male	Injured Male	Uninjured Female	Injured Female
14 Day Proximal Tibia Trabecular Analysis	BV/TV	0.08 ± 0.01	0.06 ± 0.02*	0.14 ± 0.02	0.12 ± 0.03
	vBMD (mgHA/cm³)	92.8 ± 16.4	71.1 ± 25.3	157.5 ± 21.0	141.1 ± 34.2
	Conn. Dens. (mm⁻³)	49.7 ± 13.2	42.3 ± 21.2	99.6 ± 19.2	95.5 ± 19.9
	Trab. Number (1/mm)	4.01 ± 0.2	3.82 ± 0.3	3.92 ± 0.3	3.91 ± 0.1
	Trab. Thickness (mm)	0.042 ± 0.002	0.036 ± 0.005*	0.048 ± 0.003	0.045 ± 0.004
	Trab. Spacing (mm)	0.25 ± 0.01	0.26 ± 0.02	0.25 ± 0.02	0.25 ± 0.01
14 Day Distal Femur Trabecular Analysis	BV/TV	0.06 ± 0.01	0.03 ± 0.02*	0.08 ± 0.02	0.06 ± 0.02*
	vBMD (mgHA/cm³)	61.9 ± 14.6	36.2 ± 20.1*	81.3 ± 21.4	65.3 ± 18.3
	Conn. Dens. (mm⁻³)	77.1 ± 18.4	42.0 ± 31.6*	107.8 ± 26.2	70.9 ± 20.7*
	Trab. Number (1/mm)	3.61 ± 0.1	3.17 ± 0.4*	3.60 ± 0.3	3.42 ± 0.2
	Trab. Thickness (mm)	0.038 ± 0.002	0.032 ± 0.004*	0.038 ± 0.002	0.036 ± 0.003
	Trab. Spacing (mm)	0.28 ± 0.01	0.32 ± 0.04*	0.28 ± 0.02	0.29 ± 0.01
14 Day Midshaft Femur Cortical Analysis	vBMD (mgHA/cm³)	749.3 ± 16.4	741.4 ± 34.4	758.4 ± 40.6	769.8 ± 20.0
	Peri. Volume (mm³)	0.58 ± 0.03	0.64 ± 0.04*	0.59 ± 0.03	0.68 ± 0.05*
	Endo. Volume (mm³)	0.25 ± 0.02	0.25 ± 0.01	0.24 ± 0.02	0.25 ± 0.01
	Cortical Porosity	0.53 ± 0.07	11.8 ± 5.8*	0.52 ± 0.08	6.15 ± 3.9*
	Cortical Thickness (mm)	0.200 ± 0.004	0.20 ± 0.01	0.21 ± 0.01	0.21 ± 0.01
	Marrow Area (mm²)	0.50 ± 0.04	0.49 ± 0.03	0.48 ± 0.04	0.51 ± 0.02
	Total Area (mm²)	1.16 ± 0.06	1.28 ± 0.07*	1.19 ± 0.05	1.36 ± 0.11*
	BA/TA	0.57 ± 0.02	0.62 ± 0.03*	0.59 ± 0.03	0.63 ± 0.02*
	Cortical Area (mm²)	0.66 ± 0.03	0.79 ± 0.07*	0.70 ± 0.04	0.85 ± 0.10*
14 Day Smoothness Ratios	Prox. Tib. Smoothness Ratio	0.893 ± 0.02	0.851 ± 0.03*	0.906 ± 0.01	0.853 ± 0.02*
	Distal Fem. Smoothness Ratio	0.918 ± 0.01	0.869 ± 0.03*	0.929 ± 0.01	0.881 ± 0.02*

Table 4.3: Mean and standard deviation for 14 day microCT data (*=significant p<0.05)

28 Day MicroCT Analysis		Uninjured Male	Injured Male	Uninjured Female	Injured Female
28 Day Proximal Tibia Trabecular Analysis	BV/TV	0.06 ± 0.01	0.05 ± 0.01	0.07 ± 0.02	0.07 ± 0.02
	vBMD (mgHA/cm³)	71.6 ± 13.7	52.6 ± 11.0	89.7 ± 26.2	78.6 ± 25.4
	Conn. Dens. (mm⁻³)	25.4 ± 8.9	23.5 ± 13.7*	41.9 ± 19.7	46.4 ± 20.2
	Trab. Number (1/mm)	3.4 ± 0.2	3.2 ± 0.4	3.2 ± 0.2	3.2 ± 0.2
	Trab. Thickness (mm)	0.044 ± 0.002	0.044 ± 0.005	0.044 ± 0.003	0.043 ± 0.004
	Trab. Spacing (mm)	0.29 ± 0.02	0.32 ± 0.06*	0.31 ± 0.02	0.31 ± 0.02
28 Day Distal Femur Trabecular Analysis	BV/TV	0.05 ± 0.01	0.03 ± 0.01*	0.06 ± 0.02	0.06 ± 0.02
	vBMD (mgHA/cm³)	47.07 ± 16.7	30.72 ± 15.8*	61.00 ± 16.23	62.67 ± 18.6
	Conn. Dens. (mm⁻³)	46.2 ± 18.8	22.7 ± 11.7*	72.6 ± 16.1	61.5 ± 17.0*
	Trab. Number (1/mm)	3.07 ± 0.29	2.75 ± 0.24	3.10 ± 0.19	3.09 ± 0.21
	Trab. Thickness (mm)	0.042 ± 0.005	0.040 ± 0.005*	0.040 ± 0.004	0.041 ± 0.004
	Trab. Spacing (mm)	0.33 ± 0.03	0.37 ± 0.04*	0.33 ± 0.02	0.33 ± 0.02
28 Day Midshaft Femur Cortical Analysis	vBMD (mgHA/cm³)	750.3 ± 40.0	748.3 ± 29.3	763.3 ± 38.4	762.8 ± 34.1
	Peri. Volume (mm³)	0.57 ± 0.04	0.65 ± 0.05*	0.57 ± 0.04	0.73 ± 0.11*
	Endo. Volume (mm³)	0.24 ± 0.03	0.27 ± 0.02*	0.24 ± 0.02	0.28 ± 0.03*
	Cortical Porosity	0.59 ± 0.21	1.18 ± 0.72*	0.62 ± 0.10	4.17 ± 5.27*
	Cortical Thickness (mm)	0.20 ± 0.01	0.20 ± 0.01	0.21 ± 0.01	0.20 ± 0.03
	Marrow Area (mm²)	0.48 ± 0.05	0.55 ± 0.04*	0.48 ± 0.04	0.56 ± 0.05*
	Total Area (mm²)	1.13 ± 0.07	1.29 ± 0.10*	1.15 ± 0.07	1.46 ± 0.21*
	BA/TA	0.58 ± 0.02	0.58 ± 0.02	0.58 ± 0.03	0.62 ± 0.03
	Cortical Area (mm²)	0.65 ± 0.04	0.75 ± 0.07*	0.67 ± 0.05	0.91 ± 0.17*
28 Day Smoothness Ratios	Prox. Tib. Smoothness Ratio	0.896 ± 0.01	0.861 ± 0.03*	0.917 ± 0.02	0.875 ± 0.03*
	Distal Fem. Smoothness Ratio	0.905 ± 0.02	0.870 ± 0.03*	0.924 ± 0.02	0.870 ± 0.02*

Table 4.4: Mean and standard deviation for 28 day microCT data (*=significant p<0.05)

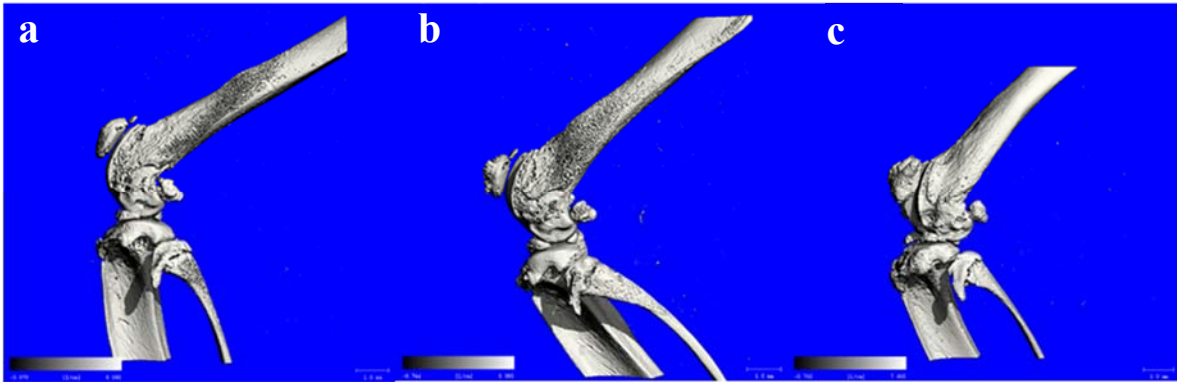


Figure 4.5: MicroCT images of injured knee joint at (a) 7 days (b) 14 days and (c) 28 days following injury

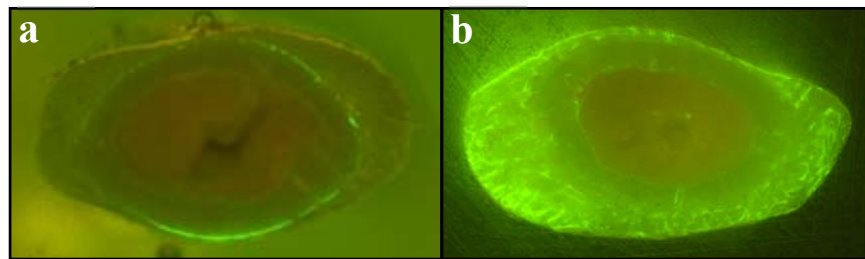


Figure 4.6: Fluorescent imaging of calcein label of injured distal femur at 28 days following injury. (a) Female injured limb (b) Male injured limb

Finite Element Analysis

At 7 days following injury, cortical bone stiffness declined 16%, trabecular stiffness declined 31% and whole bone (trabecular+cortical) stiffness declined 31%. At 14 days following injury, cortical bone stiffness increased 66%, trabecular bone stiffness increased 48% and whole bone stiffness increased 59%. There were no changes in trabecular bone stiffness at 28 days. Cortical bone stiffness increased 30% and whole bone stiffness increased 29% at day 28. All comparisons are made with respect to uninjured contralateral limbs and corresponding graphs are found in Figure 4.7.

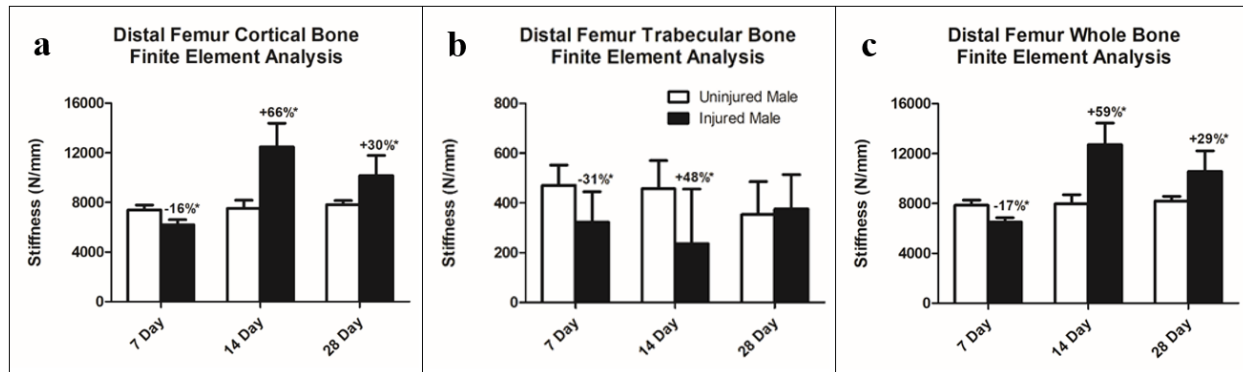


Figure 4.7: Male distal femur finite element analysis for (a) cortical bone only (b) trabecular bone only and (c) trabecular and cortical bone combined stiffness

Keyence Profilometry

An example laser+optical image with area of interest highlighted as well as a surface roughness profile is shown in Figure 4.8 below. All samples were polished until the entire surface roughness for nanoindentation testing was less than 5 μm . For the example shown, the maximum surface roughness value is 2.534 microns.

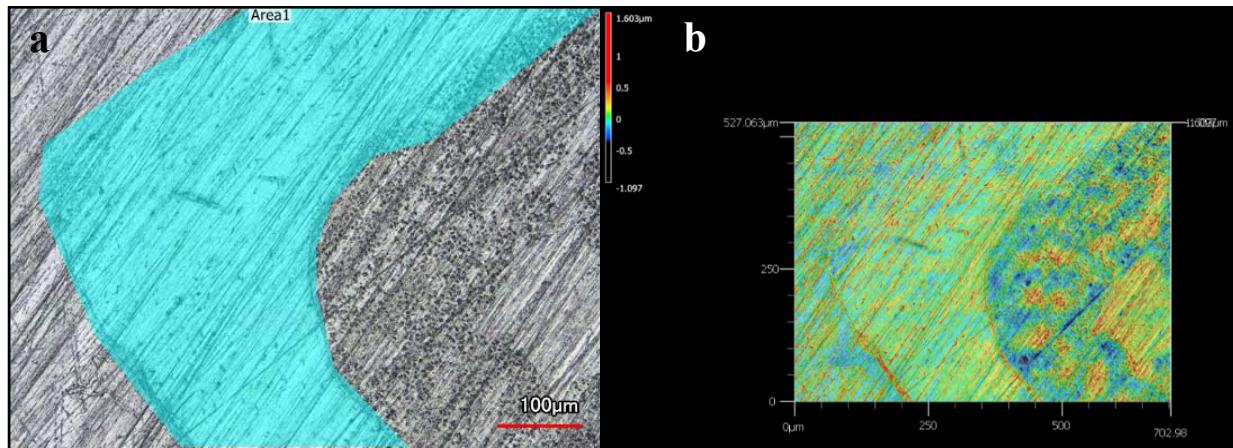


Figure 4.8: Example Keyence profilometry assessment (a) selected region for quantified surface roughness and (b) heat map image of bone section for surface roughness with maximum difference under 5 microns.

Nanoindentation

At 28 days, there was a 23% decrease in mean reduced modulus at the distal femur cortical bone in the injured group compared to the contralateral group (Figure 4.9). The variance of the data also decreased in the injured group.

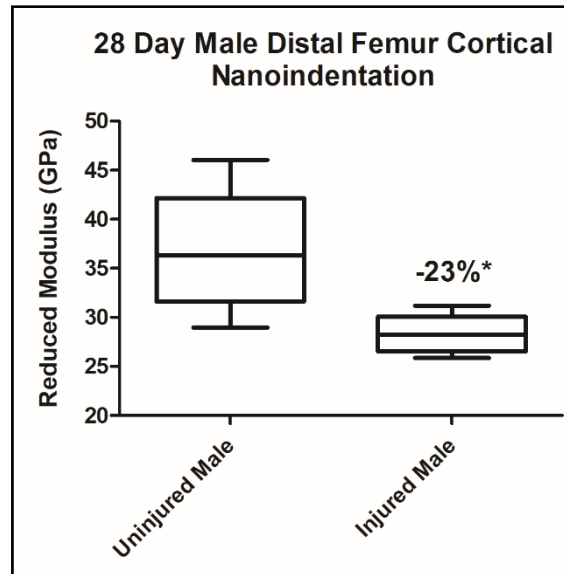


Figure 4.9: Box and whisker plot comparison of reduced modulus for uninjured and injured male distal femurs at 28 days

Raman Spectroscopy

At 28 days, there was a 27% decrease in mineral to matrix ratio in the injured distal femur cortical bone compared to contralateral limbs (Figure 4.11). There were no statistically significant changes between injured and contralateral limbs for carbonate to phosphate ratio or crystallinity (4.10).

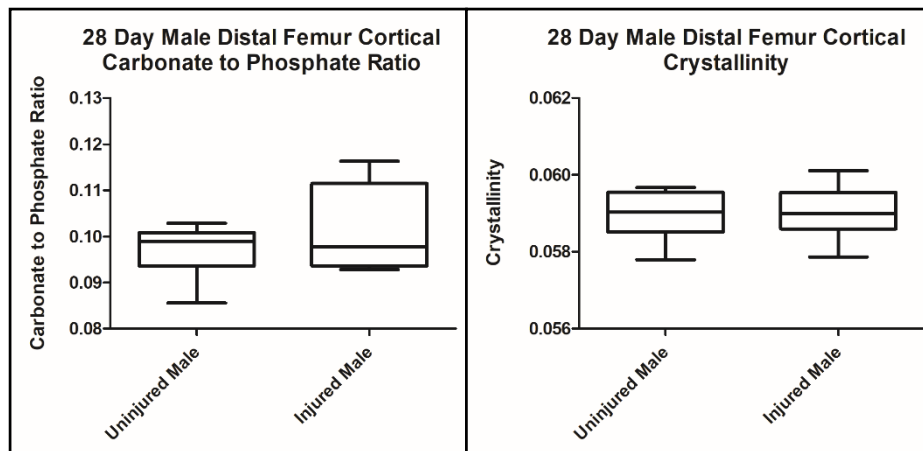


Figure 4.11: Box and whisker plots for comparison of (a) carbonate to phosphate ratio and (b) crystallinity for uninjured and injured male distal femurs at 28 days

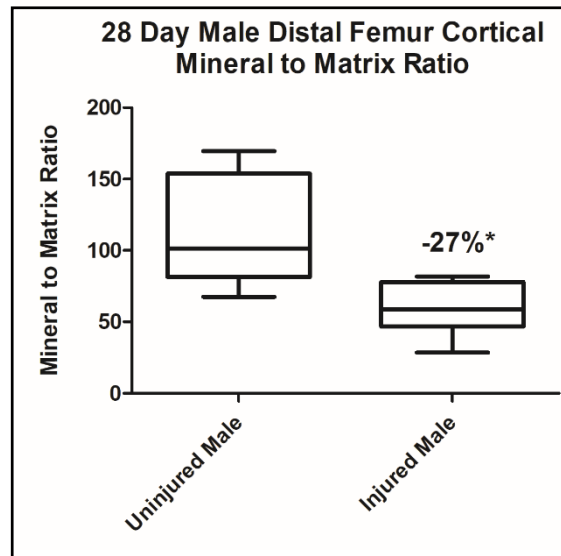


Figure 4.10: Box and whisker plot comparison of mineral to matrix ratio for uninjured and injured male distal femurs at 28 days

Discussion

In recent years, there have been many advancements made in therapies to treat hemophilia, including gene therapy and monoclonal antibodies [158]. These breakthroughs have increased life expectancy in the hemophilia population, but also highlight the importance of fully characterizing the potential short and long-term effects of a joint bleed in order to improve quality of life. In this study, structural and material alterations to the tibia and femur following knee hemarthrosis are quantified in both male and female Factor VIII deficient mice.

In the male mice, a decline in trabecular BV/TV in both proximal tibia and distal femur is evident by seven days and continues to decrease further at day 14. At day 28, there is a smaller difference in contralateral and injured trabecular BV/TV in the tibia and femur than day 14. However, this seems to be due to the contralateral limb losing BV/TV, rather than a recovery in trabecular bone volume. A comparison with uninjured mice would be necessary to determine whether this is a systemic effect of injury on the contralateral limb or an effect of aging. In general, female trabecular bone seems to be less affected by joint injury than males. There were no significant changes in BV/TV between injured and contralateral limbs in the female proximal tibia at any time point. There was a significant decrease in female distal femur BV/TV at day 14, though less than the change seen in males. Female mice also had higher starting values for BV/TV at both the proximal tibia and distal femur than male mice.

In the cortical compartment, as evaluated in the midshaft region of the femur, female mice experienced more dramatic increases in cortical area and porosity than male mice. This elevated response to joint injury could potentially be due to an increased immune response. Women have a higher incidence of autoimmune disease and estrogen is known to have an immune-enhancing effect on bone [159, 160].

In addition to differences in trabecular and cortical responses, male and female mice have a different timeline for bone formation following injury. At the 28 day time point, the cortical thickening is evident in both male and female femurs, though only the formation in the male mice is fluorescent. Calcein labels were given at injury and three days prior to euthanization.

In the cortical region of the male distal femur, both mean reduced modulus and mineral to matrix ratio decreased in the injured limb. Interestingly, the variance of mineral to matrix ratio and reduced modulus also decreased in the injured limb. Heterogeneity in nanoscale material properties and mineralization has emerged as a contributor to bone fracture toughness and energy dissipation [161]. Increased heterogeneity should prevent crack initiation and propagation within bone [162]. A decrease in variance suggests more homogenous bone and therefore, cracks are more likely to propagate along the bone.

Clinically, low bone density has been recognized in both adults and children with hemophilia [72-75]. There are a variety of factors that contribute to this problem, including limited physical activity, joint bleeding and the effects of HIV or other infections [73]. The results from this study confirm that joint injury can further exacerbate decreased trabecular bone density and also alter morphology of the cortical bone. Previous reports using ultrasound have described the bone to have osteophytes and surface erosion following hemarthrosis [163]. The smoothness ratio described in this study offers a way to quantify the phenotypic response to hemophilic injury.

Overall, the identification of cortical mineralization (also described as heterotopic ossification [79, 153]) following hemarthrosis is fairly new and this is the first time a time course has been described. Based on this study, most cortical formation happens within 7-14 days following hemarthrosis. The porosity continues to fill in up to the 28 day timepoint and the new

formation begins to look more like normal bone. Including the female mice in this study provides suggestions about mechanisms that could be contributing to bone alterations, including hormones and inflammatory immune response. In future studies, we would like to look at long-term effects of knee hemarthrosis to see if the cortical mineralization is resorbed with time or if cortical thickness increases.

CHAPTER 5: CONCLUSION AND FUTURE WORK

Summary of Findings

The goal of this work was to characterize structural and material changes of bone in a mouse model for radiation therapy induced estrogen deficiency and hemophilic joint bleeding. Both disease states are associated with altered bone phenotype, but lack full understanding of the factors contributing to bone fragility or optimal targets for therapeutic development. Through microCT, DEXA, finite element analysis, fluorescent imaging, FTIR, Raman spectroscopy and nanoindentation assessment, bone alterations were quantified at multiple length scales to provide a more complete evaluation of bone strength. Additionally, multiple time points were characterized to determine whether bone changes were transient or persisted long-term.

In Chapter 2, bone morphological parameters and structural stiffness in the trabecular and cortical compartments were quantified at three skeletal sites following concurrent fractionated radiation and estrogen deficiency. A biologically effective dose (BED) was used to simulate cervical cancer treatment. First, a validation experiment demonstrated greater loss in trabecular bone density from multiple fractions of radiation compared to a single large dose. Following dose validation, fractionated irradiation using a BED led to significant decline in trabecular bone volume and stiffness. Interestingly, radiation caused an increase in cortical thickness and stiffness at the proximal tibia. The combination of irradiation with ovariectomy had an additive effect at the proximal tibia, with greater trabecular bone loss seen than in either procedure alone. Ovariectomy had a systemic effect, while skeletal radiation damage was largely specific to trabecular bone within the X-ray field.

The mouse model characterization from Chapter 2 allowed for assessment of the ability of high-dose zoledronate treatment to prevent bone loss from radiation therapy in Chapter 3. Zoledronate prevented loss of trabecular bone volume fraction at the 3 and 14 day time points. At six months, there were extreme structural changes (+1140% BV/TV), with the trabecular compartment almost completing filling in with bone. Average changes in material properties were less apparent. However, location within cortical thickness from endosteal to periosteal surface proved to have a significant effect in the mixed model analysis for both nanoindentation and Raman spectroscopy. Newer bone formed close to the endosteal surface showed trends of increased modulus, mineral to matrix ratio and crystallinity at 6 months, though not statistically significant ($p < 0.05$). At 14 days, newer bone following irradiation has a trending lower modulus compared to controls, while the exact opposite is true at six months. Interestingly, heterogeneity of tissue is also used to quantify bone health, with increases in heterogeneity considered beneficial [36]. The mixed model results highlight the complexity of the relationship between material properties and overall bone strength as well as the importance of using multiple modalities (nanoindentation, FTIR, Raman spectroscopy) to define material alterations.

In Chapter 4, insights from material characterization in Chapter 3 led to the characterization of rapid mineralization and cortical thickening at the knee joint following joint injury in a male and female Hemophilia A mouse model. Fluorescent images and microCT morphometric analysis revealed large areas of new cortical bone formation at the distal femur within the 7 day time point and persisting through the 28 day time point. Most cortical bone formation happened within 7-14 days following hemarthrosis. The cortical porosity continued to fill in up to the 28 day time point. Additionally, significant loss of trabecular bone was evident at all time points in the male distal femur. Female mice saw fewer changes in trabecular

microarchitecture, but large changes in cortical thickness and porosity. Male and female differences following joint injury may be related to immune response [159, 160]. In addition to structural changes, there were large changes in material properties at the 28 day time point. Distal femur cortical reduced modulus and mineral to matrix ratio decreased significantly. Reduced modulus and mineral to matrix variability also decreased.

Beyond the quantitative data gathered, considerations for experiment design, sample preparation assessment and data interpretation were highlighted through this work. First, length scale is critical in the discussion of relating structural and material properties to strength. Whether or not material changes have “positive” or “negative” impacts on bone health must be discerned at each hierarchical level. For example, from the literature, an increase in mineral to matrix ratio correlates with an increase in bone strength [39]. However, mineral to matrix ratio alone does not provide that information. Assessment at the micrometer level would be necessary to validate the functional contribution of that material change. Addition of mineral alone may not influence nanoindentation modulus if the mineral is not added in a way that can transmit strain. In other words, the increase in mineral is only useful if it is organized in a way that also increases tissue modulus. Similar thought processes apply to interpretation of all material parameters.

Variability is just as important as material parameters of interest. Drugs such as zoledronate offer huge benefits for preserving bone structure, but ultimately halt bone remodeling. Evidence for decreased remodeling can be seen through increases in crystallinity with decreases in crystallinity variability. Though the bone structure may remain intact, this homogenization of mature mineral in a localized region may cause the bone to become brittle and allow microcracks to propagate. For this reason, the crystallinity increase is only beneficial to bone health if there is still tissue heterogeneity.

For future studies, I would take a more targeted approach in locations for material testing. Since we know bone mineralizes over time, new and old bone properties are expected to be different. For this reason, I would focus on the new or old regions and gather more data within each region, rather than equally spaced through the cortical thickness. A fluorescent label would be valuable in defining new and old bone.

The development of the Oliver-Pharr equation led to a significant increase in use of nanoindentation in the literature. However, numerous factors other than load and displacement go into the measured values. Surface roughness, tip geometry, maximum depth, distance from bone surface (must assume continuum for Oliver-Pharr method), thermal drift, embedding medium, hydration state, hold time at maximum load and loading profile are just a few factors worth mentioning that influence the modulus value obtained [164]. Ideally, to compare values, all of the testing factors should be the same. One small step towards understanding values reported would be the addition of surface profilometry data following sample preparation. The maximum surface roughness measurement in combination with depth information would ensure the indenting protocol was actually probing the bone and following the well-defined contact geometry necessary to use Oliver-Pharr calculations [165].

The mixed model analysis provides a more thorough understanding of the material properties data and informs future studies. In gathering data in bone, often times there will be outliers representative of pores in the bone. This leads to unequal number of data points per row or sample, invalidating the assumptions required to run an ANOVA. Therefore, values are often averaged across a sample, reducing each bone to one data point within a treatment group. As a heterogeneous, biological sample, one data point does not well represent overall bone material or variability. For this reason, a mixed model can account for both random effects (such as sample

number) as well as all potential fixed effects. All post-hoc analyses can still be run with a mixed model to understand local changes taking place and inform further studies to focus on those specific locations.

Overall, this work demonstrates the importance of characterization of bone health at multiple length scales and time points. Though zoledronate offers the potential to decrease bone loss seen following radiation therapy and estrogen deficiency, concerns about long-term effects on bone mineralization and variability require further investigation with dosing or a less potent bisphosphonate. In the hemarthrosis model, the timeline of cortical mineralization and trabecular bone decline has been characterized in a male and female model to help elucidate mechanisms for therapeutic targets.

Limitations

One of the limitations of mouse studies is that mice lack Haversian systems and do not undergo osteonal remodeling. The mouse cortical bone is a mixture of woven bone and circumferential lamellar bone. Typically, circumferential lamellar bone is laid down on the periosteal surface and resorption occurs on the endosteal surface, though formation can also occur at the endosteal surface [166]. Therefore, changes in osteonal bone remodeling in humans will not be represented in the mouse model.

For changes in trabecular architecture, the proximal tibia and distal femur regions are analyzed instead of the femoral neck. Most pelvic fractures resulting from pelvic radiation therapy occur at the femoral neck [167]. However, in a mouse, there is very little trabecular bone present due to the small size. Therefore, changes are more evident in trabecular-rich areas, such as the proximal tibia and distal femur.

Additionally, material properties characterization in Chapter 3 had a small sample size ($n=3$). In order to account for variability in bone tissue, many data points are gathered per bone. However, in order to increase the power in future studies, I would incorporate a larger number of samples. More specific study limitations can be found in the discussions of Chapters 2-4.

Future Work

Clinical dose bisphosphonate treatment

Now that the long-term structural and material changes resulting from high-dose zoledronate have been characterized, further analysis of a single injection at a clinically relevant dose would provide meaningful information for the utility in radiation therapy. Due to the extreme structural changes at six months following zoledronate administration, a less potent bisphosphonate such as alendronate could be used. A calcein label injected at the first radiation dose would provide the boundaries for localized material properties testing in new and extant bone for assessment.

Include OVX model into material characterization for drug efficacy

In addition to testing clinical bisphosphonate dosing, an OVX model should be incorporated to determine if there are additional alterations in material or structural properties that suggest a better option for a therapeutic. Chapter 2 revealed an additive effect from OVX and radiation therapy on bone loss, which could influence the clinical dose required to prevent osteoclast activation.

Validation of heterotopic ossification in hemarthrosis model

Based on microCT imaging, soft-tissues surrounding the knee joint appear to be mineralizing. Peterson et al. developed a method to verify the existence of heterotopic ossification versus cortical bone [168]. Specifically, using microCT images to guide locations for

testing, high resolution Raman spectroscopy and histologic sections in combination can be used to identify soft tissue mineralization. With heterotopic ossification, the phosphate vibrational region shifts to the right and crystallinity/mineral to matrix ratio are significantly decreased. Picrosirius red and pentachrome staining to view collagen structure can be used to confirm results.

Improve finite element model to include modulus estimates as well

Functional evaluation in this dissertation utilized finite element models from microCT images with homogeneous material properties applied for the assessment of stiffness. In order to improve upon this estimate, modulus values obtained from nanoindentation or microindentation could be applied to areas within the bone. Further assessment of material properties at multiple length scales should be performed prior to assigning modulus values. This is not a trivial task, considering the heterogeneity to be represented in bone tissue. Another option for an improved finite element model would be to scale material properties by grayscale values obtained from microCT imaging.

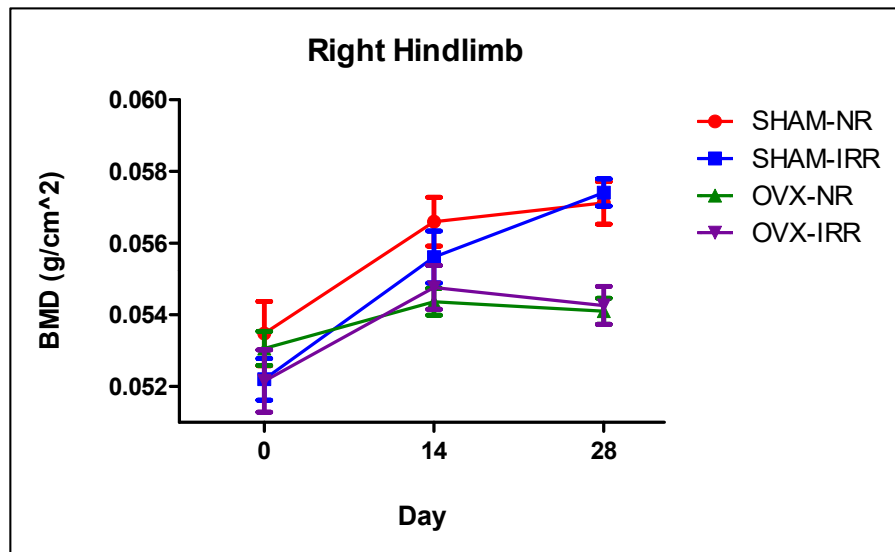


Figure 5.1: Right hindlimb DEXA data for OVX+Radiation study with four treatment group mean aBMD values plotted over time

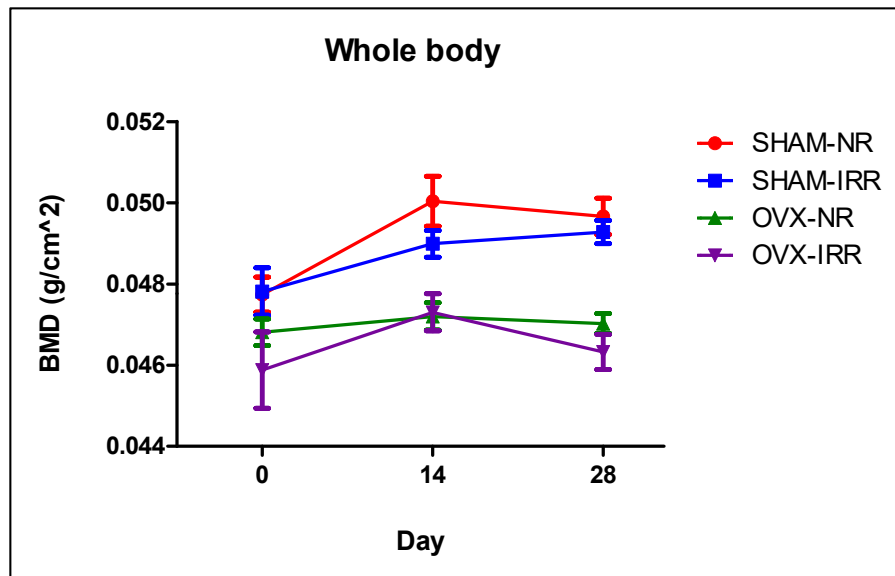


Figure 5.2: Whole body DEXA data for OVX+Radiation study with four treatment group mean aBMD values plotted over time

				Proximal Tibia Trabecular Analysis														
Mouse	Group	Rad		VOX-TV	VOX-BV	VOX-BV/TV	Conn-Dens.	TRI-SMI	DT-Tb.N	DT-Tb.Th	DT-Tb.Sp	vBMD	vBMD2	TMD				
1192	sham	NR		1.9121	0.1368	0.0715	47.3292	2.564	3.3742	0.0448	0.2963	62.0599	56.46527	789.724				
1242	sham	NR		1.928	0.2104	0.1091	80.6553	2.2461	4.0992	0.049	0.2435	98.9122	90.59446	830.38				
1291	sham	NR		2.0333	0.2126	0.1045	75.9831	1.95	4.1233	0.0437	0.2415	82.092	83.31221	797.246				
1357	sham	NR		1.7505	0.2015	0.1151	85.4062	2.1525	3.4515	0.0489	0.2903	102.6312	91.72411	796.908				
1689	sham	NR		1.9503	0.1661	0.0852	62.0433	2.3232	3.4876	0.0449	0.2862	73.6396	69.8122	819.392				
1880	sham	NR		2.1782	0.1735	0.0797	50.5014	2.3802	3.6883	0.0441	0.2698	69.667	66.15435	830.042				
6-R1	sham	NR		1.7678	0.1603	0.0907	55.1526	2.0518	3.2329	0.0469	0.3095	79.4717	73.22256	807.305				
7-R1	sham	NR		1.8218	0.1272	0.0698	42.2647	2.4424	3.603	0.0435	0.2756	56.4813	55.10501	789.47				
			MEAN	1.91775	0.17355	0.0907	62.416975	2.263775	3.6325	0.045725	0.276588	78.11936	73.29877	807.5584				
			ST DEV	0.142451	0.032501	0.017242224	16.361224	0.205361	0.325759	0.002249	0.024276	16.33754	14.22517	17.03555				
1024	sham	IRR		1.6317	0.0828	0.0508	13.4833	3.1368	2.8653	0.0498	0.3513	28.673	39.78732	783.215				
1170	sham	IRR		1.5747	0.071	0.0451	15.2411	3.2435	2.214	0.0574	0.4391	18.5302	35.73471	792.344				
1196	sham	IRR		1.289	0.0749	0.0581	18.619	3.0262	2.6372	0.0537	0.3786	44.1408	47.29729	814.067				
1427	sham	IRR		1.5864	0.0639	0.0403	16.7048	3.5461	2.681	0.0486	0.3739	19.3754	32.57183	808.234				
1492	sham	IRR		1.4772	0.0613	0.0415	11.8471	3.2242	2.5405	0.0442	0.3922	22.0802	31.82295	766.818				
1704	sham	IRR		1.6422	0.0799	0.0486	15.8321	2.8887	2.5219	0.0548	0.3991	24.1933	38.82421	798.852				
1774	sham	IRR		1.5168	0.0717	0.0473	30.656	3.0589	2.3481	0.0469	0.4193	29.8563	38.0336	804.093				
1902	sham	IRR		1.6497	0.0978	0.0593	34.2492	2.7104	2.4422	0.0463	0.4151	38.9849	46.46475	783.554				
			MEAN	1.545963	0.075413	0.048875	19.579075	3.10435	2.531275	0.050213	0.396075	28.22926	38.81708	793.8971				
			ST DEV	0.120382	0.011595	0.006991985	8.25394966	0.250656	0.202673	0.00463	0.02823	9.244825	5.724361	15.57313				
1151	ovx	NR		2.2652	0.1324	0.0584	47.8976	2.5855	3.1681	0.0394	0.3125	32.4766	44.51067	762.169				
1218	ovx	NR		2.248	0.1584	0.0705	46.2627	2.4929	3.1786	0.0465	0.3126	54.1992	54.31687	770.452				
1517	ovx	NR		2.4959	0.1341	0.0537	30.4505	2.7788	3.3976	0.0391	0.2936	40.2527	43.17072	803.924				
1707	ovx	NR		2.2694	0.177	0.078	50.8956	2.415	3.5436	0.0456	0.2815	60.7075	65.02018	833.592				
1729	ovx	NR		2.3278	0.1087	0.0467	27.2795	2.8208	3.2053	0.0372	0.3118	32.6456	37.50379	803.079				
1856	ovx	NR		1.8214	0.0892	0.049	29.9219	2.4604	2.2931	0.0421	0.4372	31.7159	39.22244	800.458				
2-R2	ovx	NR		2.4342	0.1257	0.0516	25.6754	2.7891	3.2612	0.0389	0.3053	37.8016	41.5784	805.783				
2035 (femur only)	ovx	NR																
			MEAN	2.265986	0.132214	0.058271429	36.9118857	2.620357	3.149643	0.041257	0.322071	41.39987	46.47472	797.0653				
			ST DEV	0.217167	0.029271	0.011719174	10.9035069	0.172711	0.401471	0.003586	0.052089	11.55359	9.80862	23.91281				
1055	ovx	IRR		1.6741	0.0479	0.0286	5.0775	2.8711	2.58	0.0505	0.4222	-0.5722	22.6973	793.612				
1069	ovx	IRR		1.7034	0.0557	0.0327	5.8706	3.0055	1.9488	0.0496	0.5305	4.3302	25.66917	784.99				
1394	ovx	IRR		1.9143	0.1069	0.0558	23.5068	2.8932	2.2283	0.0555	0.4618	28.2504	43.45816	778.82				
1535	ovx	IRR		1.8937	0.0815	0.043	12.6739	2.5807	2.1907	0.0527	0.4591	16.079	34.62326	805.192				
1594	ovx	IRR		1.8273	0.0652	0.0357	4.6517	2.7395	2.16	0.0535	0.4591	8.7254	28.88416	809.08				
1748	ovx	IRR		1.5211	0.0444	0.0292	8.5462	2.9646	1.5747	0.0516	0.6409	0.0195	23.09203	790.823				
1809	ovx	IRR		1.5471	0.0395	0.0255	3.8783	3.6293	2.0227	0.0498	0.5056	-4.5448	20.3923	799.698				
2-R1	ovx	IRR		1.5503	0.0371	0.0239	4.5153	3.0552	1.7606	0.045	0.5611	1.1183	18.94713	792.767				
			MEAN	1.703913	0.059775	0.0343	8.5900375	2.967388	2.058225	0.051025	0.505038	6.675725	27.22044	794.3728				
			ST DEV	0.159465	0.024028	0.01060027	6.68940929	0.307881	0.30815	0.003149	0.070915	10.80485	8.248057	10.05272				

Table 5.1: OVX+Radiation study proximal tibia trabecular microCT raw data

Mouse	Group	Rad	Proximal Tibia Cortical Analysis						
			VOX-TV	VOX-BV	VOX-BV/T Ct. Po	DT-Ct.Th	vBMD	TMD	
1192 sham	NR		0.9332	0.8661	0.9281	0.0719	0.1149	718.2172	846.8622
1242 sham	NR		1.0851	1.017	0.9373	0.0627	0.1318	753.041	871.7122
1291 sham	NR		0.793	0.7062	0.8905	0.1095	0.0915	649.584	798.6838
1357 sham	NR		1.0615	0.985	0.9279	0.0721	0.1248	723.1196	847.0313
1689 sham	NR		0.9832	0.9164	0.932	0.068	0.1204	738.5029	864.6122
1880 sham	NR		0.9779	0.9064	0.9269	0.0731	0.11	737.9113	873.2337
6-R1 sham	NR		1.0197	0.9466	0.9283	0.0717	0.1228	727.5994	850.8349
7-R1 sham	NR		0.9248	0.8662	0.9367	0.0633	0.116	703.172	820.2373
			0.9723	0.901238	0.925963	0.074038	0.116525	718.8934	846.651
			0.091816	0.095044	0.014893	0.014893	0.012118	31.75203	25.83889
1024 sham	IRR		1.1416	1.0724	0.9393	0.0607	0.1579	760.6481	870.0218
1170 sham	IRR		1.1372	1.0863	0.9552	0.0448	0.1671	791.1611	890.3919
1196 sham	IRR		1.0163	0.9668	0.9513	0.0487	0.1584	770.8755	867.8242
1427 sham	IRR		1.11	1.0469	0.9431	0.0569	0.1502	760.31	866.6408
1492 sham	IRR		1.1568	1.1069	0.9569	0.0431	0.1664	791.4147	887.6872
1704 sham	IRR		1.1012	1.0532	0.9564	0.0436	0.1545	781.2719	879.5729
1774 sham	IRR		1.09	1.036	0.9504	0.0496	0.1699	802.6564	906.7896
1902 sham	IRR		1.0387	0.9884	0.9516	0.0484	0.1436	760.6481	861.8229
			1.098975	1.044613	0.950525	0.049475	0.1585	777.3732	878.8439
			0.046499	0.044381	0.005915	0.005915	0.008468	15.55049	14.27825
1151 ovx	NR		0.9145	0.7981	0.8727	0.1273	0.0987	617.465	768.5933
1218 ovx	NR		0.9115	0.7978	0.8753	0.1247	0.0969	627.6923	790.3159
1517 ovx	NR		0.9191	0.8481	0.9227	0.0773	0.1026	700.9744	838.8325
1707 ovx	NR		0.9272	0.8043	0.8675	0.1325	0.0966	651.7816	827.4218
1729 ovx	NR		0.9027	0.8449	0.936	0.064	0.1091	719.0624	849.9051
1856 ovx	NR		0.8525	0.8005	0.939	0.061	0.1066	710.6946	833.9301
2-R2 ovx	NR		0.9053	0.8428	0.931	0.069	0.1056	712.3005	845.5944
2035 (femur only) ovx	NR								
			0.904686	0.8195	0.906314	0.093686	0.1023	677.1387	822.0847
			0.024444	0.024245	0.032726	0.032726	0.005005	43.46832	30.67723
1055 ovx	IRR		0.9651	0.9027	0.9354	0.0646	0.1348	740.8696	861.4848
1069 ovx	IRR		1.004	0.9251	0.9214	0.0786	0.1342	716.9493	841.6218
1394 ovx	IRR		1.0692	0.9459	0.8846	0.1154	0.124	675.8708	829.1968
1535 ovx	IRR		1.0299	0.9709	0.9427	0.0573	0.1324	756.2529	876.6146
1594 ovx	IRR		1.0174	0.9604	0.944	0.056	0.1364	760.9862	881.348
1748 ovx	IRR		1.0309	0.9781	0.9488	0.0512	0.1503	764.8743	867.6551
1809 ovx	IRR		0.9675	0.9023	0.9326	0.0674	0.1402	742.9827	862.5837
2-R1 ovx	IRR		0.9394	0.8794	0.936	0.064	0.1343	756.4219	881.1789
			1.002925	0.9331	0.930688	0.069313	0.135825	739.401	862.7105
			0.042819	0.03622	0.020403	0.020403	0.007431	29.86555	18.80589

Table 5.2: OVX+Radiation study proximal tibia cortical microCT raw data.
Mean and standard deviation highlighted in gray (mean on top)

			Midshaft Femur Cortical Analysis										
Mouse	Group	Rad	VOX-TV	VOX-BV	VOX-BV/TV	Ct. Po	DT-Cort.Th	Vbmd	TMD	M.Ar	T.Ar	BA/TA	Cort. Ar
	1192 sham	NR	0.3478	0.3112	0.8947	10.53	0.1695	991.4822	1037.2097	0.856	1.5438	0.445524	0.6878
	1242 sham	NR	0.3792	0.3425	0.9033	9.67	0.1992	994.5251	1036.5334	0.7392	1.4884	0.503359	0.7492
	1291 sham	NR	0.3134	0.2693	0.8591	14.09	0.1656	949.7276	995.9621	0.726	1.346	0.460624	0.62
	1357 sham	NR	0.3687	0.3342	0.9066	9.34	0.1875	1012.1906	1058.3406	0.7826	1.5112	0.482133	0.7286
	1689 sham	NR	0.3686	0.3377	0.9162	8.38	0.1785	1028.4192	1074.4846	0.8616	1.5902	0.458181	0.7286
	1880 sham	NR	0.3645	0.3312	0.9087	9.13	0.1836	1027.1514	1076.006	0.8042	1.5244	0.472448	0.7202
	6-R1 sham	NR	0.357	0.3294	0.9228	7.72	0.1839	1036.618	1081.5846	0.7594	1.4648	0.481567	0.7054
	7-R1 sham	NR	0.3383	0.3102	0.917	8.3	0.1779	1023.1786	1067.2156	0.7218	1.3904	0.480869	0.6686
			0.354688	0.320713	0.90355	9.645	0.1807125	1007.911588	1053.417075	0.78135	1.4824	0.473088	0.70105
			0.021088	0.023829	0.020005356	2.000535643	0.010510327	28.53739781	28.81210469	0.055297404	0.080533	0.018001	0.041438
	1024 sham	IRR	0.3678	0.3375	0.9176	8.24	0.1878	1032.3073	1077.9501	0.785	1.512	0.48082	0.727
	1170 sham	IRR	0.3478	0.3123	0.898	10.2	0.1755	1002.5549	1052.3394	0.8244	1.512	0.454762	0.6876
	1196 sham	IRR	0.3229	0.2875	0.8904	10.96	0.1691	978.6347	1023.6013	0.7764	1.415	0.451307	0.6386
	1427 sham	IRR	0.3451	0.3023	0.876	12.4	0.1693	962.6597	1008.218	0.8726	1.555	0.438842	0.6824
	1492 sham	IRR	0.3388	0.2996	0.8843	11.57	0.1733	978.2121	1025.6299	0.7974	1.4668	0.456368	0.6694
	1704 sham	IRR	0.3503	0.3201	0.9137	8.63	0.1794	1026.3906	1072.9631	0.773	1.4654	0.472499	0.6924
	1774 sham	IRR	0.3461	0.3134	0.9054	9.46	0.1738	1027.9966	1080.4858	0.82	1.5042	0.45486	0.6842
	1902 sham	IRR	0.3219	0.2905	0.9024	9.76	0.1672	1005.8513	1054.0299	0.801	1.4376	0.442821	0.6366
			0.342588	0.3079	0.898475	10.1525	0.174425	1001.8259	1049.402188	0.806225	1.4835	0.456535	0.677275
			0.01498	0.016448	0.014304919	1.430491923	0.006689811	26.3591014	27.49877546	0.032677723	0.045624	0.014036	0.029506
	1151 ovx	NR	0.3433	0.2999	0.8736	12.64	0.1629	957.4193	1002.893	0.9784	1.6572	0.409607	0.6788
	1218 ovx	NR	0.3533	0.3223	0.9122	8.78	0.1712	1016.5859	1062.7358	0.89	1.5886	0.439758	0.6986
	1517 ovx	NR	0.3368	0.2999	0.8904	10.96	0.1719	997.0609	1047.7751	0.7886	1.4546	0.457858	0.666
	1707 ovx	NR	0.3532	0.3227	0.9137	8.63	0.1757	1015.8251	1060.7073	0.8414	1.5396	0.453494	0.6982
	1729 ovx	NR	0.3386	0.3067	0.9056	9.44	0.1701	1000.8644	1045.8311	0.8192	1.489	0.449832	0.6698
	1856 ovx	NR	0.3335	0.3001	0.8999	10.01	0.1649	989.3692	1034.843	0.8602	1.5196	0.43393	0.6594
	2-R2 ovx	NR	0.3473	0.3163	0.9108	8.92	0.1718	1010.7537	1055.7203	0.839	1.5256	0.450052	0.6866
2035 (femur only)	ovx	NR	0.3406	0.3036	0.8913	10.87	0.1735	968.9145	1010.162	0.8158	1.4892	0.452189	0.6734
			0.343325	0.308938	0.8996875	10.03125	0.17025	994.599125	1040.08345	0.854075	1.532925	0.44334	0.67885
			0.007384	0.009979	0.013879938	1.387993799	0.004292186	21.74408312	22.61815088	0.0587257	0.064138	0.015669	0.014539
	1055 ovx	IRR	0.3399	0.3049	0.8969	10.31	0.1722	993.9335	1040.0835	0.8062	1.4782	0.454607	0.672
	1069 ovx	IRR	0.3386	0.2837	0.8378	16.22	0.1637	937.1336	987.9323	0.915	1.5848	0.42264	0.6698
	1394 ovx	IRR	0.3361	0.2913	0.8669	13.31	0.174	970.8585	1024.9537	0.7724	1.437	0.462491	0.6646
	1535 ovx	IRR	0.3455	0.3083	0.8924	10.76	0.1676	990.637	1039.0692	0.9026	1.5858	0.430824	0.6832
	1594 ovx	IRR	0.3528	0.3164	0.8971	10.29	0.1707	996.131	1045.0703	0.8896	1.5868	0.439375	0.6972
	1748 ovx	IRR	0.3544	0.3173	0.8953	10.47	0.1763	993.8489	1041.5204	0.8402	1.541	0.45477	0.7008
	1809 ovx	IRR	0.33	0.2986	0.905	9.5	0.1654	1008.4715	1055.2977	0.8472	1.4998	0.435125	0.6526
	2-R1 ovx	IRR	0.3322	0.2976	0.8957	10.43	0.1681	988.1014	1035.0966	0.846	1.5028	0.437051	0.6568
			0.341188	0.302263	0.8858875	11.41125	0.16975	984.889425	1033.627963	0.8524	1.527025	0.44211	0.674625
			0.009009	0.011767	0.022400602	2.240060187	0.004321706	21.926474	20.352499	0.048659047	0.05654	0.013733	0.017735

Table 5.3: OVX+Radiation study midshaft femur cortical microCT raw data. Mean and standard deviation highlighted in gray (mean on top)

Proximal Tibia Finite Element Analysis							
Mouse	Group	Rad	Whole Bone Stiffness	Whole Bone Cross-Sectional Area	Cortical Bone Stiffness	Cortical Bone Cross-Sectional Area	Trabecular Bone Stiffness
1192 sham	NR		6.72E+03	3.62E+00	5.23E+03	3.34E+00	1.50E+03
1242 sham	NR		8.87E+03	3.75E+00	6.91E+03	3.21E+00	1.96E+03
1291 sham	NR		6.44E+03	3.36E+00	4.13E+03	2.91E+00	2.31E+03
1357 sham	NR		8.17E+03	3.73E+00	5.99E+03	3.33E+00	2.18E+03
1689 sham	NR		7.69E+03	3.71E+00	6.07E+03	3.25E+00	1.62E+03
1880 sham	NR		7.45E+03	3.74E+00	5.67E+03	3.30E+00	1.78E+03
6-R1 sham	NR		7.63E+03	3.65E+00	5.74E+03	3.32E+00	1.90E+03
7-R1 sham	NR		6.99E+03	3.39E+00	5.62E+03	3.06E+00	1.37E+03
			7494.45	3.6185375	5668.35	3.216425	1826.1
			791.7843447	0.157079552	790.9627804	0.154510561	325.4570325
1024 sham	IRR		8.43E+03	3.37E+00	7.34E+03	3.16E+00	1.10E+03
1170 sham	IRR		8.87E+03	3.14E+00	7.93E+03	2.97E+00	9.38E+02
1196 sham	IRR		7.77E+03	2.93E+00	6.65E+03	2.72E+00	1.12E+03
1427 sham	IRR		8.37E+03	3.02E+00	7.41E+03	2.89E+00	9.61E+02
1492 sham	IRR		8.40E+03	3.31E+00	7.81E+03	3.16E+00	5.92E+02
1704 sham	IRR		8.59E+03	3.17E+00	7.49E+03	3.06E+00	1.10E+03
1774 sham	IRR		8.37E+03	3.12E+00	7.47E+03	2.95E+00	9.00E+02
1902 sham	IRR		7.43E+03	3.38E+00	6.40E+03	3.15E+00	1.03E+03
			8279.5	3.1798875	7313.2875	3.0069125	966.2125
			459.7793819	0.162786525	530.7088694	0.157760392	171.2523988
1151 ovx	NR		5.88E+03	3.62E+00	4.56E+03	3.29E+00	1.32E+03
1218 ovx	NR		5.57E+03	3.83E+00	4.12E+03	3.50E+00	1.45E+03
1517 ovx	NR		6.43E+03	3.95E+00	4.85E+03	3.54E+00	1.58E+03
1707 ovx	NR		5.61E+03	4.06E+00	3.91E+03	3.71E+00	1.70E+03
1729 ovx	NR		6.61E+03	3.68E+00	5.45E+03	3.19E+00	1.16E+03
1856 ovx	NR		6.64E+03	3.19E+00	5.08E+03	3.05E+00	1.55E+03
2-R2 ovx	NR		6.49E+03	3.83E+00	5.15E+03	3.34E+00	1.34E+03
2035 (femur only) ovx	NR		6174.542857	3.7353	4732.271429	3.373514286	1442.271429
			472.6647891	0.28146895	563.9018523	0.223935098	185.1585511
1055 ovx	IRR		6.96E+03	2.90E+00	6.19E+03	2.83E+00	7.64E+02
1069 ovx	IRR		7.16E+03	3.02E+00	6.42E+03	2.85E+00	7.39E+02
1394 ovx	IRR		6.57E+03	3.78E+00	5.02E+03	3.58E+00	1.55E+03
1535 ovx	IRR		7.41E+03	3.30E+00	6.35E+03	3.14E+00	1.06E+03
1594 ovx	IRR		7.55E+03	3.04E+00	6.73E+03	2.92E+00	8.21E+02
1748 ovx	IRR		7.68E+03	2.94E+00	6.99E+03	2.86E+00	6.93E+02
1809 ovx	IRR		6.77E+03	2.85E+00	6.07E+03	2.80E+00	7.02E+02
2-R1 ovx	IRR		6.87E+03	2.69E+00	6.26E+03	2.64E+00	6.08E+02
			7120.0375	3.0664875	6252.7375	2.953275	867.3
			396.5112967	0.338720822	581.9309236	0.290456959	307.2916344

Table 5.4: OVX+Radiation study proximal tibia finite element analysis raw data. Mean and standard deviation highlighted in gray (mean on top)

			Femoral Neck Finite Element Analysis
Mouse	Group	Rad	Stiffness (N/mm)
1192	sham	NR	1233.628
1242	sham	NR	1299.3
1291	sham	NR	1106.582
1357	sham	NR	1287.568
1689	sham	NR	1406.25
1880	sham	NR	1321.926
6-R1	sham	NR	1439.064
7-R1	sham	NR	1263.992
			1294.78875
			102.9276701
1024	sham	IRR	1218.698
1170	sham	IRR	1423.072
1196	sham	IRR	1324.214
1427	sham	IRR	1271.084
1492	sham	IRR	1153.518
1704	sham	IRR	1169.728
1774	sham	IRR	1041.07
1902	sham	IRR	1080.422
			1210.22575
			126.711636
1151	ovx	NR	1096.432
1218	ovx	NR	1173.608
1517	ovx	NR	1253.492
1707	ovx	NR	1257.446
1729	ovx	NR	1389.626
1856	ovx	NR	1098.82
2-R2	ovx	NR	1126.878
2035 (femur only)	ovx	NR	1019.486
			1176.9735
			118.0012657
1055	ovx	IRR	1032.696
1069	ovx	IRR	1192.654
1394	ovx	IRR	1171.5
1535	ovx	IRR	1274.566
1594	ovx	IRR	1261.6
1748	ovx	IRR	1396.244
1809	ovx	IRR	1230.68
2-R1	ovx	IRR	1178.504
			1217.3055
			104.0128397

Table 5.5: OVX+Radiation study femoral neck finite element analysis raw data. Mean and standard deviation (mean on top)

		L1 Vertebrae Trabecular Analysis										L1 Vertebrae Finite Element Analysis	
Mouse	Group	Rad	VOX-TV	VOX-BV	VOX-BV/TV	Conn-Dens.	DT-Tb.N	DT-Tb.Th	DT-Tb.Sp	vBMD		Stiffness (N/mm)	
1192 sham	NR		1.5675	0.3738	0.2385	184.3726	4.6458	0.0467	0.2026	199.6788		2462.093333	
1242 sham	NR		1.8685	0.4803	0.257	237.3532	4.7968	0.0485	0.1976	214.3899		2872.133333	
1291 sham	NR		1.6329	0.4701	0.2879	227.1979	5.3789	0.0483	0.1695	236.639		2958.213333	
1357 sham	NR		1.4579	0.3827	0.2625	188.9743	4.9757	0.0501	0.1872	222.5763		2841.08	
1689 sham	NR		1.6612	0.3695	0.2224	171.8664	4.5709	0.0474	0.2044	190.8034		2774.186667	
1880 sham	NR		1.7331	0.3814	0.2201	201.9454	4.306	0.0465	0.2222	182.2523		2837.626667	
6-R1 sham	NR		1.4541	0.3266	0.2246	167.4573	4.3543	0.0487	0.2202	190.4387		2686.106667	
7-R1 sham	NR		1.5425	0.3189	0.2067	177.6362	4.1884	0.0455	0.2315	177.6323		2554.026667	
			1.6147125	0.3879125	0.2399625	194.6004125	4.6521	0.0477125	0.2044	201.8013375		2748.183333	
			0.1407864	0.0590641	0.02710751	25.69595729	0.393521	0.0014701	0.020228	20.78670684		169.1069354	
1024 sham	IRR		1.4617	0.3057	0.2091	172.3987	4.4524	0.0452	0.2163	178.3618		2513.92	
1170 sham	IRR		1.78	0.3363	0.189	163.2038	4.2203	0.0437	0.2249	156.9232		2545.346667	
1196 sham	IRR		1.6447	0.4467	0.2716	186.6553	4.9115	0.0499	0.1894	231.1679		3088.226667	
1427 sham	IRR		1.6241	0.3011	0.1854	171.4806	4.3133	0.043	0.2201	150.52		2458.666667	
1492 sham	IRR		1.2674	0.2765	0.2182	174.3763	4.4281	0.0471	0.2134	189.2634		2440.306667	
1704 sham	IRR		1.6945	0.3709	0.2189	190.6157	4.5724	0.0459	0.2079	177.4702		2468.72	
1774 sham	IRR		1.4544	0.2808	0.1931	164.6782	4.2991	0.044	0.2232	156.7206		2380.506667	
1902 sham	IRR		1.5738	0.4165	0.2646	214.7666	5.1878	0.047	0.1796	218.1184		2766.853333	
			1.562575	0.3418125	0.2187375	179.7719	4.548113	0.045725	0.20935	182.3181875		2582.818333	
			0.1622782	0.0637024	0.03304542	17.08860177	0.335944	0.0022601	0.016471	29.43906101		234.5601423	
1151 ovx	NR		1.6942	0.3166	0.1869	199.7956	4.509	0.0407	0.2145	156.4774		2502.853333	
1218 ovx	NR		1.7661	0.2723	0.1542	179.2046	3.7814	0.0394	0.2582	125.434		2266.96	
1517 ovx	NR		1.7151	0.3248	0.1894	183.0833	4.3793	0.0421	0.2204	159.5169		2405.706667	
1707 ovx	NR		1.6282	0.2843	0.1746	155.0833	4.2529	0.0418	0.2295	144.1978		2423.893333	
1729 ovx	NR		1.8794	0.3122	0.1661	179.5766	4.2772	0.0402	0.2239	134.7957		2385.546667	
1856 ovx	NR		1.7578	0.2889	0.1644	163.838	3.9078	0.0424	0.2505	133.4178		2220.786667	
2-R2 ovx	NR		1.8386	0.2888	0.1571	116.6637	3.9457	0.0419	0.2432	134.593		2376.626667	
2035 (femur only) ovx	NR		1.6719	0.284	0.1699	177.6418	3.9911	0.0417	0.2432	143.671		2369.453333	
			1.7542	0.2982714	0.17038571	168.1778714	4.150471	0.0412143	0.234314	141.2046571		2368.978333	
			0.0855938	0.0194977	0.01381249	26.82469155	0.27218	0.0011246	0.016479	12.72590095		88.63156969	
1055 ovx	IRR		1.5918	0.2383	0.1497	136.949	4.0659	0.0385	0.2383	122.0703		2312.16	
1069 ovx	IRR		1.9804	0.2615	0.132	145.4215	3.7702	0.0382	0.2616	103.5091		2166.213333	
1394 ovx	IRR		1.7981	0.2503	0.1392	159.335	3.946	0.0382	0.2443	117.2071		2070.826667	
1535 ovx	IRR		1.7702	0.3247	0.1834	138.9707	4.266	0.0423	0.2247	157.2069		2510.733333	
1594 ovx	IRR		1.593	0.3162	0.1985	160.7024	4.5101	0.0442	0.2093	169.1622		2507.266667	
1748 ovx	IRR		1.7305	0.2738	0.1582	150.5346	3.9563	0.0412	0.2443	129.1219		2166.213333	
1809 ovx	IRR		1.6589	0.2717	0.1638	156.7304	3.8553	0.0412	0.2533	139.2941		2265.04	
2-R1 ovx	IRR		1.6774	0.2932	0.1748	181.2352	4.3001	0.0409	0.2251	145.6163		2331.213333	
			1.7250375	0.2787125	0.16245	153.73485	4.083738	0.0405875	0.237613	135.3984875		2291.208333	
			0.1278656	0.0305662	0.02249203	14.26408716	0.252936	0.0021577	0.017056	21.71263744		159.1998574	

Table 5.6: OVX+Radiation study L1 Vertebra trabecular microCT analysis and finite element analysis raw data. Mean and standard deviation highlighted in gray (mean on top)

Chapter 3

Bone	Rad	Treatment	VOX-TV	VOX-BV	VOX-BV/TV	Conn-Dens.	TRI-SMI	DT-Tb.N	DT-Tb.Th	DT-Tb.Sp	vBMD
5145	NR	PLAC	1.9321	0.1477	0.0765	45.2875	2.4317	3.194	0.0478	0.3106	83.0432
5146	NR	PLAC	1.8704	0.1908	0.102	62.8212	2.2072	3.4542	0.0534	0.2885	105.576
5147	NR	PLAC	1.727	0.1709	0.099	50.0861	2.4212	2.7904	0.056	0.3644	105.9002
5150	NR	PLAC	1.8517	0.1129	0.061	27.8124	2.9027	3.0522	0.0472	0.3282	73.8436
5151	NR	PLAC	2.2577	0.1391	0.0616	29.2335	2.6184	2.71	0.0536	0.3732	73.8031
5152	NR	PLAC	1.6984	0.1435	0.0845	50.9298	2.4227	3.143	0.0473	0.3173	96.0522
5156	NR	PLAC	2.1128	0.1769	0.0837	43.5433	2.2261	2.8133	0.0529	0.3605	89.568
5160	NR	PLAC	2.0033	0.1888	0.0942	46.1728	2.19	3.485	0.0469	0.2881	105.4139
5164	NR	PLAC	1.8189	0.1467	0.0806	39.8586	2.2507	3.078	0.0467	0.3312	87.1769
5166	NR	PLAC	1.6568	0.078	0.0471	13.8825	3.4626	2.8724	0.0485	0.3533	61.8883
				MEAN	0.07902	40.96277	2.51333	3.05925	0.05003	0.33153	88.22654
				ST DEV	0.01784363	13.975943	0.39956	0.26925	0.003522	0.030767	15.30571
5148	NR	ZOL	1.8366	0.1319	0.0718	42.1974	2.5483	3.3947	0.0465	0.2929	79.031
5149	NR	ZOL	1.9864	0.141	0.071	31.4636	2.5537	3.0511	0.0471	0.3271	73.3573
5154	NR	ZOL	1.8595	0.118	0.0635	33.0737	2.7553	2.96	0.0472	0.3365	68.0078
5158	NR	ZOL	1.9097	0.1727	0.0904	43.7248	2.5965	3.4905	0.0482	0.2858	101.2802
5161	NR	ZOL	1.6054	0.1402	0.0873	75.6822	2.2445	3.9038	0.0401	0.2554	96.5791
5163	NR	ZOL	2.0528	0.1759	0.0857	51.6362	2.3286	3.3096	0.0496	0.3003	92.6885
5167	NR	ZOL	1.7707	0.1199	0.0677	45.7455	2.8593	3.0787	0.0451	0.3194	79.9226
5170	NR	ZOL	2.0258	0.1527	0.0754	33.8145	2.562	3.0653	0.045	0.3233	79.1931
5172	NR	ZOL	2.0623	0.2083	0.101	94.7983	1.9555	4.0464	0.0401	0.2431	101.6044
5173	NR	ZOL	2.0157	0.1855	0.092	52.3403	2.1302	3.3377	0.0471	0.2972	91.5943
				MEAN	0.08058	50.44765	2.45339	3.36378	0.0456	0.2981	86.32583
				ST DEV	0.01233115	20.2293543	0.28261	0.36657	0.003193	0.030617	11.92226
5142	IRR	PLAC	2.1017	0.1886	0.0898	54.7166	2.4923	3.5681	0.0485	0.2779	94.958
5143	IRR	PLAC	2.0666	0.1387	0.0671	28.549	2.585	2.6869	0.052	0.3726	76.0321
5144	IRR	PLAC	1.7137	0.1521	0.0888	63.606	2.4278	3.2256	0.047	0.3108	96.8627
5153	IRR	PLAC	1.8614	0.1443	0.0775	26.5935	2.7959	3.2958	0.0547	0.3004	90.0543
5157	IRR	PLAC	1.8966	0.15	0.0791	37.436	2.6318	3.2394	0.0502	0.3067	82.4758
5165	IRR	PLAC	1.817	0.1282	0.0705	25.317	2.8057	3.0699	0.0524	0.3234	77.5316
5169	IRR	PLAC	1.9727	0.1675	0.0849	47.3965	2.3361	3.4478	0.0465	0.2868	88.19
5171	IRR	PLAC	1.8123	0.1752	0.0967	30.6236	2.3252	2.8189	0.0656	0.3477	91.5132
5174	IRR	PLAC	1.8341	0.1948	0.1062	31.3513	2.2661	2.7741	0.0587	0.3594	107.0755
5179	IRR	PLAC	1.9807	0.2009	0.1014	55.0305	2.4166	3.9162	0.0492	0.2496	105.9812
				MEAN	0.0862	40.062	2.50825	3.20427	0.05248	0.31353	91.06744
				ST DEV	0.01291037	13.9449249	0.19128	0.38411	0.005903	0.038233	10.64582
5155	IRR	ZOL	1.9089	0.18	0.0943	56.0541	2.2677	3.4976	0.0492	0.2821	96.417
5159	IRR	ZOL	1.9694	0.1592	0.0809	31.7351	2.9535	3.1198	0.0584	0.3198	82.0705
5162	IRR	ZOL	1.9745	0.1706	0.0864	26.8417	2.7923	3.0132	0.0603	0.3338	92.5669
5168	IRR	ZOL	2.3978	0.1556	0.0649	23.7721	2.7168	3.1016	0.0494	0.3202	66.5083
5175	IRR	ZOL	1.8422	0.1516	0.0823	41.5267	2.6742	3.471	0.051	0.2854	86.5285
5176	IRR	ZOL	2.0204	0.1405	0.0695	29.6964	2.7121	3.337	0.0479	0.298	74.1678
5177	IRR	ZOL	1.8393	0.2	0.1087	77.4768	2.0548	3.6059	0.0508	0.275	114.046
5178	IRR	ZOL	2.0117	0.1644	0.0817	48.2184	2.363	3.5887	0.0457	0.2763	85.5964
5181	IRR	ZOL	1.7164	0.1661	0.0968	60.884	2.4173	3.2887	0.0518	0.3008	102.2933
5180	IRR	ZOL	1.8901	0.1325	0.0701	57.141	2.8167	3.1208	0.0471	0.332	74.1273
				MEAN	0.08356	45.33463	2.57684	3.31443	0.05116	0.30234	87.4322
				ST DEV	0.01362149	17.6019206	0.28528	0.21879	0.004719	0.022698	14.3757

Table 5.7: Radiation+Zoledronate study 3 day proximal tibia trabecular microCT raw data

Bone	Rad	Treatment		VOX-TV	VOX-BV	VOX-BV/TV	Conn-Dens.	TRI-SMI	DT-Tb.N	DT-Tb.Th	DT-Tb.Sp	vBMD
5233	NR	PLAC		2.1794	0.185	0.0849	45.4244	2.5145	2.947	0.054	0.3407	95.5254
5234	NR	PLAC		1.9925	0.1544	0.0775	39.6483	2.3588	2.9515	0.0466	0.3388	88.109
5235	NR	PLAC		1.724	0.1591	0.0923	53.0737	2.4115	2.7741	0.0513	0.3622	103.8333
5236	NR	PLAC		2.049	0.1466	0.0715	29.2822	2.4777	2.6431	0.0535	0.3782	79.7605
5237	NR	PLAC		2.0043	0.1881	0.0939	49.1453	2.5153	3.3225	0.0527	0.3076	98.3622
5238	NR	PLAC		2.295	0.1249	0.0544	13.9434	2.8352	2.7819	0.0558	0.3611	67.2378
5239	NR	PLAC		2.1155	0.1706	0.0806	50.1058	2.1283	3.451	0.044	0.2876	88.5548
5240	NR	PLAC		1.9976	0.1704	0.0853	55.8175	2.4548	3.3527	0.0495	0.296	94.877
5243	NR	PLAC		1.9749	0.1576	0.0798	54.687	2.3353	3.2738	0.0484	0.3081	87.5011
5244	NR	PLAC		2.3216	0.1683	0.0725	39.4124	2.3821	2.9478	0.0465	0.3382	80.5305
			MEAN	2.06538	0.1625	0.07927	43.054	2.44135	3.04454	0.05023	0.33185	88.42916
			ST DEV	0.17401	0.01853	0.01145901	13.1361595	0.17886	0.283	0.003844	0.030709	10.62216
5241	NR	ZOL		2.076	0.1945	0.0937	55.1548	2.4108	3.469	0.0508	0.2816	104.9681
5242	NR	ZOL		1.8884	0.1411	0.0747	27.8017	2.6117	3.0073	0.049	0.3313	86.8121
5245	NR	ZOL		1.7602	0.1787	0.1015	62.4915	2.4727	3.7969	0.0483	0.2592	119.8008
5246	NR	ZOL		2.0132	0.2317	0.1151	69.5421	2.4178	4.1226	0.0525	0.2352	132.0399
5247	NR	ZOL		1.9295	0.1944	0.1007	58.3051	2.348	3.6577	0.0495	0.2706	113.8434
5248	NR	ZOL		1.7526	0.2381	0.1358	99.28	1.867	4.1689	0.0457	0.2331	147.1158
5251	NR	ZOL		1.846	0.2523	0.1367	63.6496	1.9123	3.8154	0.0537	0.2567	146.2242
5252	NR	ZOL		2.2581	0.239	0.1059	77.4996	2.264	3.827	0.0482	0.2541	118.1392
5266	NR	ZOL		2.08	0.1663	0.08	30.7697	2.4245	2.8442	0.0482	0.3535	93.0127
5267	NR	ZOL		1.9247	0.1843	0.0958	61.4387	2.3372	3.7365	0.0475	0.2634	114.3297
			MEAN	1.95287	0.20204	0.10399	60.59328	2.3066	3.64455	0.04934	0.27387	117.6286
			ST DEV	0.15715	0.03657	0.02063522	20.7519019	0.23828	0.43144	0.002394	0.039268	20.11347
5249	IRR	PLAC		2.1701	0.1187	0.0547	21.8886	2.9859	2.5731	0.0513	0.3864	56.2551
5250	IRR	PLAC		1.9007	0.1098	0.0578	19.9923	3.1214	2.2448	0.058	0.4467	58.1598
5254	IRR	PLAC		1.9452	0.1087	0.0559	25.4469	2.8782	2.8097	0.0452	0.3567	61.6857
5255	IRR	PLAC		2.1934	0.104	0.0474	8.2064	3.0479	1.9703	0.053	0.5207	48.7982
5256	IRR	PLAC		1.8661	0.1057	0.0567	29.4737	2.9227	2.3027	0.0533	0.4457	58.0383
5265	IRR	PLAC		1.8977	0.0878	0.0462	13.7007	3.0439	2.1021	0.049	0.4793	44.1376
5269	IRR	PLAC		1.9721	0.0801	0.0406	10.9022	2.9397	3.3748	0.043	0.2914	35.5865
5270	IRR	PLAC		1.8939	0.0918	0.0485	14.52	2.9783	2.3342	0.0476	0.4385	52.4861
5271	IRR	PLAC		1.7215	0.0609	0.0354	5.2281	2.9358	2.178	0.0451	0.4658	41.1387
5272	IRR	PLAC		1.761	0.0877	0.0498	17.3193	2.878	2.1725	0.0523	0.4691	49.3656
			MEAN	1.93217	0.09552	0.0493	16.66782	2.97318	2.40622	0.04978	0.43003	50.56516
			ST DEV	0.15213	0.0172	0.00732378	7.66607297	0.0788	0.41633	0.004633	0.067122	8.382198
5253	IRR	ZOL		1.671	0.1363	0.0816	38.0007	2.8723	3.0419	0.0514	0.326	93.418
5257	IRR	ZOL		1.6073	0.2543	0.1582	78.3939	1.9898	3.6303	0.0586	0.273	154.0863
5258	IRR	ZOL		1.8989	0.1351	0.0712	30.8069	3.2155	2.9614	0.0536	0.3319	74.1273
5259	IRR	ZOL		1.8458	0.1424	0.0771	29.5261	2.9221	3.1211	0.0513	0.3212	80.4495
5260	IRR	ZOL		2.0089	0.2092	0.1042	56.2506	2.6028	3.7271	0.0538	0.2615	102.2528
5261	IRR	ZOL		1.4209	0.1426	0.1004	56.656	2.3794	2.8561	0.051	0.3493	110.3176
5262	IRR	ZOL		1.6148	0.2106	0.1304	65.3343	2.1533	3.4217	0.0529	0.2924	138.2404
5263	IRR	ZOL		1.6789	0.2123	0.1264	62.5392	2.4883	3.5552	0.0606	0.2765	131.8372
5264	IRR	ZOL		1.8807	0.1983	0.1055	67.5272	2.5518	3.8235	0.0526	0.2525	109.2639
5268	IRR	ZOL		1.6598	0.1869	0.1126	51.8122	2.7017	3.3103	0.0603	0.3055	120.4492
			MEAN	1.7287	0.1828	0.10676	53.68471	2.5877	3.34486	0.05461	0.29898	111.4442
			ST DEV	0.17553	0.04136	0.02677188	16.289782	0.36529	0.33925	0.003758	0.03278	25.39033

Table 5.8: Radiation+Zoledronate study 14 day proximal tibia trabecular microCT raw data

BONE	RAD	Treatment		VOX-TV	VOX-BV	VOX-BV/TV	Conn-Dens.	TRI-SMI	DT-Tb.N	DT-Tb.Th	DT-Tb.Sp	vBMD
6474	NR	PLAC		2.0905	0.078	0.0373	3.8269	2.7955	2.3222	0.0556	0.4311	47.0258
6477	NR	PLAC		2.0243	0.06	0.0296	1.482	3.205	1.8644	0.061	0.5349	42.8964
6479	NR	PLAC		2.499	0.0674	0.027	3.2012	2.9139	1.7096	0.0533	0.5847	31.8015
6483	NR	PLAC		2.3094	0.0656	0.0284	3.464	3.4287	1.9139	0.0732	0.5572	35.0549
6484	NR	PLAC		2.2503	0.1373	0.061	45.7715	2.3681	2.0651	0.0601	0.4934	23.2925
6485	NR	PLAC		2.4216	0.0688	0.0284	4.3361	2.1965	1.5737	0.0548	0.6376	40.7275
6494	NR	PLAC		2.46	0.0676	0.0275	6.9106	3.051	1.7851	0.0528	0.5781	35.6388
6495	NR	PLAC		2.1789	0.0265	0.0122	-0.2295	3.8843	1.5892	0.0512	0.6329	30.0079
6496	NR	PLAC		2.2834	0.0595	0.0261	2.4086	2.8238	1.6396	0.0632	0.6467	39.7264
			MEAN	2.279711	0.070078	0.030833333	7.907933333	2.962977778	1.8292	0.058355556	0.566288889	36.2413
			ST DEV	0.163433	0.029002	0.013041376	14.33401623	0.515175957	0.245506701	0.006907625	0.071696782	7.253247
6491	NR	ZOL		2.4695	0.8966	0.3631	96.9829	-1.7085	4.4382	0.0816	0.246	358.2274
6499	NR	ZOL		2.4277	1.1445	0.4714	115.7468	-3.3499	5.7504	0.0874	0.1961	450.1989
6500	NR	ZOL		2.6091	1.0311	0.3952	136.2523	-1.8221	4.9229	0.0813	0.2296	390.8033
6501	NR	ZOL		2.5505	1.1933	0.4679	105.2753	-3.4431	5.6343	0.0816	0.2021	467.05
6502	NR	ZOL		2.4842	0.8761	0.3527	169.0663	-1.5403	4.7696	0.071	0.2316	336.9134
6504	NR	ZOL		2.3399	0.9832	0.4202	117.9558	-3.1285	5.0395	0.083	0.232	414.7033
6505	NR	ZOL		2.6406	1.0211	0.3867	127.2448	-2.0295	5.3369	0.0765	0.2107	364.2337
6507	NR	ZOL		2.5924	1.2988	0.501	97.5941	-5.6776	4.9676	0.0861	0.2615	471.221
6508	NR	ZOL		2.8179	1.29	0.4578	124.9163	-3.0268	5.6306	0.087	0.1996	427.7588
6509	NR	ZOL		2.5421	1.2104	0.4761	122.1449	-4.715	5.4909	0.0828	0.2225	438.9789
			MEAN	2.54739	1.09451	0.42921	121.31795	-3.04413	5.19809	0.08183	0.22317	412.0089
			ST DEV	0.131307	0.154312	0.052404462	21.09877131	1.356273706	0.434925124	0.004993117	0.021262907	47.42327
6470	IRR	PLAC		2.6369	0.1097	0.0416	14.2212	3.341	2.3752	0.0588	0.4197	44.7317
6471	IRR	PLAC		2.376	0.0975	0.041	5.8922	3.0948	2.1137	0.0728	0.4773	37.3907
6473	IRR	PLAC		2.2582	0.0673	0.0298	1.9928	3.9723	2.1285	0.0723	0.4678	25.7534
6476	IRR	PLAC		2.4001	0.099	0.0412	-0.2083	3.0913	1.7744	0.0765	0.5798	36.7233
6478	IRR	PLAC		2.3684	0.0648	0.0274	2.7445	3.2637	1.8142	0.0666	0.551	21.0819
6486	IRR	PLAC		2.603	0.0454	0.0174	0.5763	2.6618	1.3078	0.078	0.7745	19.8723
6487	IRR	PLAC		2.1631	0.0603	0.0279	4.6229	3.5701	1.9493	0.0726	0.5176	43.3135
6497	IRR	PLAC		2.5392	0.072	0.0284	4.726	3.5137	1.8632	0.0689	0.5368	24.5021
6503	IRR	PLAC		2.1837	0.1213	0.0556	22.4389	2.6039	2.3142	0.059	0.4329	65.9623
			MEAN	2.392067	0.081922	0.034477778	6.334055556	3.234733333	1.960055556	0.0695	0.5286	35.48124
			ST DEV	0.173468	0.02565	0.011338185	7.37366741	0.434854461	0.324117873	0.006920079	0.106726449	14.779
6472	IRR	ZOL		2.2495	0.9549	0.4245	99.5787	-3.3502	4.6049	0.0756	0.233	412.159
6475	IRR	ZOL		2.5928	1.1758	0.4535	180.6913	-1.1868	5.9149	0.0874	0.1581	445.1103
6480	IRR	ZOL		2.5465	1.1137	0.4374	108.5809	-2.2419	4.887	0.0821	0.2085	442.9831
6482	IRR	ZOL		2.3491	1.0017	0.4264	137.4996	-2.8236	4.8056	0.0787	0.2276	411.4917
6488	IRR	ZOL		2.4547	0.8025	0.3269	111.0107	-1.032	4.5071	0.0687	0.2275	336.3711
6489	IRR	ZOL		2.2674	0.9827	0.4334	103.4234	-2.8535	4.8846	0.0819	0.2204	415.037
6490	IRR	ZOL		2.0944	0.8507	0.4062	79.9768	-1.6407	4.5053	0.0847	0.23	409.865
6492	IRR	ZOL		2.609	1.1785	0.4517	65.1595	-3.6276	4.3256	0.0964	0.2642	462.6287
6493	IRR	ZOL		2.4007	0.927	0.3862	71.0208	-2.1468	4.1069	0.0828	0.2655	383.6291
6506	IRR	ZOL		2.3203	1.2236	0.5273	65.5091	-4.9135	5.14	0.1026	0.2391	522.8585
			MEAN	2.38844	1.02111	0.42735	102.24508	-2.58166	4.76819	0.08409	0.22739	424.2134
			ST DEV	0.165509	0.145372	0.051255596	36.08303967	1.192177293	0.503254547	0.00974046	0.030165486	49.39204

Table 5.9: Radiation+Zoledronate study 6 month proximal tibia trabecular microCT raw data

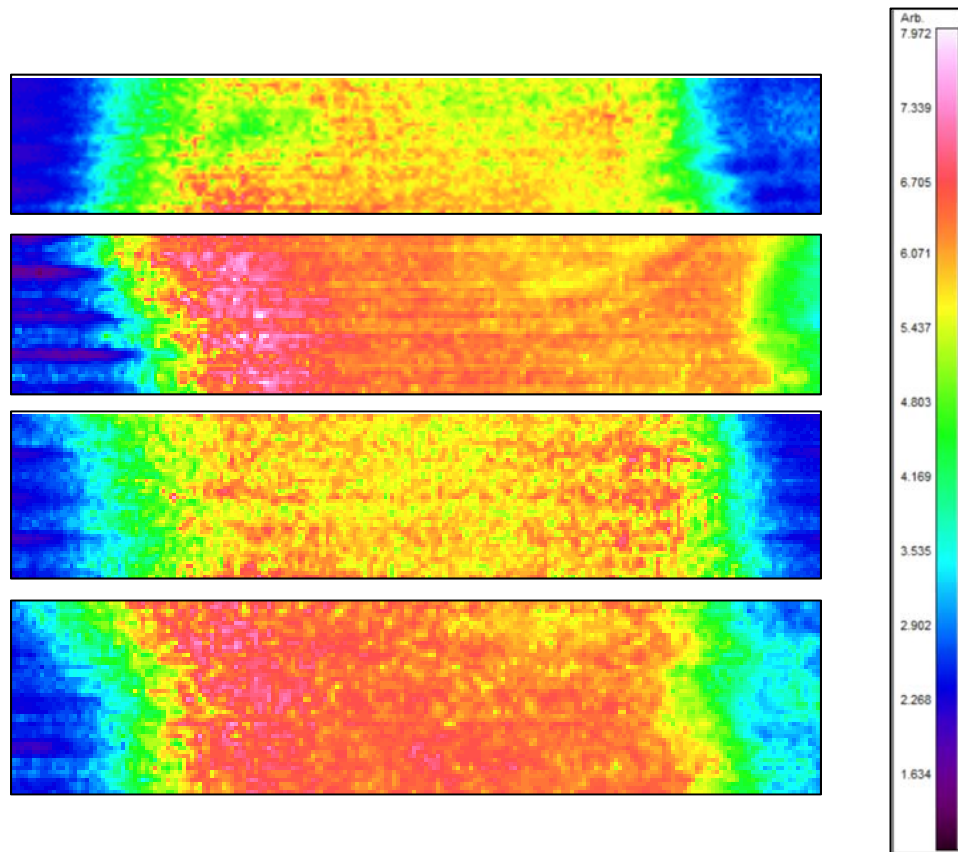


Figure 5.3: Radiation+Zoledronate study example Mineral to Matrix Ratio mapping for FTIR data. Embedding material appears dark blue to light blue and bone spans roughly green to green from left to right. Endosteal surface=left green, periosteal surface=right green

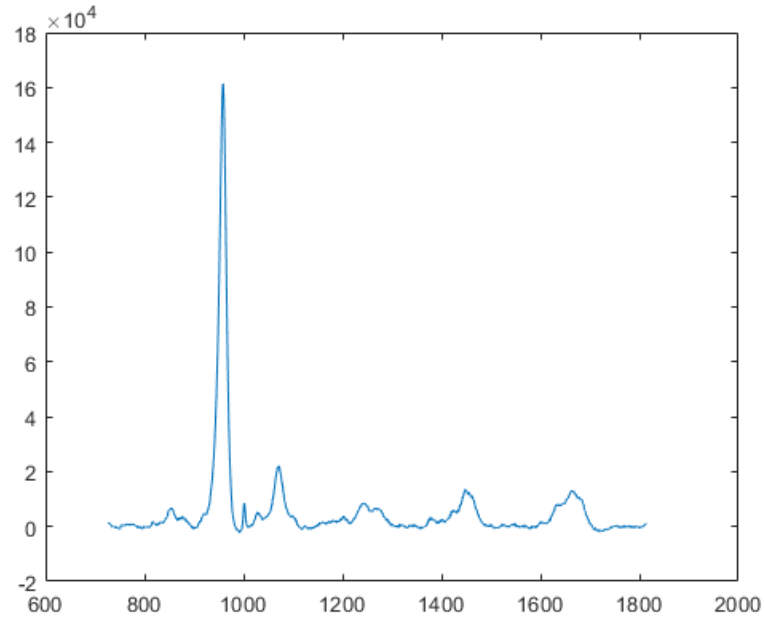


Figure 5.5: Example Raman MATLAB spectra of bone after baseline subtraction and PMMA subtraction (x-axis represents wave shift and y-axis represents intensity)

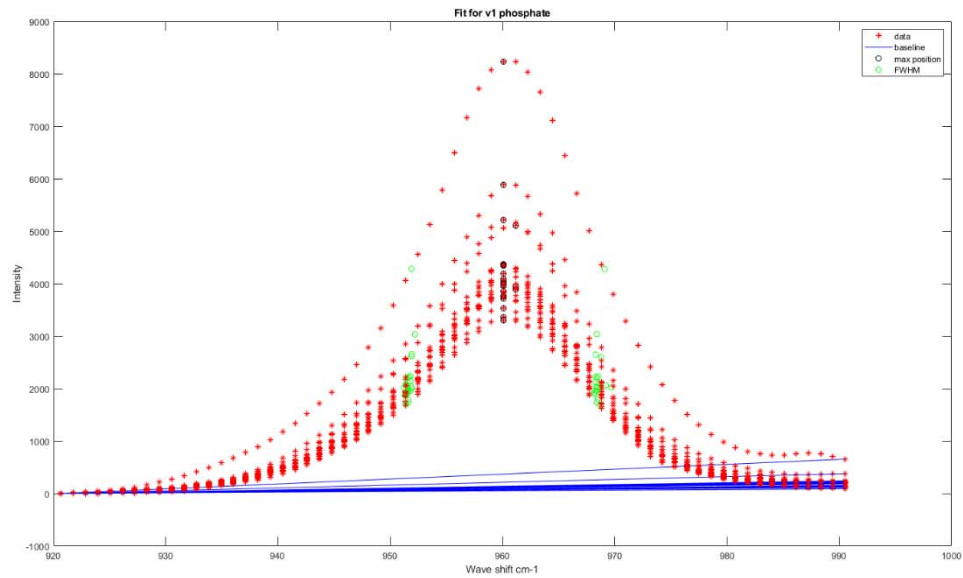


Figure 5.4: Example MATLAB calculation of full-width half maximum (green circle) for phosphate peak in Raman spectroscopy data

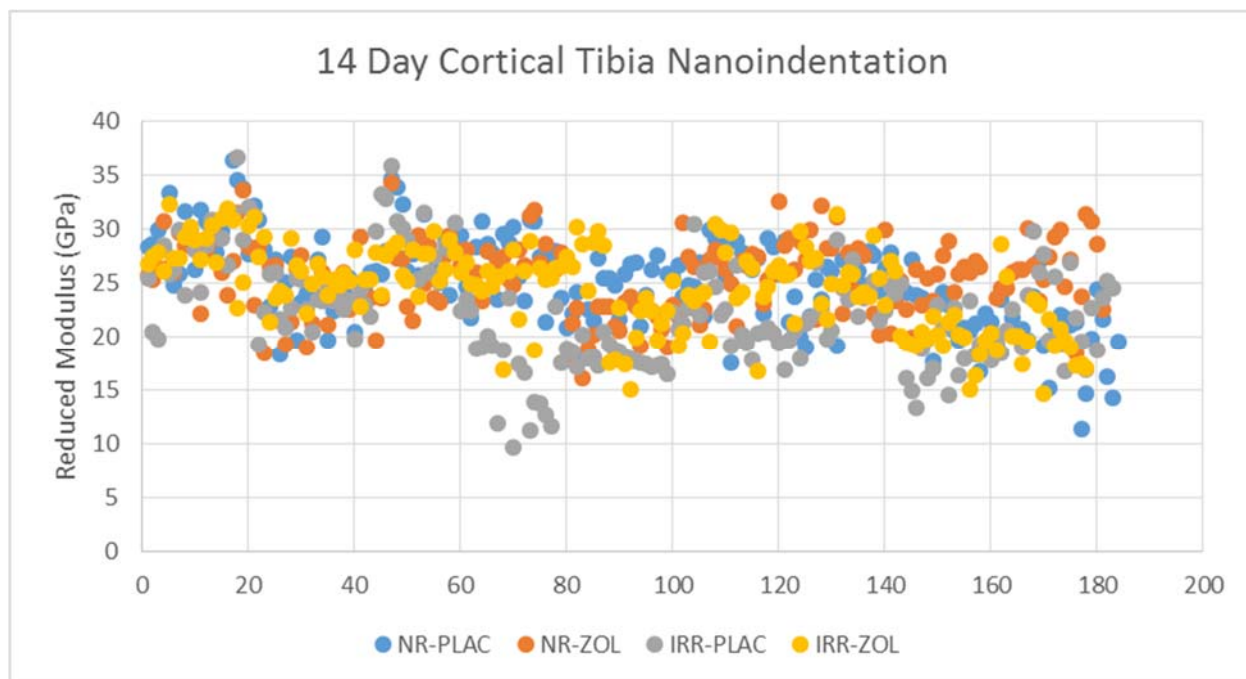


Figure 5.6: Nanoindentation data collected for 14 day time point for Radiation+Zoledronate study

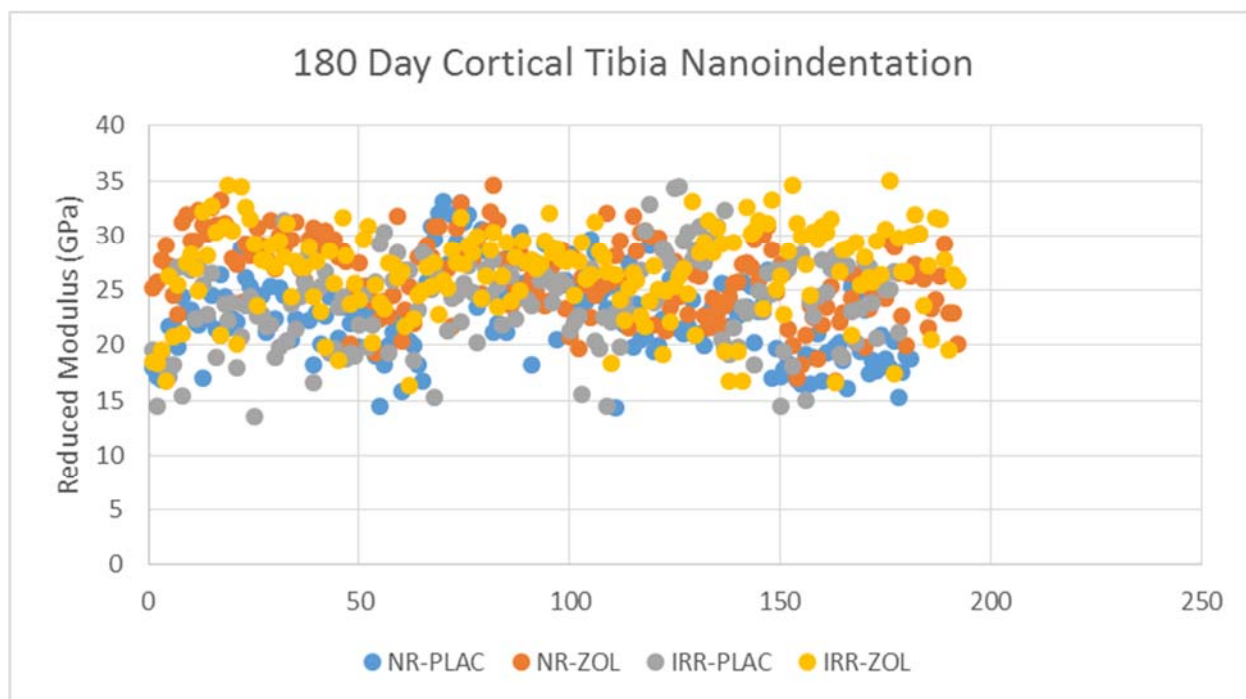


Figure 5.7: Nanoindentation data collected for 6 month time point for Radiation+Zoledronate study

Chapter 4

Bone	Cage	Limb	Sex	VOX-TV	VOX-BV	VOX-BV/TV	Conn-Dens.	TRI-SMI	DT-Tb.N	DT-Tb.Th	DT-Tb.Sp	vBMD
7414	13-0	R	M	1.833	0.0953	0.052	87.8324	2.7951	3.6978	0.0331	0.2697	45.3897
7416	13-1	R	M	1.698	0.1069	0.063	91.5802	2.2672	3.4951	0.0339	0.2859	62.9226
7367	13-2	R	M	1.6946	0.1229	0.0725	129.5316	2.2456	4.0797	0.0325	0.2435	65.4398
7413	14-0	R	M	1.826	0.1028	0.0563	88.7189	2.58	3.5219	0.0347	0.2805	58.1488
7420	14-1	R	M	1.6891	0.0748	0.0443	42.923	3.052	3.4766	0.0339	0.2871	46.518
7366	14-2	R	M	1.6292	0.0919	0.0564	93.297	2.7265	3.5217	0.0343	0.2836	59.8848
7422	15-0	R	M	1.6871	0.0926	0.0549	88.3167	2.8021	3.3662	0.0365	0.2931	41.4838
7426	15-1	R	M	1.5996	0.0651	0.0407	42.5104	2.9666	3.4805	0.0339	0.2906	50.4239
7428	15-2	R	M	1.6838	0.0884	0.0525	73.3471	2.7559	3.3097	0.0353	0.3031	49.1219
7458	15-3	R	M	1.6055	0.0851	0.053	99.0358	2.7824	3.7237	0.0322	0.2681	51.2919
			mean			0.05456	83.70931	2.69734	3.56729	0.03403	0.28052	53.06252
			stdev			0.00888322	25.8629526	0.265244	0.22009	0.001284	0.016644	8.056933
7328	13-0	L	M	1.783	0.0784	0.044	47.6718	2.8025	3.4212	0.0325	0.2914	45.6501
7415	13-1	L	M	1.6307	0.0708	0.0434	49.0577	2.8075	3.043	0.0353	0.3301	39.5743
7329	13-2	L	M	1.663	0.084	0.0505	56.5249	2.7561	3.8719	0.0316	0.2582	48.5144
7417	14-0	L	M	1.7034	0.0597	0.035	27.5917	3.1216	3.394	0.0339	0.293	29.6794
7425	14-1	L	M	1.7027	0.0491	0.0288	16.1506	2.9853	3.2918	0.0291	0.3046	26.3812
7334	14-2	L	M	1.7334	0.0658	0.0379	30.8646	2.9104	3.1642	0.034	0.3166	40.6158
7421	15-0	L	M	1.6634	0.072	0.0433	47.1911	2.8912	3.3032	0.0333	0.3009	45.6501
7423	15-1	L	M	1.6927	0.056	0.0331	18.0185	3.0345	3.2768	0.0319	0.3051	32.2833
7427	15-2	L	M	1.6327	0.0558	0.0342	37.975	3.0519	3.3434	0.0308	0.3013	34.5401
7451	15-3	L	M	1.6209	0.0601	0.0371	41.6441	2.9536	3.5067	0.0299	0.2848	38.7063
			mean			0.03873	37.269	2.93146	3.36162	0.03223	0.2986	38.1595
			stdev			0.00647286	13.6922704	0.119943	0.221695	0.001953	0.019186	7.34882

Table 5.11: Hemophilia study 7 day male distal femur trabecular microCT raw data

Bone	Cage	Limb	Sex	VOX-TV	VOX-BV	VOX-BV/TV	Conn-Dens.	TRI-SMI	DT-Tb.N	DT-Tb.Th	DT-Tb.Sp	vBMD
7454	16-0	R	F	1.7095	0.175	0.1024	120.2101	1.9585	3.8349	0.0407	0.2596	109.1854
7374	16-1	R	F	1.4997	0.1004	0.0669	89.0153	2.4882	3.4097	0.0373	0.2896	77.7649
7457	16-2	R	F	1.7614	0.1668	0.0947	125.751	1.9866	3.8142	0.0397	0.2581	101.9812
7375	17-0	R	F	1.3231	0.0626	0.0473	72.556	2.9536	3.6331	0.0326	0.2782	56.1525
7460	17-1	R	F	1.5061	0.1225	0.0814	111.546	2.1703	3.5247	0.037	0.284	95.2979
			mean			0.07854	103.81568	2.31144	3.64332	0.03746	0.2739	88.07638
			stdev			0.0220797	22.3937042	0.41642	0.183478	0.003137	0.014328	21.31048
7453	16-0	L	F	1.6412	0.127	0.0774	118.5138	2.2887	3.9052	0.0355	0.2515	74.4666
7288	16-1	L	F	1.4217	0.1072	0.0754	85.1108	2.4691	3.5806	0.039	0.2766	86.6182
7455	16-2	L	F	1.4755	0.1136	0.077	97.2564	2.4048	3.5951	0.0405	0.2781	78.0253
7286	17-0	L	F	1.3155	0.052	0.0395	57.3914	3.0084	3.6843	0.0295	0.2711	56.0657
7459	17-1	L	F	1.3088	0.0676	0.0517	67.2387	2.7132	3.2247	0.0373	0.3137	49.8163
			mean			0.0642	85.10222	2.57684	3.59798	0.03636	0.2782	68.99842
			stdev			0.01753468	24.2438277	0.286822	0.245705	0.004266	0.022506	15.46812

Table 5.10: Hemophilia study 7 day female distal femur trabecular microCT raw data

Bone	Mouse	Sex	Limb		Smoothed Surface	Smoothed Volume	Unsmoothed Surface	Unsmoothed Volume	Avg Dist B/W Surfaces	Smoothness Ratio
7414	13-0	M	R		15.935242	6.02008	17.467581	5.85717	0.043325	0.912
7416	13-1	M	R		15.529947	5.888942	17.262119	5.739721	0.039813	0.900
7367	13-2	M	R		15.578012	5.684399	16.980193	5.531702	0.040866	0.917
7413	14-0	M	R		15.770549	5.923532	17.58263	5.768711	0.041651	0.897
7420	14-1	M	R		15.794462	5.985825	17.576474	5.825673	0.041269	0.899
7366	14-2	M	R		16.144063	6.048143	17.879661	5.85688	0.044736	0.903
7422	15-0	M	R		15.791216	5.914108	17.024336	5.793849	0.040796	0.928
7426	15-1	M	R		15.514881	5.783739	17.051712	5.623175	0.041938	0.910
7428	15-2	M	R		15.522461	5.901128	16.77438	5.750024	0.043214	0.925
7458	15-3	M	R		15.271797	5.486131	16.951362	5.322715	0.044172	0.901
7454	16-0	F	R		15.21752	5.512226	16.302387	5.368092	0.042091	0.933
7374	16-1	F	R		15.433214	5.723932	16.619615	5.575119	0.041149	0.929
7457	16-2	F	R		15.427561	5.9292	16.872918	5.780847	0.041608	0.914
7375	17-0	F	R		14.617586	5.077992	17.058505	4.905541	0.043512	0.857
7460	17-1	F	R		15.53902	5.899324	16.780721	5.753069	0.040945	0.926
7328	13-0	M	L		16.020544	5.868001	18.88933	5.677411	0.042577	0.848
7415	13-1	M	L		15.406064	5.615222	17.587608	5.467208	0.039159	0.876
7329	13-2	M	L		16.046998	5.793788	18.155318	5.595333	0.044627	0.884
7417	14-0	M	L		15.705087	5.703184	17.954761	5.545898	0.042495	0.875
7425	14-1	M	L		15.783726	5.669466	18.814291	5.43549	0.045349	0.839
7334	14-2	M	L		16.214891	5.752989	19.052503	5.508437	0.045871	0.851
7421	15-0	M	L		15.607848	5.689082	17.876303	5.536729	0.041026	0.873
7423	15-1	M	L		15.52975	5.630922	18.289615	5.439837	0.041915	0.849
7427	15-2	M	L		15.618022	5.584106	18.344345	5.381005	0.04423	0.851
7451	15-3	M	L		15.099106	5.369442	18.507771	5.197779	0.043725	0.816
7453	16-0	F	L		15.473143	5.351964	17.248178	5.138963	0.044752	0.897
7288	16-1	F	L		15.954524	5.485847	18.588345	5.231521	0.044667	0.858
7455	16-2	F	L		15.7042	5.726655	17.299066	5.544102	0.044207	0.908
7286	17-0	F	L		15.193716	5.172243	17.75293	4.95753	0.044175	0.856
7459	17-1	F	L		15.457235	5.476555	17.57182	5.27441	0.045937	0.880

Table 5.12: Hemophilia study 7 day male and female distal femur microCT smoothness ratio raw data

Bone	Cage	Mouse	Limb	Sex		VOX-TV	VOX-BV	VOX-BV/T	Conn-Den	TRI-SMI	DT-Tb.N	DT-Tb.Th	DT-Tb.Sp	vBMD
7676	10	0	R	M		1.6247	0.1195	0.0736	90.1716	2.6335	3.7168	0.0394	0.2664	78.5461
7678	10	1	R	M		1.7326	0.1296	0.0748	97.8316	2.7855	3.8377	0.0419	0.2561	83.2331
7680	11	0	R	M		1.7248	0.0966	0.056	70.7314	2.7008	3.4003	0.0357	0.2968	50.2503
7368	11	1	R	M		1.6717	0.1075	0.0643	78.0655	2.7172	3.6206	0.0392	0.2791	66.2209
7369	12	0	R	M		1.5412	0.0795	0.0516	66.5081	2.7725	3.6464	0.0346	0.2755	52.7674
7682	12	1	R	M		1.7234	0.1068	0.062	94.5808	2.5817	3.6164	0.0357	0.2748	64.485
7684	12	2	R	M		1.6247	0.0873	0.0537	78.4755	2.9325	3.5235	0.0367	0.2821	60.6659
7686	12	3	R	M		1.5922	0.0722	0.0453	40.825	3.0452	3.5116	0.0371	0.2836	39.0535
					mean			0.060163	77.14869	2.771113	3.609163	0.037538	0.2768	61.90278
					stdev			0.010479	18.43007	0.153084	0.134092	0.002436	0.012083	14.63924
7674	10	0	L	M		1.3056	0.0401	0.0307	39.0629	3.1144	3.3995	0.03	0.2963	36.6232
7677	10	1	L	M		1.6787	0.13	0.0774	109.6105	2.6491	3.8867	0.0397	0.2561	82.0179
7679	11	0	L	M		1.5393	0.0484	0.0315	24.6867	3.1479	2.8993	0.0359	0.3446	30.1134
7330	11	1	L	M		1.3293	0.0391	0.0294	26.7054	3.2859	3.2141	0.0316	0.3113	36.4496
7331	12	0	L	M		1.2716	0.0303	0.0238	23.5918	3.1305	3.115	0.0287	0.3252	24.298
7681	12	1	L	M		1.2842	0.0343	0.0267	31.536	3.0528	3.1776	0.0282	0.3112	30.4606
7683	12	2	L	M		1.5766	0.0564	0.0358	66.9141	2.7474	3.1577	0.0284	0.3188	36.0156
7685	12	3	L	M		1.1417	0.0226	0.0198	13.5766	3.2103	2.521	0.0302	0.398	13.622
					mean			0.034388	41.9605	3.042288	3.171363	0.031588	0.320188	36.20004
					stdev			0.018059	31.60115	0.224683	0.390233	0.00412	0.040559	20.07474

Table 5.13: Hemophilia study 14 day male distal femur trabecular microCT raw data

Bone	Cage	Mouse	Limb	Sex		VOX-TV	VOX-BV	VOX-BV/T	Conn-Den	TRI-SMI	DT-Tb.N	DT-Tb.Th	DT-Tb.Sp	vBMD
7589	7	1	R	F		1.502	0.1708	0.1137	139.1512	1.8855	4.0568	0.0408	0.2434	117.3443
7373	7	2	R	F		1.4002	0.1263	0.0902	130.3368	2.0548	3.9039	0.0374	0.2579	85.4898
7591	7	3	R	F		1.6691	0.1076	0.0645	106.0471	2.5274	3.5334	0.036	0.2814	62.7491
7594	8	1	R	F		1.6168	0.1315	0.0813	100.8154	2.0925	3.5732	0.0383	0.2768	94.3431
7605	8	2	R	F		1.3991	0.1118	0.0799	112.9334	2.2095	3.3499	0.0381	0.2946	82.6255
7607	8	3	R	F		1.3822	0.1321	0.0956	117.2024	1.9923	3.6323	0.0401	0.2752	91.4788
7636	9	1	R	F		1.5108	0.0678	0.0449	51.9604	3.0427	3.4088	0.0351	0.2929	48.0804
7638	9	2	R	F		1.6187	0.1139	0.0704	103.788	2.1566	3.3595	0.0359	0.3015	68.2173
					mean			0.080063	107.7793	2.245163	3.602225	0.037713	0.277963	81.29104
					stdev			0.020871	26.16315	0.373722	0.257495	0.002031	0.019537	21.41784
7588	7	1	L	F		1.0508	0.082	0.0781	100.4	2.0164	3.3905	0.0381	0.2898	86.5314
7284	7	2	L	F		0.9862	0.0606	0.0614	70.4695	2.4028	3.6841	0.0348	0.2711	71.3419
7590	7	3	L	F		1.259	0.0531	0.0422	60.3667	2.7962	3.2676	0.0325	0.306	41.4838
7593	8	1	L	F		1.1475	0.0595	0.0519	70.1535	2.5441	3.4633	0.0333	0.2936	62.3151
7604	8	2	L	F		1.1757	0.0806	0.0686	92.2885	2.3667	3.5021	0.037	0.29	76.463
7606	8	3	L	F		0.9232	0.067	0.0726	68.242	2.4825	3.5931	0.0433	0.277	85.4898
7635	9	1	L	F		1.2826	0.0464	0.0362	31.5753	3.214	3.2571	0.0343	0.3073	38.5327
7637	9	2	L	F		1.1202	0.0541	0.0483	74.091	2.4485	3.1738	0.0342	0.3067	60.4055
					mean			0.057413	70.94831	2.5339	3.41645	0.035938	0.292688	65.3204
					stdev			0.015093	20.71256	0.349352	0.177069	0.003501	0.013709	18.26816

Table 5.14: Hemophilia study 14 day female distal femur trabecular microCT raw data

Bone	Cage	Mouse	Sex	Limb		Smoothed Surface	Smoothed Volume	Unsmoothed Surface	Unsmoothed Volume	Avg Dist B/W Surfaces	Smoothness Ratio
7676	10	0	R	M		16.098166	6.047444	17.391649	5.869661	0.045113	0.926
7678	10	1	R	M		15.981284	5.90761	17.199517	5.758027	0.041638	0.929
7680	11	0	R	M		15.383531	5.605003	16.712122	5.439701	0.044463	0.921
7368	11	1	R	M		15.63342	5.644888	16.860587	5.481152	0.043293	0.927
7369	12	0	R	M		15.452936	5.644841	17.4741	5.509425	0.039099	0.884
7682	12	1	R	M		15.609279	5.762726	16.905039	5.5999	0.043205	0.923
7684	12	2	R	M		15.686686	5.822545	17.025737	5.652794	0.0432	0.921
7686	12	3	R	M		15.384604	5.678585	16.933788	5.501412	0.045592	0.909
7589	7	1	R	F		15.364798	5.607862	16.811148	5.455479	0.042253	0.914
7373	7	2	R	F		15.188897	5.377226	16.512984	5.244473	0.040672	0.920
7591	7	3	R	F		15.059866	5.406977	15.982573	5.283505	0.039834	0.942
7594	8	1	R	F		15.571749	5.731568	16.548112	5.601631	0.041147	0.941
7605	8	2	R	F		15.21272	5.595373	16.264817	5.440775	0.042714	0.935
7607	8	3	R	F		15.119068	5.406036	16.021759	5.266476	0.042986	0.944
7636	9	1	R	F		15.722841	5.919121	17.200876	5.746082	0.04449	0.914
7638	9	2	R	F		15.772005	6.004556	17.047446	5.840286	0.044615	0.925
7674	10	0	L	M		17.1404	6.220476	20.202814	5.969568	0.042672	0.848
7677	10	1	L	M		16.134152	6.169273	17.427955	6.011589	0.043377	0.926
7679	11	0	L	M		16.838521	5.826803	19.606438	5.545989	0.046242	0.859
7330	11	1	L	M		16.718686	5.839458	19.087469	5.572811	0.042735	0.876
7331	12	0	L	M		16.54382	5.776666	19.450437	5.512364	0.043866	0.851
7681	12	1	L	M		16.394748	5.978959	18.263421	5.757444	0.04326	0.898
7683	12	2	L	M		17.098638	6.358474	20.612176	6.084773	0.042432	0.830
7685	12	3	L	M		16.008298	5.561242	18.549694	5.331015	0.044376	0.863
7588	7	1	L	F		16.102916	5.519912	18.507427	5.270394	0.043771	0.870
7284	7	2	L	F		16.428728	5.683327	18.739436	5.418552	0.045481	0.877
7590	7	3	L	F		16.41398	5.776796	18.918011	5.530736	0.043699	0.868
7593	8	1	L	F		16.857735	5.846204	19.098036	5.565243	0.045767	0.883
7604	8	2	L	F		15.412229	5.66625	17.043661	5.509471	0.041147	0.904
7606	8	3	L	F		16.47192	5.567927	18.977188	5.293517	0.044413	0.868
7635	9	1	L	F		15.954027	5.629	17.641485	5.416272	0.044278	0.904
7637	9	2	L	F		16.924822	5.983453	19.37751	6.650791	0.047231	0.873

Table 5.15: Hemophilia study 14 day distal femur male and female microCT smoothness ratio raw data

Bone	Cage	Mouse	Limb	Sex		VOX-TV	VOX-BV	VOX-BV/TV	Conn-Den	TRI-SMI	DT-Tb.N	DT-Tb.Th	DT-Tb.Sp	vBMD
7567	4	1	R	M		1.5913	0.0685	0.0431	26.0788	3.2512	2.9599	0.0448	0.3339	42.699
7570	4	2	R	M		1.7225	0.113	0.0656	71.9884	2.6072	3.3138	0.0416	0.3011	68.5645
7572	4	3	R	M		1.7692	0.0724	0.0409	20.3486	3.3702	2.5776	0.049	0.3788	36.6232
7574	5	1	R	M		1.6688	0.0999	0.0598	58.1262	2.7965	3.4334	0.0427	0.2902	63.7038
7580	5	3	R	M		1.6284	0.1066	0.0655	65.0943	2.9069	3.2192	0.0465	0.3087	67.1757
7582	5	4	R	M		1.6476	0.0698	0.0424	43.3954	3.0709	3.1035	0.0389	0.3191	36.1024
7584	6	1	R	M		1.5573	0.0611	0.0392	52.334	3.1372	3.1984	0.0367	0.3137	34.2797
7587	6	2	R	M		1.5185	0.0426	0.028	32.2681	3.0858	2.7721	0.0354	0.3703	27.4227
					mean			0.0480625	46.20423	3.028238	3.072238	0.04195	0.326975	47.07138
					stdev			0.013827709	18.81116	0.247662	0.286519	0.004766	0.032082	16.65221
7566	4	1	L	M		1.6798	0.0439	0.0261	18.1565	3.6342	2.6495	0.0371	0.3771	11.1917
7569	4	2	L	M		1.4695	0.0588	0.04	38.1079	3.1446	2.9861	0.0394	0.3385	50.6843
7571	4	3	L	M		1.5875	0.0413	0.026	9.1339	3.5679	2.3076	0.0428	0.4377	21.1733
7573	5	1	L	M		1.6195	0.0471	0.0291	22.2286	3.6058	2.8887	0.0362	0.353	24.298
7579	5	3	L	M		1.6993	0.096	0.0565	37.6622	3.0774	3.037	0.0489	0.328	55.3713
7581	5	4	L	M		1.6728	0.0622	0.0372	27.4995	3.2378	2.8884	0.0389	0.3465	35.2344
7583	6	1	L	M		1.2673	0.0238	0.0187	6.3125	3.7806	2.7019	0.0339	0.3667	16.2259
7586	6	2	L	M		1.5607	0.0495	0.0317	22.1058	3.3339	2.5745	0.0398	0.395	31.589
					mean			0.0331625	22.65086	3.422775	2.754213	0.039625	0.367813	30.72099
					stdev			0.011567681	11.69917	0.258036	0.243573	0.004592	0.035514	15.81685

Table 5.16: Hemophilia study 28 day male distal femur trabecular microCT raw data

Bone	Cage	Mouse	Limb	Sex		VOX-TV	VOX-BV	VOX-BV/TV	Conn-Dens.	TRI-SMI	DT-Tb.N	DT-Tb.Th	DT-Tb.Sp	vBMD
7484	1	1	R	F		1.6929	0.1203	0.0711	96.5827	2.6333	3.3087	0.0425	0.3008	75.5082
7556	1	2	R	F		1.5438	0.0785	0.0509	78.6999	2.6424	3.0643	0.0359	0.3272	45.7369
7558	2	1	R	F		1.4737	0.0497	0.0337	48.177	3.1092	2.8407	0.0356	0.3449	40.5291
7560	2	2	R	F		1.4811	0.0879	0.0593	73.5935	2.8001	3.0283	0.0407	0.333	65.0058
7372	3	1	R	F		1.3955	0.0865	0.062	58.4028	2.5726	3.0401	0.0444	0.3321	66.5681
7563	3	2	R	F		1.5182	0.0709	0.0467	68.8337	2.6519	3.041	0.0372	0.3402	49.4691
7565	3	3	R	F		1.5015	0.1237	0.0824	84.2473	2.2598	3.4083	0.0436	0.2976	84.1879
					mean			0.058014286	72.64812857	2.667043	3.104486	0.039986	0.325114	61.00073
					stdev			0.016089586	16.13090996	0.254934	0.19113	0.003721	0.018631	16.22857
7483	1	1	L	F		1.3174	0.0984	0.0747	82.7384	2.7438	3.3285	0.0442	0.3047	81.4104
7555	1	2	L	F		1.185	0.082	0.0692	75.9466	2.4285	3.008	0.0438	0.3371	71.3419
7557	2	1	L	F		1.2861	0.0507	0.0394	54.0382	2.9007	2.8764	0.0373	0.3559	40.3555
7559	2	2	L	F		1.3163	0.0716	0.0544	66.8526	2.9787	3.3683	0.0418	0.2978	54.243
7283	3	1	L	F		1.0685	0.0487	0.0455	32.756	2.7718	2.8097	0.044	0.3554	59.7979
7562	3	2	L	F		1.3328	0.0524	0.0393	50.645	2.9077	3.0726	0.0348	0.3345	42.8726
7564	3	3	L	F		1.0736	0.0834	0.0777	67.5294	2.2276	3.1793	0.0417	0.317	88.7013
					mean			0.057171429	61.50088571	2.7084	3.091829	0.041086	0.328914	62.67466
					stdev			0.016595553	16.95339146	0.278253	0.213504	0.003658	0.023182	18.58839

Table 5.17: Hemophilia study 28 day female distal femur trabecular microCT raw data

Bone	Cage	Mouse	Sex	Limb		Smoothed Surface	Smoothed Volume	Unsmoothed Surface	Unsmoothed Volume	Avg Dist B/W Surfaces	Smoothness Ratio
7567	4	1	M	R		15.464343	5.587304	16.731585	5.438365	0.042452	0.924
7570	4	2	M	R		15.815441	5.851648	17.49438	5.681662	0.042858	0.904
7572	4	3	M	R		15.599304	5.948141	17.405721	5.788374	0.041051	0.896
7574	5	1	M	R		15.722147	5.953772	17.983744	5.781172	0.043075	0.874
7582	5	4	M	R		15.57477	5.877714	17.115993	5.700062	0.043879	0.910
7584	6	1	M	R		15.319872	5.641923	16.539148	5.499987	0.04257	0.926
7587	6	2	M	R		15.116242	5.447719	16.80826	5.278989	0.044708	0.899
7484	1	1	F	R		15.548997	5.712913	16.319816	5.520467	0.045507	0.953
7556	1	2	F	R		14.948842	5.280682	16.004523	5.144027	0.041429	0.934
7558	2	1	F	R		15.261264	5.539311	16.831307	5.385654	0.0412	0.907
7560	2	2	F	R		15.03495	5.400912	16.189968	5.25637	0.043821	0.929
7372	3	1	F	R		15.210144	5.525913	16.474981	5.372185	0.04313	0.923
7563	3	2	F	R		15.37999	5.700497	16.97575	5.523308	0.043731	0.906
7565	3	3	F	R		15.677605	5.82735	17.045368	5.646246	0.043885	0.920
7566	4	1	M	L		17.757067	6.551532	20.833671	6.290814	0.042798	0.852
7569	4	2	M	L		17.263769	6.311147	19.661657	6.047939	0.043862	0.878
7571	4	3	M	L		16.872719	6.108522	18.676973	5.829409	0.044857	0.903
7573	5	1	M	L		17.982778	6.840592	21.962639	6.548373	0.044767	0.819
7581	5	4	M	L		16.814775	6.400316	19.549672	6.143586	0.042526	0.860
7583	6	1	M	L		16.371559	5.659333	18.661996	5.440204	0.04219	0.877
7586	6	2	M	L		15.548231	5.370789	17.233788	5.183357	0.04211	0.902
7483	1	1	F	L		17.334766	6.269121	20.288576	5.947821	0.046036	0.854
7555	1	2	F	L		15.810539	5.482948	17.524152	5.276077	0.042522	0.902
7557	2	1	F	L		16.396863	5.85041	18.616133	5.606648	0.042529	0.881
7559	2	2	F	L		17.459496	5.925364	20.693067	5.654189	0.041464	0.844
7283	3	1	F	L		17.394983	5.810463	19.96115	5.534362	0.042032	0.871
7562	3	2	F	L		16.676864	5.848213	18.865349	5.618741	0.041631	0.884
7564	3	3	F	L		17.558508	6.239688	20.553942	5.986088	0.043017	0.854

Table 5.18: Hemophilia study 28 day male and female distal femur microCT smoothness ratio raw data

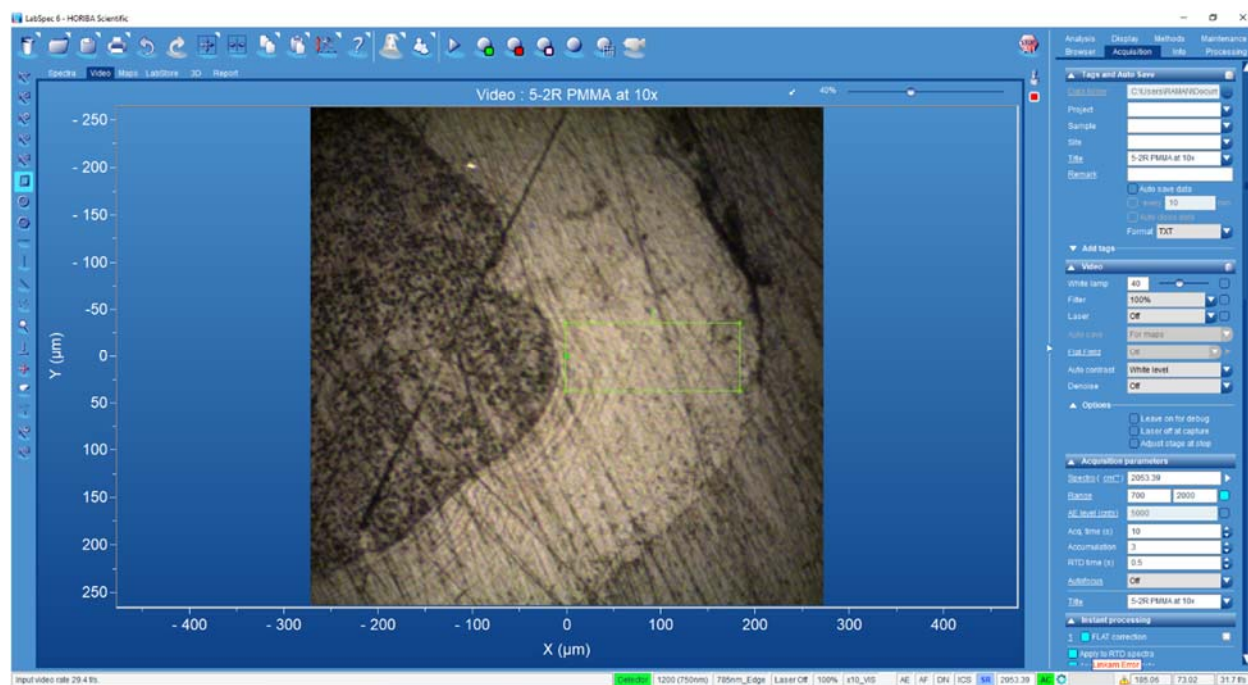


Figure 5.8: Example setup for hemophilia study Raman spectroscopy array on uninjured limb distal femur cortical bone

REFERENCES

1. Liu Y, Luo D, Wang T (2016) Hierarchical Structures of Bone and Bioinspired Bone Tissue Engineering. *Small* 12:4611-4632
2. Kobrina Y, Turunen M, Saarakkala S, Jurvelin J, Hauta-Kasari M, Isaksson H (2010) Cluster analysis of infrared spectra of rabbit cortical bone samples during maturation and growth. *The Analyst* 135:3147-3155
3. Baxter NN, Habermann EB, Tepper JE, Durham SB, Virnig BA (2005) Risk of pelvic fractures in older women following pelvic irradiation. *Jama* 294:2587-2593
4. Fonseca H, Moreira-Gonçalves D, Coriolano H-JA, Duarte JA (2014) Bone Quality: The Determinants of Bone Strength and Fragility. *Sports Medicine* 44:37-53
5. Goswami A, Bora A, Kundu G, Ghosh S, Goswami A (2014) Bleeding disorders in dental practice: A diagnostic overview. *Journal of the International Clinical Dental Research Organization* 6:143-150
6. Pulles AE, Mastbergen SC, Schutgens REG, Lafeber FPJG, van Vulpen LFD (2017) Pathophysiology of hemophilic arthropathy and potential targets for therapy. *Pharmacological Research* 115:192-199
7. Oliver WC, Pharr GM (1992) An improved technique for determining hardness and elastic modulus using load and displacement sensing indentation experiments. *Journal of Materials Research* 7:1564-1583
8. Torres-del-Pliego E, Vilaplana L, Guerri-Fernandez R, Diez-Perez A (2013) Measuring bone quality. *Curr Rheumatol Rep* 15:373
9. Siddiqui JA, Partridge NC (2016) Physiological Bone Remodeling: Systemic Regulation and Growth Factor Involvement. *Physiology (Bethesda)* 31:233-245
10. Morris MD, Mandair GS (2011) Raman assessment of bone quality. *Clin Orthop Relat Res* 469:2160-2169
11. Del Carmen MG, Rice LW (2017) Management of menopausal symptoms in women with gynecologic cancers. *Gynecologic oncology* 146:427-435

12. Clarke B (2008) Normal bone anatomy and physiology. Clin J Am Soc Nephrol 3 Suppl 3:S131-139
13. Florencio-Silva R, Sasso GR, Sasso-Cerri E, Simoes MJ, Cerri PS (2015) Biology of Bone Tissue: Structure, Function, and Factors That Influence Bone Cells. Biomed Res Int 2015:421746
14. Buck DW, 2nd, Dumanian GA (2012) Bone biology and physiology: Part I. The fundamentals. Plast Reconstr Surg 129:1314-1320
15. Katsimbri P (2017) The biology of normal bone remodelling. Eur J Cancer Care (Engl) 26
16. Rho JY, Kuhn-Spearing L, Zioupos P (1998) Mechanical properties and the hierarchical structure of bone. Medical engineering & physics 20:92-102
17. Reznikov N, Shahar R, Weiner S (2014) Bone hierarchical structure in three dimensions. Acta Biomater 10:3815-3826
18. Kenkre JS, Bassett J (2018) The bone remodelling cycle. Ann Clin Biochem 55:308-327
19. Krugh M, Langaker MD (2020) Dual Energy Xray Absorptiometry (DEXA). In: StatPearls. StatPearls Publishing
20. Garg MK, Kharb S (2013) Dual energy X-ray absorptiometry: Pitfalls in measurement and interpretation of bone mineral density. Indian J Endocrinol Metab 17:203-210
21. Forsyth JJ, Davey RC (2008) Chapter 7 - Bone health. In: Buckley JP (ed) Exercise Physiology in Special Populations. Churchill Livingstone, Edinburgh, p 225-247
22. de Bakker CMJ, Tseng WJ, Li Y, Zhao H, Liu XS (2017) Clinical Evaluation of Bone Strength and Fracture Risk. Current osteoporosis reports 15:32-42
23. Oei L, Koromani F, Rivadeneira F, Zillikens MC, Oei EHG (2016) Quantitative imaging methods in osteoporosis. Quant Imaging Med Surg 6:680-698
24. Komori T (2015) Animal models for osteoporosis. Eur J Pharmacol 759:287-294

25. Bouxsein ML, Boyd SK, Christiansen BA, Guldberg RE, Jepsen KJ, Muller R (2010) Guidelines for assessment of bone microstructure in rodents using micro-computed tomography. *Journal of bone and mineral research : the official journal of the American Society for Bone and Mineral Research* 25:1468-1486
26. Sanseverino MJ, Speacht TL, Donahue HJ, Lau AG (2018) The Effects of Hind Limb Suspension and Cast Mediated Immobilization on Bone Strength Properties. *Conf Proc IEEE Eng Med Biol Soc* 2018:1747-1750
27. Meganck JA, Liu B (2017) Dosimetry in Micro-computed Tomography: a Review of the Measurement Methods, Impacts, and Characterization of the Quantum GX Imaging System. *Mol Imaging Biol* 19:499-511
28. Hart NH, Nimphius S, Rantalainen T, Ireland A, Siafarikas A, Newton RU (2017) Mechanical basis of bone strength: influence of bone material, bone structure and muscle action. *Journal of musculoskeletal & neuronal interactions* 17:114-139
29. Ott SM (2018) Cortical or Trabecular Bone: What's the Difference? *Am J Nephrol* 47:373-375
30. Paschalis EP, Mendelsohn R, Boskey AL (2011) Infrared assessment of bone quality: a review. *Clin Orthop Relat Res* 469:2170-2178
31. Wu D, Isaksson P, Ferguson SJ, Persson C (2018) Young's modulus of trabecular bone at the tissue level: A review. *Acta Biomaterialia* 78:1-12
32. Mandair GS, Morris MD (2015) Contributions of Raman spectroscopy to the understanding of bone strength. *BoneKEY reports* 4:620-620
33. Turunen MJ, Saarakkala S, Rieppo L, Helminen HJ, Jurvelin JS, Isaksson H (2011) Comparison between infrared and Raman spectroscopic analysis of maturing rabbit cortical bone. *Appl Spectrosc* 65:595-603
34. Boskey AL, Imbert L (2017) Bone quality changes associated with aging and disease: a review. *Annals of the New York Academy of Sciences* 1410:93-106
35. Bi X, Grafe I, Ding H, Flores R, Munivez E, Jiang MM, Dawson B, Lee B, Ambrose CG (2017) Correlations Between Bone Mechanical Properties and Bone Composition Parameters in Mouse Models of Dominant and Recessive Osteogenesis Imperfecta and

the Response to Anti-TGF-beta Treatment. *Journal of bone and mineral research : the official journal of the American Society for Bone and Mineral Research* 32:347-359

36. Bala Y, Seeman E (2015) Bone's Material Constituents and their Contribution to Bone Strength in Health, Disease, and Treatment. *Calcif Tissue Int* 97:308-326
37. Yerramshetty JS, Akkus O (2008) The associations between mineral crystallinity and the mechanical properties of human cortical bone. *Bone* 42:476-482
38. Jimenez-Palomar I, Shipov A, Shahar R, Barber AH (2015) Mechanical Behavior of Osteoporotic Bone at Sub-Lamellar Length Scales. *Frontiers in Materials* 2
39. Takata S, Yonezu H, Shibata A, Enishi T, Sato N, Takahashi M, Nakao S, Komatsu K, Yasui N (2011) Mineral to matrix ratio determines biomaterial and biomechanical properties of rat femur--application of Fourier transform infrared spectroscopy. *J Med Invest* 58:197-202
40. Glaser DL, Kaplan FS (1997) Osteoporosis. Definition and clinical presentation. *Spine (Phila Pa 1976)* 22:12s-16s
41. Black DM, Rosen CJ (2016) Postmenopausal Osteoporosis. *New England Journal of Medicine* 374:254-262
42. Siegel RL, Miller KD, Jemal A (2017) Cancer Statistics, 2017. *CA: a cancer journal for clinicians* 67:7-30
43. Shevde NK, Bendixen AC, Dienger KM, Pike JW (2000) Estrogens suppress RANK ligand-induced osteoclast differentiation via a stromal cell independent mechanism involving c-Jun repression. *Proceedings of the National Academy of Sciences of the United States of America* 97:7829-7834
44. Eghbali-Fatourehchi G, Khosla S, Sanyal A, Boyle WJ, Lacey DL, Riggs BL (2003) Role of RANK ligand in mediating increased bone resorption in early postmenopausal women. *J Clin Invest* 111:1221-1230
45. Khosla S, Oursler MJ, Monroe DG (2012) Estrogen and the skeleton. *Trends Endocrinol Metab* 23:576-581

46. Pacifici R (1996) Estrogen, cytokines, and pathogenesis of postmenopausal osteoporosis. *Journal of bone and mineral research : the official journal of the American Society for Bone and Mineral Research* 11:1043-1051
47. Roberts BC, Giorgi M, Oliviero S, Wang N, Boudiffa M, Dall'Ara E (2019) The longitudinal effects of ovariectomy on the morphometric, densitometric and mechanical properties in the murine tibia: A comparison between two mouse strains. *Bone* 127:260-270
48. Tella SH, Gallagher JC (2014) Prevention and treatment of postmenopausal osteoporosis. *J Steroid Biochem Mol Biol* 142:155-170
49. Dhillon S (2016) Zoledronic Acid (Reclast((R)), Aclasta((R))): A Review in Osteoporosis. *Drugs* 76:1683-1697
50. Zhang J, Qiu X, Xi K, Hu W, Pei H, Nie J, Wang Z, Ding J, Shang P, Li B, Zhou G (2018) Therapeutic ionizing radiation induced bone loss: a review of in vivo and in vitro findings. *Connect Tissue Res* 59:509-522
51. Morris KA, Haboubi NY (2015) Pelvic radiation therapy: Between delight and disaster. *World journal of gastrointestinal surgery* 7:279-288
52. Yamamoto K, Nagao S, Suzuki K, Kogiku A, Senda T, Yano H, Kitai M, Shiozaki T, Matsuoka K, Yamaguchi S (2017) Pelvic fractures after definitive and postoperative radiotherapy for cervical cancer: A retrospective analysis of risk factors. *Gynecologic oncology* 147:585-588
53. Cenzer IS, Tang V, Boscardin WJ, Smith AK, Ritchie C, Wallhagen MI, Espaldon R, Covinsky KE (2016) One-Year Mortality After Hip Fracture: Development and Validation of a Prognostic Index. *Journal of the American Geriatrics Society* 64:1863-1868
54. Mitchell MJ, Logan PM (1998) Radiation-induced changes in bone. *Radiographics* 18:1125-1136; quiz 1242-1123
55. Wright LE, Buijs JT, Kim HS, Coats LE, Scheidler AM, John SK, She Y, Murthy S, Ma N, Chin-Sinex HJ, Bellido TM, Bateman TA, Mendonca MS, Mohammad KS, Guise TA (2015) Single-Limb Irradiation Induces Local and Systemic Bone Loss in a Murine Model. *Journal of bone and mineral research : the official journal of the American Society for Bone and Mineral Research* 30:1268-1279

56. Nishiyama K, Inaba F, Higashihara T, Kitatani K, Kozuka T (1992) Radiation osteoporosis — an assessment using single energy quantitative computed tomography. *European Radiology* 2:322-325
57. Hopewell JW (2003) Radiation-therapy effects on bone density. *Medical and Pediatric Oncology* 41:208-211
58. Stroud JS, Mutch D, Rader J, Powell M, Thaker PH, Grigsby PW (2009) Effects of cancer treatment on ovarian function. *Fertility and Sterility* 92:417-427
59. Willey JS, Lloyd SA, Nelson GA, Bateman TA (2011) Ionizing Radiation and Bone Loss: Space Exploration and Clinical Therapy Applications. *Clinical reviews in bone and mineral metabolism* 9:54-62
60. Pacheco R, Stock H (2013) Effects of radiation on bone. *Current osteoporosis reports* 11:299-304
61. Lam J, Takeshita S, Barker JE, Kanagawa O, Ross FP, Teitelbaum SL (2000) TNF-alpha induces osteoclastogenesis by direct stimulation of macrophages exposed to permissive levels of RANK ligand. *J Clin Invest* 106:1481-1488
62. Willey JS, Lloyd SA, Robbins ME, Bourland JD, Smith-Sielicki H, Bowman LC, Norrdin RW, Bateman TA (2008) Early increase in osteoclast number in mice after whole-body irradiation with 2 Gy X rays. *Radiation research* 170:388-392
63. Oest ME, Franken V, Kuchera T, Strauss J, Damron TA (2015) Long-term loss of osteoclasts and unopposed cortical mineral apposition following limited field irradiation. *Journal of orthopaedic research : official publication of the Orthopaedic Research Society* 33:334-342
64. Kondo H, Searby ND, Mojarrab R, Phillips J, Alwood J, Yumoto K, Almeida EA, Limoli CL, Globus RK (2009) Total-body irradiation of postpubertal mice with (137)Cs acutely compromises the microarchitecture of cancellous bone and increases osteoclasts. *Radiation research* 171:283-289
65. Fowler JF (2010) 21 years of biologically effective dose. *The British journal of radiology* 83:554-568

66. Hong JH, Chiang CS, Tsao CY, Lin PY, McBride WH, Wu CJ (1999) Rapid induction of cytokine gene expression in the lung after single and fractionated doses of radiation. *Int J Radiat Biol* 75:1421-1427
67. Willey JS, Livingston EW, Robbins ME, Bourland JD, Tirado-Lee L, Smith-Sielicki H, Bateman TA (2010) Risedronate prevents early radiation-induced osteoporosis in mice at multiple skeletal locations. *Bone* 46:101-111
68. Green DE, Rubin CT (2014) Consequences of irradiation on bone and marrow phenotypes, and its relation to disruption of hematopoietic precursors. *Bone* 63:87-94
69. Gong B, Oest ME, Mann KA, Damron TA, Morris MD (2013) Raman spectroscopy demonstrates prolonged alteration of bone chemical composition following extremity localized irradiation. *Bone* 57:252-258
70. Green DE, Adler BJ, Chan ME, Lennon JJ, Acerbo AS, Miller LM, Rubin CT (2013) Altered composition of bone as triggered by irradiation facilitates the rapid erosion of the matrix by both cellular and physicochemical processes. *PLoS One* 8:e64952
71. Hoyer LW (1994) Hemophilia A. *New England Journal of Medicine* 330:38-47
72. Wallny TA, Scholz DT, Oldenburg J, Nicolay C, Ezziddin S, Pennekamp PH, Stoffel-Wagner B, Kraft CN (2007) Osteoporosis in haemophilia - an underestimated comorbidity? *Haemophilia : the official journal of the World Federation of Hemophilia* 13:79-84
73. Gerstner G, Damiano ML, Tom A, Worman C, Schultz W, Recht M, Stopeck AT (2009) Prevalence and risk factors associated with decreased bone mineral density in patients with haemophilia. *Haemophilia : the official journal of the World Federation of Hemophilia* 15:559-565
74. Anagnostis P, Vakalopoulou S, Slavakis A, Charizopoulou M, Kazantzidou E, Chrysopoulou T, Vyzantiadis TA, Moka E, Agapidou A, Garipidou V (2012) Reduced bone mineral density in patients with haemophilia A and B in Northern Greece. *Thrombosis and haemostasis* 107:545-551
75. Kempton CL, Antun A, Antoniucci DM, Carpenter W, Ribeiro M, Stein S, Slovensky L, Elon L (2014) Bone density in haemophilia: a single institutional cross-sectional study. *Haemophilia : the official journal of the World Federation of Hemophilia* 20:121-128

76. Barnes C, Wong P, Egan B, Speller T, Cameron F, Jones G, Ekert H, Monagle P (2004) Reduced bone density among children with severe hemophilia. *Pediatrics* 114:e177-181
77. Kempton CL, Antoniucci DM, Rodriguez-Merchan EC (2015) Bone health in persons with haemophilia. *Haemophilia : the official journal of the World Federation of Hemophilia* 21:568-577
78. Recht M, Liel MS, Turner RT, Klein RF, Taylor JA (2013) The bone disease associated with factor VIII deficiency in mice is secondary to increased bone resorption. *Haemophilia : the official journal of the World Federation of Hemophilia* 19:908-912
79. Lau AG, Sun J, Hannah WB, Livingston EW, Heymann D, Bateman TA, Monahan PE (2014) Joint bleeding in factor VIII deficient mice causes an acute loss of trabecular bone and calcification of joint soft tissues which is prevented with aggressive factor replacement. *Haemophilia : the official journal of the World Federation of Hemophilia* 20:716-722
80. Siegel RL, Miller KD, Jemal A (2018) Cancer statistics, 2018. *CA: a cancer journal for clinicians* 68:7-30
81. Vordermark D (2016) Radiotherapy of Cervical Cancer. *Oncology research and treatment* 39:516-520
82. William T Creasman TRB, Jr (2019) Radiation Therapy in Gynecology. In: Huh WK (ed), Medscape
83. Schmeler KM, Jhingran A, Iyer RB, Sun CC, Eifel PJ, Soliman PT, Ramirez PT, Frumovitz M, Bodurka DC, Sood AK (2010) Pelvic fractures after radiotherapy for cervical cancer: implications for survivors. *Cancer* 116:625-630
84. Lima F, Swift JM, Greene ES, Allen MR, Cunningham DA, Braby LA, Bloomfield SA (2017) Exposure to Low-Dose X-Ray Radiation Alters Bone Progenitor Cells and Bone Microarchitecture. *Radiation research* 188:433-442
85. Diab DL, Watts NB (2013) Postmenopausal osteoporosis. *Current opinion in endocrinology, diabetes, and obesity* 20:501-509
86. Ji MX, Yu Q (2015) Primary osteoporosis in postmenopausal women. *Chronic diseases and translational medicine* 1:9-13

87. Langton CM, Pisharody S, Keyak JH (2009) Generation of a 3D proximal femur shape from a single projection 2D radiographic image. *Osteoporosis international : a journal established as result of cooperation between the European Foundation for Osteoporosis and the National Osteoporosis Foundation of the USA* 20:455-461
88. Lang TF, Sigurdsson S, Karlsdottir G, Oskarsdottir D, Sigmarsdottir A, Chengshi J, Kornak J, Harris TB, Sigurdsson G, Jonsson BY, Siggeirsdottir K, Eiriksdottir G, Gudnason V, Keyak JH (2012) Age-related loss of proximal femoral strength in elderly men and women: the Age Gene/Environment Susceptibility Study--Reykjavik. *Bone* 50:743-748
89. Lang TF, Keyak JH, Heitz MW, Augat P, Lu Y, Mathur A, Genant HK (1997) Volumetric quantitative computed tomography of the proximal femur: precision and relation to bone strength. *Bone* 21:101-108
90. Li JY, Tawfeek H, Bedi B, Yang X, Adams J, Gao KY, Zayzafoon M, Weitzmann MN, Pacifici R (2011) Ovariectomy disregulates osteoblast and osteoclast formation through the T-cell receptor CD40 ligand. *Proceedings of the National Academy of Sciences of the United States of America* 108:768-773
91. Kameda T, Mano H, Yuasa T, Mori Y, Miyazawa K, Shiokawa M, Nakamaru Y, Hiroi E, Hiura K, Kameda A, Yang NN, Hakeda Y, Kumegawa M (1997) Estrogen inhibits bone resorption by directly inducing apoptosis of the bone-resorbing osteoclasts. *The Journal of experimental medicine* 186:489-495
92. Hughes DE, Dai A, Tiffie JC, Li HH, Mundy GR, Boyce BF (1996) Estrogen promotes apoptosis of murine osteoclasts mediated by TGF-beta. *Nature medicine* 2:1132-1136
93. Hui SK, Fairchild GR, Kidder LS, Sharma M, Bhattacharya M, Jackson S, Le C, Petryk A, Islam MS, Yee D (2013) The influence of therapeutic radiation on the patterns of bone remodeling in ovary-intact and ovariectomized mice. *Calcif Tissue Int* 92:372-384
94. Swift JM, Smith JT, Kiang JG (2015) Hemorrhage trauma increases radiation-induced trabecular bone loss and marrow cell depletion in mice. *Radiation research* 183:578-583
95. Schreurs AS, Shirazi-Fard Y, Shahnazari M, Alwood JS, Truong TA, Tahimic CG, Limoli CL, Turner ND, Halloran B, Globus RK (2016) Dried plum diet protects from bone loss caused by ionizing radiation. *Scientific reports* 6:21343

96. Alwood JS, Shahnazari M, Chicana B, Schreurs AS, Kumar A, Bartolini A, Shirazi-Fard Y, Globus RK (2015) Ionizing Radiation Stimulates Expression of Pro-Osteoclastogenic Genes in Marrow and Skeletal Tissue. *Journal of interferon & cytokine research : the official journal of the International Society for Interferon and Cytokine Research* 35:480-487
97. Chmura SJ, Winter KA, Al-Hallaq HA, Borges VF, Jaskowiak NT, Matuszak M, Milano MT, Salama JK, Woodward WA, White JR (2019) NRG-BR002: A phase IIR/III trial of standard of care therapy with or without stereotactic body radiotherapy (SBRT) and/or surgical ablation for newly oligometastatic breast cancer (NCT02364557). *Journal of Clinical Oncology* 37:TPS1117-TPS1117
98. Palma DA, Olson R, Harrow S, Correa RJM, Schneiders F, Haasbeek CJA, Rodrigues GB, Lock M, Yaremko BP, Bauman GS, Ahmad B, Schellenberg D, Liu M, Gaede S, Laba J, Mulroy L, Senthil S, Louie AV, Swaminath A, Chalmers A, Warner A, Slotman BJ, de Gruijl TD, Allan A, Senan S (2019) Stereotactic ablative radiotherapy for the comprehensive treatment of 4-10 oligometastatic tumors (SABR-COMET-10): study protocol for a randomized phase III trial. *BMC Cancer* 19:816
99. Jee WS, Yao W (2001) Overview: animal models of osteopenia and osteoporosis. *Journal of musculoskeletal & neuronal interactions* 1:193-207
100. Campbell GM, Sophocleous A (2014) Quantitative analysis of bone and soft tissue by micro-computed tomography: applications to ex vivo and in vivo studies. *BoneKey reports* 3:564
101. Hohlbaum K, Bert B, Dietze S, Palme R, Fink H, Thöne-Reineke C (2017) Severity classification of repeated isoflurane anesthesia in C57BL/6JRj mice—Assessing the degree of distress. *PLOS ONE* 12:e0179588
102. Faienza MF, Ventura A, Marzano F, Cavallo L (2013) Postmenopausal osteoporosis: the role of immune system cells. *Clinical & developmental immunology* 2013:575936
103. Lorimore SA, Coates PJ, Scobie GE, Milne G, Wright EG (2001) Inflammatory-type responses after exposure to ionizing radiation in vivo: a mechanism for radiation-induced bystander effects? *Oncogene* 20:7085-7095
104. Hui SK, Khalil A, Zhang Y, Coghill K, Le C, Dusenbery K, Froelich J, Yee D, Downs L (2010) Longitudinal assessment of bone loss from diagnostic computed tomography scans in gynecologic cancer patients treated with chemotherapy and radiation. *American journal of obstetrics and gynecology* 203:353.e351-357

105. Okoukoni C, Lynch SK, McTyre ER, Randolph DM, Weaver AA, Blackstock AW, Lally BE, Munley MT, Willey JS (2016) A cortical thickness and radiation dose mapping approach identifies early thinning of ribs after stereotactic body radiation therapy. *Radiotherapy and oncology : journal of the European Society for Therapeutic Radiology and Oncology* 119:449-453
106. Okoukoni C, Randolph DM, McTyre ER, Kwok A, Weaver AA, Blackstock AW, Munley MT, Willey JS (2017) Early dose-dependent cortical thinning of the femoral neck in anal cancer patients treated with pelvic radiation therapy. *Bone* 94:84-89
107. Farris M, McTyre ER, Okoukoni C, Dugan G, Johnson BJ, Blackstock AW, Munley MT, Bourland JD, Cline JM, Willey JS (2018) Cortical Thinning and Structural Bone Changes in Non-Human Primates after Single-Fraction Whole-Chest Irradiation. *Radiation research* 190:63-71
108. Turner RT, Iwaniec UT, Wong CP, Lindenmaier LB, Wagner LA, Branscum AJ, Menn SA, Taylor J, Zhang Y, Wu H, Sibonga JD (2013) Acute exposure to high dose gamma-radiation results in transient activation of bone lining cells. *Bone* 57:164-173
109. Deyhle RT, Jr., Wong CP, Martin SA, McDougall MQ, Olson DA, Branscum AJ, Menn SA, Iwaniec UT, Hamby DM, Turner RT (2019) Maintenance of Near Normal Bone Mass and Architecture in Lethally Irradiated Female Mice following Adoptive Transfer with as few as 750 Purified Hematopoietic Stem Cells. *Radiation research* 191:413-427
110. Black DM, Rosen CJ (2016) Clinical Practice. Postmenopausal Osteoporosis. *The New England journal of medicine* 374:254-262
111. Hui SK, Fairchild GR, Kidder LS, Sharma M, Bhattacharya M, Jackson S, Le C, Yee D (2012) Skeletal remodeling following clinically relevant radiation-induced bone damage treated with zoledronic acid. *Calcif Tissue Int* 90:40-49
112. Keenawinna L, Oest ME, Mann KA, Spadaro J, Damron TA (2013) Zoledronic acid prevents loss of trabecular bone after focal irradiation in mice. *Radiation research* 180:89-99
113. Patntirapong S, Poolgesorn M (2018) Alteration of macrophage viability, differentiation, and function by bisphosphonates. *Oral diseases* 24:1294-1302
114. Bryant AK, Banegas MP, Martinez ME, Mell LK, Murphy JD (2017) Trends in Radiation Therapy among Cancer Survivors in the United States, 2000-2030. *Cancer*

epidemiology, biomarkers & prevention : a publication of the American Association for Cancer Research, cosponsored by the American Society of Preventive Oncology 26:963-970

115. Miller KD, Nogueira L, Mariotto AB, Rowland JH, Yabroff KR, Alfano CM, Jemal A, Kramer JL, Siegel RL (2019) Cancer treatment and survivorship statistics, 2019. *CA: a cancer journal for clinicians* 69:363-385
116. Dieckmann K, Widder J, Potter R (2002) Long-term side effects of radiotherapy in survivors of childhood cancer. *Frontiers of radiation therapy and oncology* 37:57-68
117. Martin RM, Correa PH (2010) Bone quality and osteoporosis therapy. *Arquivos brasileiros de endocrinologia e metabologia* 54:186-199
118. Grey A, Reid IR (2006) Differences between the bisphosphonates for the prevention and treatment of osteoporosis. *Ther Clin Risk Manag* 2:77-86
119. Dalle Carbonare L, Zanatta M Fau - Gasparetto A, Gasparetto A Fau - Valenti MT, Valenti MT Safety and tolerability of zoledronic acid and other bisphosphonates in osteoporosis management.
120. Clezardin P Mechanisms of action of bisphosphonates in oncology: a scientific concept evolving from antiresorptive to anticancer activities.
121. Paschalis EP, DiCarlo E, Betts F, Sherman P, Mendelsohn R, Boskey AL (1996) FTIR microspectroscopic analysis of human osteonal bone. *Calcif Tissue Int* 59:480-487
122. Heveran CM, Schurman CA, Acevedo C, Livingston EW, Howe D, Schaible EG, Hunt HB, Rauff A, Donnelly E, Carpenter RD, Levi M, Lau AG, Bateman TA, Alliston T, King KB, Ferguson VL (2019) Chronic kidney disease and aging differentially diminish bone material and microarchitecture in C57Bl/6 mice. *Bone* 127:91-103
123. Hagino H (2015) [Bisphosphonate]. *Nihon rinsho. Japanese journal of clinical medicine* 73:1683-1689
124. Unal M, Uppuganti S, Timur S, Mahadevan-Jansen A, Akkus O, Nyman JS (2019) Assessing matrix quality by Raman spectroscopy helps predict fracture toughness of human cortical bone. *Scientific reports* 9:7195

125. Chauhan S, Khan SA, Prasad A (2018) Irradiation-Induced Compositional Effects on Human Bone After Extracorporeal Therapy for Bone Sarcoma. *Calcif Tissue Int* 103:175-188
126. Marx RE, Cillo JE, Ulloa JJ (2007) Oral Bisphosphonate-Induced Osteonecrosis: Risk Factors, Prediction of Risk Using Serum CTX Testing, Prevention, and Treatment. *Journal of Oral and Maxillofacial Surgery* 65:2397-2410
127. Saita Y, Ishijima M, Kaneko K (2015) Atypical femoral fractures and bisphosphonate use: current evidence and clinical implications. *Therapeutic advances in chronic disease* 6:185-193
128. Ettinger B, Burr DB, Ritchie RO (2013) Proposed pathogenesis for atypical femoral fractures: lessons from materials research. *Bone* 55:495-500
129. Amanata N, He LH, Swain MV, Little DG (2008) The effect of zoledronic acid on the intrinsic material properties of healing bone: an indentation study. *Medical engineering & physics* 30:843-847
130. Casanova M, Herelle J, Thomas M, Softley R, Schindeler A, Little D, Schneider P, Muller R (2016) Effect of combined treatment with zoledronic acid and parathyroid hormone on mouse bone callus structure and composition. *Bone* 92:70-78
131. Burket JC, Brooks DJ, MacLeay JM, Baker SP, Boskey AL, van der Meulen MC (2013) Variations in nanomechanical properties and tissue composition within trabeculae from an ovine model of osteoporosis and treatment. *Bone* 52:326-336
132. Olejnik C, Falgayrac G, During A, Cortet B, Penel G (2016) Doses effects of zoledronic acid on mineral apatite and collagen quality of newly-formed bone in the rat's calvaria defect. *Bone* 89:32-39
133. Brennan O, Kennedy OD, Lee TC, Rackard SM, O'Brien FJ, McNamara LM (2011) The effects of estrogen deficiency and bisphosphonate treatment on tissue mineralisation and stiffness in an ovine model of osteoporosis. *J Biomech* 44:386-390
134. Oest ME, Policastro CG, Mann KA, Zimmerman ND, Damron TA (2018) Longitudinal Effects of Single Hindlimb Radiation Therapy on Bone Strength and Morphology at Local and Contralateral Sites. *Journal of bone and mineral research : the official journal of the American Society for Bone and Mineral Research* 33:99-112

135. Baxter NN, Habermann Eb Fau - Tepper JE, Tepper Je Fau - Durham SB, Durham Sb Fau - Virnig BA, Virnig BA Risk of pelvic fractures in older women following pelvic irradiation.
136. Glatt V, Canalis E, Stadmeier L, Bouxsein ML (2007) Age-related changes in trabecular architecture differ in female and male C57BL/6J mice. *Journal of bone and mineral research : the official journal of the American Society for Bone and Mineral Research* 22:1197-1207
137. Dalle Carbonare L, Zanatta M, Gasparetto A, Valenti MT (2010) Safety and tolerability of zoledronic acid and other bisphosphonates in osteoporosis management. *Drug Healthc Patient Saf* 2:121-137
138. Vermeer J, Renders G, van Duin MA, Jansen I, Bakker LF, Kroon SA, de Vries TJ, Everts V (2017) Bone-site-specific responses to zoledronic acid. *Oral diseases* 23:126-133
139. Sullivan LK, Livingston EW, Lau AG, Rao-Dayton S, Bateman TA (2019) A Mouse Model for Skeletal Structure and Function Changes Caused by Radiation Therapy and Estrogen Deficiency. *Calcif Tissue Int*
140. Soucie JM (2019) Global Hemophilia Care: Data for Action. *Annals of internal medicine*
141. Bolton-Maggs PH, Pasi KJ (2003) Haemophilias A and B. *Lancet (London, England)* 361:1801-1809
142. Nair PS, Shetty S, Ghosh K (2012) A homozygous female hemophilia A. *Indian journal of human genetics* 18:134-136
143. Franchini M, Mannucci PM (2013) Hemophilia A in the third millennium. *Blood reviews* 27:179-184
144. Sokoloff L Biochemical and physiological aspects of degenerative joint diseases with special reference to hemophilic arthropathy. *Annals of the New York Academy of Sciences* 240:285-290
145. Hakobyan N, Enockson C, Cole AA, Sumner DR, Valentino LA (2008) Experimental haemophilic arthropathy in a mouse model of a massive haemarthrosis: gross,

radiological and histological changes. *Haemophilia* : the official journal of the World Federation of Hemophilia 14:804-809

146. Sun J, Hakobyan N, Valentino LA, Feldman BL, Samulski RJ, Monahan PE (2008) Intraarticular factor IX protein or gene replacement protects against development of hemophilic synovitis in the absence of circulating factor IX. *Blood* 112:4532-4541
147. Narkbunnam N, Sun J, Hu G, Lin FC, Bateman TA, Mihara M, Monahan PE (2013) IL-6 receptor antagonist as adjunctive therapy with clotting factor replacement to protect against bleeding-induced arthropathy in hemophilia. *Journal of thrombosis and haemostasis* : JTH 11:881-893
148. Sen D, Chapla A, Walter N, Daniel V, Srivastava A, Jayandharan GR (2013) Nuclear factor (NF)-kappaB and its associated pathways are major molecular regulators of blood-induced joint damage in a murine model of hemophilia. *Journal of thrombosis and haemostasis* : JTH 11:293-306
149. Ovlisen K, Kristensen AT, Valentino LA, Hakobyan N, Ingerslev J, Tranholm M (2008) Hemostatic effect of recombinant factor VIIa, NN1731 and recombinant factor VIII on needle-induced joint bleeding in hemophilia A mice. *Journal of thrombosis and haemostasis* : JTH 6:969-975
150. Ovlisen K, Kristensen AT, Jensen AL, Tranholm M (2009) IL-1 beta, IL-6, KC and MCP-1 are elevated in synovial fluid from haemophilic mice with experimentally induced haemarthrosis. *Haemophilia* : the official journal of the World Federation of Hemophilia 15:802-810
151. Nieuwenhuizen L, Roosendaal G, Coeleveld K, Lubberts E, Biesma DH, Lafeber FP, Schutgens RE (2013) Haemarthrosis stimulates the synovial fibrinolytic system in haemophilic mice. *Thrombosis and haemostasis* 110:173-183
152. van Meegeren ME, Roosendaal G, Coeleveld K, Nieuwenhuizen L, Mastbergen SC, Lafeber FP (2013) A single intra-articular injection with IL-4 plus IL-10 ameliorates blood-induced cartilage degeneration in haemophilic mice. *British journal of haematology* 160:515-520
153. Taves S, Sun J, Livingston EW, Chen X, Amiaud J, Brion R, Hannah WB, Bateman TA, Heymann D, Monahan PE (2019) Hemophilia A and B mice, but not VWF(-/-)mice, display bone defects in congenital development and remodeling after injury. *Scientific reports* 9:14428

154. Baud'huin M, Duplomb L, Teletchea S, Charrier C, Maillason M, Fouassier M, Heymann D (2009) Factor VIII-von Willebrand factor complex inhibits osteoclastogenesis and controls cell survival. *The Journal of biological chemistry* 284:31704-31713
155. Liel MS, Greenberg DL, Recht M, Vanek C, Klein RF, Taylor JA (2012) Decreased bone density and bone strength in a mouse model of severe factor VIII deficiency. *British journal of haematology* 158:140-143
156. Sun Y, Mauerhan DR, Honeycutt PR, Kneisl JS, Norton HJ, Zinchenko N, Hanley EN, Jr., Gruber HE (2010) Calcium deposition in osteoarthritic meniscus and meniscal cell culture. *Arthritis research & therapy* 12:R56
157. Bi L, Lawler AM, Antonarakis SE, High KA, Gearhart JD, Kazazian HH, Jr. (1995) Targeted disruption of the mouse factor VIII gene produces a model of haemophilia A. *Nature genetics* 10:119-121
158. Batty P, Lillicrap D (2019) Advances and challenges for hemophilia gene therapy. *Hum Mol Genet* 28:R95-r101
159. Desai MK, Brinton RD (2019) Autoimmune Disease in Women: Endocrine Transition and Risk Across the Lifespan. *Front Endocrinol (Lausanne)* 10:265-265
160. Taneja V (2018) Sex Hormones Determine Immune Response. *Front Immunol* 9:1931-1931
161. Tai K, Dao M, Suresh S, Palazoglu A, Ortiz C (2007) Nanoscale heterogeneity promotes energy dissipation in bone. *Nat Mater* 6:454-462
162. Lloyd AA, Wang ZX, Donnelly E (2015) Multiscale contribution of bone tissue material property heterogeneity to trabecular bone mechanical behavior. *J Biomech Eng* 137:0108011-0108018
163. Melchiorre D, Linari S, Innocenti M, Biscoglio I, Toigo M, Cerinic MM, Morfini M (2011) Ultrasound detects joint damage and bleeding in haemophilic arthropathy: a proposal of a score. *Haemophilia : the official journal of the World Federation of Hemophilia* 17:112-117

164. Rodriguez-Florez N, Oyen ML, Shefelbine SJ (2013) Insight into differences in nanoindentation properties of bone. *Journal of the Mechanical Behavior of Biomedical Materials* 18:90-99
165. Donnelly E, Baker SP, Boskey AL, van der Meulen MCH (2006) Effects of surface roughness and maximum load on the mechanical properties of cancellous bone measured by nanoindentation. *J Biomed Mater Res A* 77:426-435
166. Jerome C, Hoch B (2012) 5 - Skeletal System. In: Treuting PM, Dintzis SM (eds) *Comparative Anatomy and Histology*. Academic Press, San Diego, p 53-70
167. Ayorinde RO, Okolo CA (2009) Concurrent femoral neck fractures following pelvic irradiation: a case report. *J Med Case Rep* 3:9332-9332
168. Peterson JR, Okagbare PI, De La Rosa S, Cilwa KE, Perosky JE, Eboda ON, Donneys A, Su GL, Buchman SR, Cederna PS, Wang SC, Kozloff KM, Morris MD, Levi B (2013) Early detection of burn induced heterotopic ossification using transcutaneous Raman spectroscopy. *Bone* 54:28-34